

**SYNTHESIS AND THERMOELECTRIC STUDIES OF
DUAL ION (Ni-In, Ni-Pr, Ni-Cu, and Al-Cu) DOPED
ZnO CERAMICS**

*Thesis submitted to the
University of Calicut for the partial fulfillment of the requirements
for the award of the degree of*

DOCTOR OF PHILOSOPHY IN PHYSICS

Under the Faculty of Science

By

SOUMYA C

Under the guidance of

Prof. (Dr.) P. P. PRADYUMNAN
Senior Professor



**DEPARTMENT OF PHYSICS
UNIVERSITY OF CALICUT
KERALA, INDIA 673 635
2023**



Department of Physics UNIVERSITY OF CALICUT

Dr. P.P. Pradyumnan
Senior Professor

Calicut University P.O
Kerala, India 673 635
Tel: +919895961751
Fax: 0494-2400269
E-mail: drpradyumnan@gmail.com

Certificate

Certified that the work presented in this thesis entitled “**Synthesis and thermoelectric studies of dual ion (Ni-In, Ni-Pr, Ni-Cu, and Al-Cu) doped ZnO ceramics**” is submitted to the University of Calicut in partial fulfillment of the requirements for the award of degree of Doctor of Philosophy in Physics is a record of original research work done by **Ms. SOUMYA C** during the period 2014 - 2023 under my guidance in the Department of Physics, University of Calicut. The thesis has not formed the basis for the award of any Degree/Diploma and has undergone plagiarism check using OURIGINAL software at CHMK Library, University of Calicut and the similarity index is found within the permissible limit.

Calicut University
June 2023


Prof. (Dr.) P. P. Pradyumnan

Prof.(Dr.) P.P. PRADYUMNAN
Senior Professor
Department of Physics
University of Calicut
Kerala - 673 635, India



Department of Physics UNIVERSITY OF CALICUT


Dr. P.P. Pradyumnan
Senior Professor

Calicut University P.O
Kerala, India 673 635
Tel: +919895961751
Fax: 0494-2400269
E-mail: drpradyumnan@gmail.com

Certificate

The adjudicators of the thesis entitled “Synthesis and thermoelectric studies of dual ion (Ni-In, Ni-Pr, Ni-Cu, and Al-Cu) doped ZnO ceramics” submitted by Soumya C, have not recommended or suggested any corrections/modifications in any part of the submitted thesis, and the content of the thesis in both hard copy and soft copy are one and same.

Calicut University
15 February 2024


Prof. (Dr.) P. P. Pradyumnan

Prof.(Dr.) P.P. PRADYUMNAN
Senior Professor
Department of Physics
University of Calicut
Kerala - 673 635, India



Department of Physics UNIVERSITY OF CALICUT

Dr. P.P. Pradyumnan
Senior Professor


Calicut University P.O
Kerala, India 673 635
Tel: +919895961751
Fax: 0494-2400269
E-mail: drpradyumnan@gmail.com

Certificate

Certified that the following articles are authored/co-authored by Soumya C, under my supervision during the research period in the Department of Physics, University of Calicut.

1. C. Soumya, P. P. Pradyumnan, Waste heat energy harvesting by using praseodymium, nickel codoped zinc oxide thermoelectric materials. J Mater Sci 58, 16771–16784 (2023). <https://doi.org/10.1007/s10853-023-09034-w>
2. C. Soumya, P.P. Pradyumnan, Enhancement of thermoelectric properties of transition metals, nickel and copper dually doped ZnO, Mater. Today Commun. 35 (2023). <https://doi.org/10.1016/j.mtcomm.2023.106197>
3. C. Soumya, P.P. Pradyumnan, Enhancement of thermoelectric power factor of zinc oxide by nickel and indium dual doping, Int. J. Energy Res. 46 (2022) 19574–19584. <https://doi.org/10.1002/er.8529>
4. C. Soumya, P.P. Pradyumnan, Synthesis and characterizations of nickel doped zinc oxide, AIP Conf. Proc. 2287 (2020) 5–10. <https://doi.org/10.1063/5.0029876>.

Calicut University
June 2023


Prof. (Dr.) P. P. Pradyumnan
Prof.(Dr.) P.P. PRADYUMNAN
Senior Professor
Department of Physics
University of Calicut
Kerala - 673 635, India

Declaration

I, SOUMYA C, hereby declared that this thesis work “**Synthesis and thermoelectric studies of dual ion (Ni-In, Ni-Pr, Ni-Cu, and Al-Cu) doped ZnO ceramics**” submitted to the Department of Physics, University of Calicut is a record of the original work done by me under the guidance of Prof. (Dr.) P. P. Pradyumnan, Senior Professor, Department of Physics, University of Calicut and this work has not been included in any other thesis submitted previously for the award of any degree. It is also certified that the thesis has undergone plagiarism check using OUR ORIGINAL software at CHMK Library, University of Calicut and the similarity index is found within the permissible limit.



Calicut University

Date :

SOUMYA C

Acknowledgment

I am deeply grateful to my research supervisor Prof. (Dr.) P. P. Pradyumnan, Senior Professor, Department of Physics, University of Calicut for all the guidance, and instructions he provided me throughout the research work. Without his boundless support and guidance, the completion of this Ph.D. would not have been possible. He is always available as a mentor to me, support and encourages me in all the stages of my research work. His deep insight and experience directed me to the right path of research. He continuously evaluated my research work by giving me enough freedom and appreciated my efforts. I deeply acknowledge his patience and valuable suggestions in correcting my thesis.

I am truly thankful to Dr. C.D. Ravikumar, Head of the Department of Physics, and all the other former HODs including Dr. Antony Joseph, Dr. A.M. Vinodkumar and Dr. M.M. Musthafa for providing the facilities in the department to carry out my research work. I am glad to extend and express my sincere gratitude to all the faculty members including Dr. Libu K. Alexander, Dr. Muhammed Shahin Thayyil, Dr. Zuhail K. P. and Dr. Drisya. K for their critical advice and support during the period. Thanks to all non-teaching staff for their help and cooperation throughout the course of the research work.

I am deeply thankful to my dear friends Jumanath, Sabeer, Anju, and Parvathy for the unconditional support, love, and care that they have shown me throughout my research work. They are always with me to provide mental support and encourage and motivate me to complete this research work. Many thanks to my senior co-researchers Dr. Binitha, Dr. Ramachandran T, Dr. Jaya T P, Dr. Divya N K, Dr. Shyni P and my lab mates Nabeela, Hashir, Vineetha, Hisna, Midhun Shah, and Jamshina for their support during the research work. Thanks to all other research scholars in the Department for providing valuable suggestions for my research.

I would like to extend my gratitude to my colleagues Asha, Jayasree, Sherina, Lisha, and Vinni for their boundless support and care during the entire course of my

research. My sincere thanks to my friends Sajan and Shahina for their technical assistance and support.

I am eternally grateful to my parents, who have been my genuine pillars of strength, and to my sisters Remya and Suremya, and my cousin brother Ramesh who have supported me through all of life's ups and downs with unending love, care, and affection.

I gratefully thank my husband, Krishnakumar, as my best friend he was always there to listen and support me during my research work. I express my heartfelt gratitude to my little son Darshan, who make me laugh and gave me unlimited pleasure and happiness when I was writing my thesis.

SOUMYA C

*Dedicated to
My parents and Teachers*

Contents

	<i>Page No.</i>
Preface	
Chapter 1	1-34
Fundamentals of thermoelectricity and waste heat energy management	
1.1 Introduction	1
1.2. Thermoelectric phenomena	3
1.2.1 Seebeck effect	3
1.2.2 Peltier Effect	5
1.2.3. Thomson Effect	6
1.3 Thermoelectric power generation and refrigeration	7
1.4 Thermoelectric parameters and efficiency	8
1.4.1. Electrical transport properties	11
a) Doping or alloying	11
b) Low dimensional systems	12
c) Resonant levels	12
d) Energy filtering	13
e) Band tailoring	14
1.4.2. Thermal transport	15
1.5 Theory of thermoelectric phenomena in metals and semiconductors	17
1.6 Materials for waste heat management	22
1.6.1 Chalcogenides	23
1.6.2 Skutterudites	24
1.6.3 Half-Heusler alloys	25
1.6.4 Clathrates	25
1.6.5 Oxide materials	26
1.7 Methods to enhance thermoelectric properties of zinc oxide	28
1.7.1 Doping	28
1.7.2 Nanostructuring	29
1.7.3 Quantum confinement	29
1.8 Motivation and objectives	29
References	31

Chapter 2	35-53
Material preparation and characterization techniques	
2.1 Introduction	35
2.2 Solid-state reaction technique	35
2.2.1 Mixing & grinding	35
2.2.2 Calcination	36
2.2.3 Pelletization	36
2.2.4. Sintering	36
2.3 Characterization techniques	39
2.3.1 Powder X-ray diffraction	39
2.3.2 Field emission scanning electron microscopy (FESEM)	42
2.3.3 Energy dispersive X-ray spectroscopy (EDAX/EDS)	44
2.3.4 UV-Vis spectroscopic analysis	46
2.3.5 Hall measurement	47
2.3.6 Thermoelectric measurements	48
2.3.7 Thermal conductivity measurements	51
References	53
Chapter 3	55-74
Preparation, characterization, and thermoelectric performance of Ni-In dual doped zinc oxide	
3.1 Introduction	55
3.2 Experimental method	56
3.3 Results and discussions	56
3.3.1 Structural characterisations	56
3.3.2 FESEM and EDAX analysis	60
3.3.3 UV-Vis spectroscopic analysis	61
3.3.4 Thermoelectric property studies	63
3.3.4.1 Electrical conductivity	63
3.3.4.2 Seebeck coefficient	65
3.3.4.3 Power factor	68
3.3.4.4 Thermal conductivity	69
3.3.4.5 Figure of merit	71
3.4 Conclusion	71
References	73

Chapter 4	75-92
Nickel and praseodymium, codoped zinc oxide materials for thermoelectric applications	
4.1 Introduction	75
4.2 Experimental method	76
4.3 Results and discussions	76
4.3.1 Structural characterisations	76
4.3.2 FESEM and EDAX analysis	79
4.3.3 UV-Vis spectroscopic analysis	81
4.3.4 Thermoelectric property studies	83
4.3.4.1 Electrical conductivity	83
4.3.4.2 Seebeck coefficient	84
4.3.4.3 Power factor	86
4.3.4.4 Thermal conductivity	87
4.3.4.5 Figure of merit	89
4.4 Conclusion	90
References	91
Chapter 5	93-110
Effects of Ni-Cu dual doping on the thermoelectric properties of ZnO	
5.1 Introduction	93
5.2 Experimental methods	94
5.3 Results and discussions	94
5.3.1 Structural characterisation	94
5.3.2 FESEM and EDAX analysis	97
5.3.3 UV-Vis spectroscopic analysis	98
5.3.4 Thermoelectric studies	99
5.3.4.1 Electrical conductivity	99
5.3.4.2 Seebeck coefficient	101
5.3.4.3 Power factor	103
5.3.4.4 Thermal conductivity	104
5.3.4.5 Figure of merit	107
5.4 Conclusion	107
References	108
Chapter 6	111-127
Thermoelectric features of Al-Cu dual doped ZnO	
6.1 Introduction	111
6.2 Experimental methods	112

6.3 Results and discussions	112
6.3.1 X-ray diffraction analysis	112
6.3.2 FESEM and EDAX analysis	115
6.3.3 UV-Vis spectroscopic analysis	117
6.3.4 Thermoelectric property studies	118
6.3.4.1 Electrical conductivity	118
6.3.4.2 Seebeck coefficient	119
6.3.4.3 Power factor	122
6.3.4.4 Thermal conductivity	123
6.3.4.5 Figure of merit	124
6.4 Conclusion	125
References	126
Chapter 7	129-135
General conclusions	
7.1 Introduction	129
7.2 Summary of the research work	129
7.2.1 Ni and In dual doped ZnO	130
7.2.2 Ni and Pr dual doped ZnO	131
7.2.3 Ni and Cu dual doped ZnO	132
7.2.4 Al and Cu dual doped ZnO	133
Chapter 8	137-138
Scope for future research	
8.1 Introduction	137
8.2 Recommendations for future research	137

List of tables

<i>Table No.</i>	<i>Title</i>	<i>Page No.</i>
3.1	Average crystallite size and the induced strain of the materials	58
3.2	Fermi level shift from the conduction band edge of doped and undoped samples	67
3.3	Comparison of PF and ZT with different dopants	71
4.1	Crystallite size and strain produced in the samples	77
4.2	Elemental composition of the samples	80
4.3	Fermi level shift observed in the samples	86
5.1	Lattice constants of ZnO and doped ZnO materials	95
5.2	Crystallite size and microstrain calculated from W-H plot	95
5.3	Fermi-level shift and DOS effective mass of the prepared materials	102
6.1	Crystallite size and induced microstrain	114
6.2	Fermi level shift and DOS effective mass of the samples	121
7.1	Comparison of TE properties of best performed dual doped material with ZnO	135

List of Figures

<i>Figure No.</i>	<i>Title</i>	<i>Page No.</i>
1.1	Voltage generation in a circuit of dissimilar metals through the Seebeck effect	4
1.2	Peltier effect	5
1.3	Thomson effect	7
1.4	Power generation and refrigeration of thermoelectric materials	8
1.5	Variation of Seebeck coefficient (S), electrical conductivity (σ), and thermal conductivity (κ) with carrier concentration (n)	10
1.6	The energy band diagram of (a) metals (b) insulator (c) semiconductor (d) semimetal	18
1.7	State-of-the-art thermoelectric materials	23
2.1	Therelek electrically heated high temperature furnace	37
2.2	Procedure for solid-state reaction of dual doped ZnO materials	38
2.3	Illustration of X-ray diffraction	40
2.4	Rigaku Miniflex X-ray diffractometer	42
2.5	Illustration of SEM	45
2.6	Carl Zeiss Sigma model FESEM with EDAX facility	45
2.7	Schematic representation of UV-Vis spectrophotometer	47
2.8	Illustration of Hall effect	48
2.9	ULVAC ZEM-3 (M8) measurement system	50
2.10	Schematic representation of ULVAC-ZEM-3	50
2.11	Schematic representation of divider bar method	51
2.12	Thermal conductivity measurement set up	52
2.13	Temperature versus distance from one end of the block	52
3.1	Powder XRD pattern of undoped and doped samples	58
3.2	Powder XRD Peak shift of (101) plane	59
3.3	FESEM and EDAX images of (a) ZnO (b) $N_1I_{0.25}$ (c) $N_1I_{0.5}$ (d) N_1I_1 (e) N_1I_2	60
3.4	EDS mapping of N_1I_1 (a) Zinc (b) Oxygen (c) Nickel (d) Indium	61
3.5	Tauc's plot of undoped and doped samples	63
3.6	Electrical conductivity of the samples with temperature	65
3.7	Variation of Seebeck coefficient of the samples with temperature	67
3.8	Variation of power factor of the samples with temperature	68
3.9	Variation of thermal conductivity of the samples with temperature	70

3.10	Variation of figure of merit of the samples with temperature	70
4.1	XRD patterns of prepared samples	78
4.2	Peak Shift of (101) plane	78
4.3	FESEM images of (a) ZnO (b) $N_1P_{0.3}$ (c) $N_1P_{0.5}$ (d) $N_1P_{0.7}$	79
4.4	EDAX images of (a) ZnO (b) $N_1P_{0.3}$ (c) $N_1P_{0.5}$ (d) $N_1P_{0.7}$	80
4.5	EDS mapping of $N_1P_{0.5}$ (a) Zinc (b) Oxygen (c) Nickel (d) Praseodymium	81
4.6	Tauc's plot of undoped and doped samples	82
4.7	Electrical conductivity of undoped and doped samples	84
4.8	Seebeck coefficient of undoped and doped samples	86
4.9	Power factor of undoped and doped samples	87
4.10	Thermal conductivity of undoped and doped samples	89
4.11	Figure of merit of undoped and doped samples	90
5.1	XRD pattern of the undoped and doped samples	96
5.2	Peak shift of (101) plane	96
5.3	FESEM images of (a) ZnO (b) $N1C1$ (c) $N1C2$ (d) $N2C1$	97
5.4	EDAX spectrum of (a) ZnO (b) $N1C1$ (c) $N1C2$ (d) $N2C1$	98
5.5	Optical band gap energy of doped and undoped samples	99
5.6	Variation of electrical conductivity of samples with temperature	100
5.7	Variation of Seebeck coefficient of the samples with temperature	103
5.8	Variation of power factor of the samples with temperature	104
5.9	Variation of lattice thermal conductivity of the samples with temperature	105
5.10	Variation of total thermal conductivity of the samples with temperature	106
5.11	Variation of figure of merit of the samples with temperature	106
6.1	XRD pattern of undoped and doped materials	113
6.2	XRD peak shift of (101) plane	114
6.3	FESEM images of (a) ZnO (b) $A1C1$ (c) $A2C1$ (d) $A1C3$	115
6.4	EDAX spectrum of materials (a) ZnO (b) $A1C1$ (c) $A2C1$ (d) $A1C3$	116
6.5	Band gap energy of (a) ZnO (b) $A1C1$ (c) $A2C1$ (d) $A1C3$	117
6.6	Temperature dependent electrical conductivity of the materials	118
6.7	Temperature dependent Seebeck coefficient of the materials	120
6.8	Temperature dependent power factor of the materials	122
6.9	Temperature dependent thermal conductivity of the materials	123
6.10	Temperature dependent figure of merit of the materials	124

List of Abbreviations

R & AC	- Refrigeration and Air conditioning
TEG	- Thermoelectric generator
TEC	- Thermoelectric cooler
COP	- Coefficient of Performance
PGEC	- Phonon Glass Electron Crystal
FESEM	- Field Emission Scanning Electron Microscopy
SEM	- Scanning Electron Microscopy
SE	- Secondary Electron
BSE	- Back Scattered Electron
EDAX	- Energy Dispersive X-ray Spectroscopy
FWHM	- Full width at Half Maximum
PF	- Power factor

Symbols used

ZT	-	Figure of merit
S	-	Seebeck coefficient
T	-	Temperature
T_H	-	Hot junction temperature
T_C	-	Cold junction temperature
η	-	Thomson coefficient
π	-	Peltier coefficient
σ	-	Electrical conductivity
κ	-	Thermal conductivity
κ_e	-	Electronic thermal conductivity
κ_l	-	Lattice thermal conductivity
μ	-	Carrier mobility
η	-	Efficiency
E_F	-	Fermi energy
n	-	Carrier density
m^*	-	Effective mass
L	-	Lorentz constant
λ	-	Wavelength
E_g	-	Band gap energy

Research Publications

1. C. Soumya, P. P. Pradyumnan, Waste heat energy harvesting by using praseodymium, nickel codoped zinc oxide thermoelectric materials. *J Mater Sci* 58, 16771–16784 (2023). <https://doi.org/10.1007/s10853-023-09034-w>
2. C. Soumya, P.P. Pradyumnan, Enhancement of thermoelectric properties of transition metals, nickel and copper dually doped ZnO, *Mater. Today Commun.* 35 (2023). <https://doi.org/10.1016/j.mtcomm.2023.106197>
3. C. Soumya, P.P. Pradyumnan, Enhancement of thermoelectric power factor of zinc oxide by nickel and indium dual doping, *Int. J. Energy Res.* 46 (2022) 19574–19584. <https://doi.org/10.1002/er.8529>
4. C. Soumya, P.P. Pradyumnan, Synthesis and characterizations of nickel doped zinc oxide, *AIP Conf. Proc.* 2287 (2020) 5–10. <https://doi.org/10.1063/5.0029876>.

Papers communicated

1. C Soumya, P P Pradyumnan, Enhancement of Seebeck coefficient of Al-Cu dual doped ZnO ceramics, *Advanced Materials Technologies*.

International/ National Conferences attended and presented

1. 'World conference in thermoelectrics and materials (WCT-2023)' held at Jaipur National University, March 13-18, 2023 (Oral presentation)
2. 'International Conference on Energy and Environment 2019' held at TKM College of Arts & Science, Kollam, December 12-14, 2019 (Poster presentation)
3. International seminar on 'Recent Trends in Physics' Held at Govt College, Kodenchery, January, 15 – 16, 2015 (Oral presentation)
4. International Webinar on Frontiers in Experimental Physics - IWFEP-2020 organized by Farook College, Kozhikode, August 5-6, 2020
5. Three day International webinar series on 'Recent Trends in Nanomaterials' organized by CMS College, Kottayam, August 25-27, 2020
6. International Intradisciplinary Conference on the Frontiers of Crystallography IICFC-2014 held at Field Marshal K. M. Cariappa College, Kodagu, Karnataka, December 29-30,2014

Preface

It is essential to find new renewable, non-polluting energy sources due to the depletion of non-renewable energy sources like fossil fuels and the impact on the environment that results from their regular consumption. Thermoelectricity is one of the potential sustainable energy sources that may be used to address the current energy scarcity. In addition, thermoelectric devices reduce the rise in global atmospheric temperature and can ensure zero carbon emission to the environment. Thermoelectric devices with high efficiency can be used for power generation refrigeration applications in small and large-scale systems. It is challenging to find eco-friendly thermoelectric materials with high efficiency since many of the thermoelectric materials with high efficiency cause environmental issues. Oxide thermoelectric materials possess high efficiency at high temperatures and cause no environmental hazards. Among oxides, ZnO is a potential multifunctional metal oxide, and the field of waste heat recovery extensively exploits its thermoelectric conversion property. The thermoelectric efficiency of ZnO is tuned by doping, nanostructuring, band structure modification etc.

The thesis entitled ‘Synthesis and Thermoelectric Studies of Dual Ion (Ni-In, Ni- Pr, Ni-Cu, and Al-Cu) Doped ZnO Ceramics’ investigates the effect of dual doping on the thermoelectric performance of zinc oxide materials. Various dopants are chosen from transition metals, rare earth elements and trivalent ions to enhance the thermoelectric properties of ZnO by defect inducing technique. This thesis comprises eight chapters and the contents of the chapters are as follows.

Chapter 1 deals with the fundamental aspects of thermoelectricity and thermoelectric power generation such as the theory and techniques, various strategies to enhance the figure of merit, and a brief description of materials used for thermoelectric-conversion with detailed discussion on ZnO based systems. This chapter also describes the methods to improve the thermoelectric efficiency of ZnO and the main objectives and relevance of this research work.

Chapter 2 summarizes the solid-state reaction method, the experimental technique used for the synthesis of the dual doped ZnO materials, and the characterization techniques performed with the prepared materials. A brief discussion of the techniques to analyze the structural, morphological, and optical properties of the samples is included. The theory and procedures to study the thermoelectric property of the synthesized materials using ULVAC-ZEM-3 are briefly outlined.

Chapter 3 reports the enhancement of the thermoelectric power factor and figure of merit due to the dual doping of nickel and indium into the ZnO lattice. It includes the preparation of samples with composition $Zn_{1-x-y}Ni_xIn_yO$ and the characterizations such as XRD analysis, FESEM-EDAX analysis, UV-Vis spectroscopic studies, and thermoelectric studies of the samples. XRD and surface morphological analysis confirmed the inclusion of dual dopants in the host lattice and the optical property analysis shows the narrowing of band gap energy. Indium and nickel doping increase the carrier density leading to the increment in the electrical conductivity of ZnO. Higher electrical conductivity and better values of the Seebeck coefficient improve the power factor of doped samples. Enhancement in power factor and reduction in thermal conductivity improves the thermoelectric efficiency upon dual doping.

Chapter 4 describes how the incorporation of heavier rare-earth element praseodymium along with nickel leads to improved thermoelectric performance in ZnO. The energy filtering effect increases both the electrical conductivity and the Seebeck coefficient leading to an enhancement in the power factor. Significant reduction in thermal transport is observed due to the increased defects formed in the lattice on dual doping with nickel and ion with a large ionic radius than the host atom.

Chapter 5 discusses the introduction of transition metals nickel and copper into the ZnO structure to enhance the thermoelectric conversion efficiency of ZnO. The inclusion of ions with similar ionic radii will not alter the structure of the parent lattice and exhibit high solubility in the host material. Both the electrical conductivity and Seebeck coefficient increase as a result of the energy filtering

mechanism. The thermal conductivity measurements picture the fact that the main contribution to thermal transport comes from the lattice vibrations and not from the electronic part. Therefore, improvement in the thermoelectric figure of merit of nickel and copper doped ZnO is achieved through the enhancement in power factor and a significant reduction in thermal conductivity.

Chapter 6 discusses the thermoelectric features of aluminium and copper dual doped ZnO materials. The inclusion of dual dopants was confirmed by the structural deformations and narrowing of optical band gap energy. The remarkable result of aluminium and copper dual doping is the large enhancement of thermopower on account of the energy filtering effect. The defects created in the lattice act as phonon scattering centres, which cause a reduction in lattice thermal conductivity and hence the total thermal conductivity.

Chapter 7 consists of the general conclusions derived based on the dual ion substitution such as Ni-In, Ni-Pr, Ni-Cu, and Al-Cu. The objectives of the research investigations are achieved and it is proven experimentally. This chapter put forward that dual doping is an effective method to enhance thermoelectric efficiency since it donates more charge carriers to the parent atom and causes more lattice imperfections to scatter the phonons, thereby improving the thermoelectric performance of the material under investigation.

Chapter 8 suggests the future scope of the research in which insight into the further investigation of the dual doping approach and new materials for waste heat recovery were suggested. Novel material synthesis methods and characterisation techniques were recommended.

Chapter 1

Fundamentals of thermoelectricity and waste heat energy management

This chapter discusses the fundamentals of thermoelectricity and the conversion of waste heat into electrical energy by thermoelectric conversion techniques. It also outlines the state of the art of the current thermoelectric materials and the various strategies to tailor the thermoelectric transport properties. The motivation and the objectives of the research investigation are also discussed.

1.1 Introduction

The world's economy strongly relies on how much energy security it has achieved and whether it is capable of independent energy production. The progression of a country is thus measured in terms of its energy consumption and energy independence. But as human society advances, the most threatening and action-needed problem is the degradation of energy resources and the failure to find sustainable energy sources. For a long time, fossil fuels are the primary source of energy that has given great impetus to human progress and brought substantial changes in all spheres of society. But fossil fuels are polluting, emit greenhouse gases, and will run out within a few decades¹. Finding alternative sustainable energy sources has become crucial for lowering carbon footprints and accelerating human progress as fossil fuels are non-renewable sources and the primary source of greenhouse emissions.

The search for sustainable sources of energy leads to renewable energy sources such as solar energy, thermoelectric energy, wind energy, hydropower, etc. But most of the renewable energy sources are available only in certain regions so, we cannot completely depend on those energy sources. Among these, thermoelectricity is the most reliable energy source, as electricity can be produced even from a small temperature difference. There is an inextricable relationship between heat and electricity, both energy forms are mutually transferable, one can generate, electricity from the heat and vice versa.

Waste heat utilization is one of the best means to reduce the usage of fossil fuels and the most suitable solution to the current energy crisis. Most energy-producing systems such as automobile industries, electrical and nuclear power plants, etc. expel an enormous amount of heat energy into the atmosphere. This heat energy dissipated into the atmosphere without any use but it causes a gradual increase in the global atmospheric temperature. Heat loss from various processes is inevitable, but if there is a technique to harvest this waste heat and convert it into useful energy forms, then that technology can meet most of the world's energy requirements and will accelerate the pace of human progress. That's why the scientific community has

focussed most of its research on thermoelectric materials since thermoelectric devices use this waste heat as its input and thus, it acts as one of the solutions to environmental pollution and global warming.

Thermoelectric technology is economically viable as heat energy is readily available everywhere. Generally, thermoelectric converting systems are having solid-state devices with no moving parts, so less maintenance is required. Thermoelectric generators (TEG) are similar to that a heat engine with electrons as working fluid and they can generate electricity from very low temperature differences, therefore find applications in small-scale and remote applications.

The upsurge of thermoelectricity has led to the advancement of fields that require a continuous supply of fuel for operation but cannot provide it directly, particularly in areas such as space missions. Radioactive thermoelectric power generators are used to power space missions, by converting the heat energy produced by the radioactive decay of the radioisotope into electricity ². It is feasible to generate the energy required to operate artificial internal organs from human body temperature ³. The transportation sector contributes more to the emission of greenhouse gases and this issue can be minimized with the introduction of hybrid electric vehicles. TEGs can use as waste heat recovery systems in hybrid electric vehicles which convert the heat loss directly to electrical power ⁴. Small thermoelectric systems attached to computer systems and other electronic devices will extend the life and dependability of such components, which are damaged by heat energy produced during operation. In addition, thermoelectric modules are utilized to fabricate sensors and modulate the temperature of sensing circuits

Another potential application of thermoelectric technology is thermoelectric cooling or refrigeration. Conventional refrigeration and air conditioning (R & AC) systems use chlorofluorocarbons (CFCs) and hydrochlorofluorocarbons (HCFCs) as heat carrying fluids. Since their environmental impact is very high, intensive attention has been paid to search for novel eco-friendly refrigeration and space conditioning technologies. Thermoelectric coolers (TECs) are an alternative to the current R & AC systems which increases the coefficient of performance (COP) of the cooling

systems. Thermoelectric devices are also used as solar thermoelectric coolers, especially in portable refrigeration applications in the field of exporting and importing perishable items, transportation of medications, and biological materials that must be stored at low temperatures⁵. More inventions utilizing thermoelectric effects are the car-seat systems with air conditioning systems; systems which use Peltier effects directly to reduce the temperature generated during the working of electronic devices, hospital and pharmaceutical applications, and cooling in electronic components⁶.

The majority of thermoelectric materials are inexpensive, less hazardous, and abundant in nature. These factors make thermoelectricity a reliable, green, and clean technology. A wide range of thermoelectric materials with different structures in the forms of undoped, doped, and low dimensional/nanostructured materials have been extensively studied to increase the conversion capacity of thermoelectric devices.

1.2. Thermoelectric phenomena

Generally, thermoelectricity refers to a class of phenomena such as the Seebeck effect, Peltier effect, and Thomson effect. These three effects are collectively known as thermoelectric effects which describe the interconnection between heat and electricity. A material creates voltage when there is a temperature difference across the material and when a voltage is applied to the material, a temperature difference is created in the material.

1.2.1 Seebeck effect

The fundamental aspect of thermoelectric power generation is the Seebeck effect, which describes the generation of electrical energy from the temperature difference. This effect was discovered by Thomas Johan Seebeck in 1821. He discovered that when two dissimilar metals joined together and the junctions of the metals are maintained at different temperatures, then a voltage is induced in the circuit which is proportional to the temperature difference at the junctions and depends on the material of the conductors as shown in Fig 1.1. The electrons in higher temperature end have higher energy and higher velocity than the electrons in the cold region.

Therefore, the electrons from the higher temperature region start migrating to the low temperature region leaving positive ions in the hot end. This process will continue until the electric field developed between the positive ions in the hot end and the excess electrons in the cold end opposes further diffusion of electrons to the cold end. It creates a voltage in the materials ⁷. Thus, his experimental investigations lead to a relationship connecting temperature difference and electricity,

$$\begin{aligned} \text{ie.,} \quad \Delta V &\propto \Delta T \\ \Delta V &= S\Delta T \end{aligned} \quad (1.1)$$

Where the proportionality constant S , known as the Seebeck coefficient or thermopower, is a material property that depends on the temperature. The Seebeck coefficient is measured in units of $\mu\text{V/K}$. The Seebeck coefficient depends upon the density of the state of the material and the difference in the Fermi energy of the cold junction with respect to the hot junction. The sign of the Seebeck coefficient tells about the majority of carriers in the materials. The positive Seebeck coefficient indicates that major carriers are holes and the negative Seebeck coefficient denotes electrons are the dominant carrier in the material.

In 1851, Gustav Magnus discovered that the Seebeck voltage does not depend on the temperature distributions along the materials between the junctions. According to him, the Seebeck coefficient or thermopower is a thermodynamic state function, it depends only on the temperatures of the hot and cold junctions ⁸.

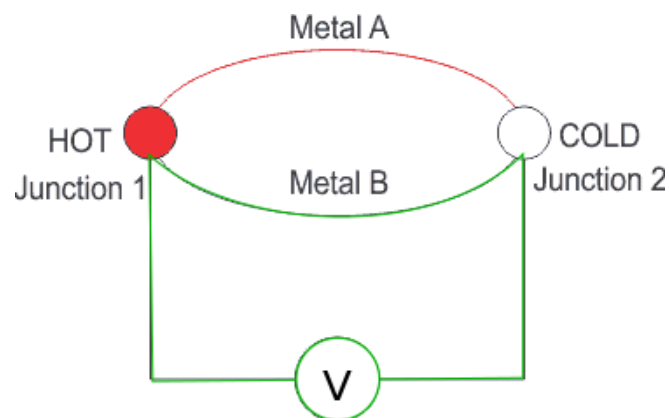


Fig 1.1 Voltage generation in a circuit of dissimilar metals through the Seebeck effect

1.2.2 Peltier Effect

Peltier effect, discovered by Jean Peltier in 1834, describes the thermal effects produced at the junction of dissimilar materials by the application of electric current in the materials as depicted in Fig 1.2. It is the reverse effect of the Seebeck effect, i.e., electrical energy is converted into thermal energy. There occurs absorption of heat Q_C at one junction and liberation of heat Q_H at another junction when a voltage E_{in} is applied to the terminals T_1 and T_2 . Change in the current direction will reverse the direction of heat flow. The sub-atomic level investigation of this effect reveals that the heat liberation/absorption is due to the different energy levels of materials especially in p-type and n-type materials. If the electrons move from p-type material to n-type material, the electrons jump to a higher energy level by absorbing heat energy from the surroundings. When the electrons move from the n-type material to the p-type material, the electron will fall to the low energy state by releasing heat energy to the surroundings.

The heat liberated or absorbed can be expressed as $Q = \pi I$, where π is the Peltier coefficient, defined as the ratio of heat liberated or absorbed to the electrical current passing through the junctions⁹. In 1838, Lenz demonstrated that the direction of current flowing through the junctions determines whether heat is absorbed or liberated in a material.

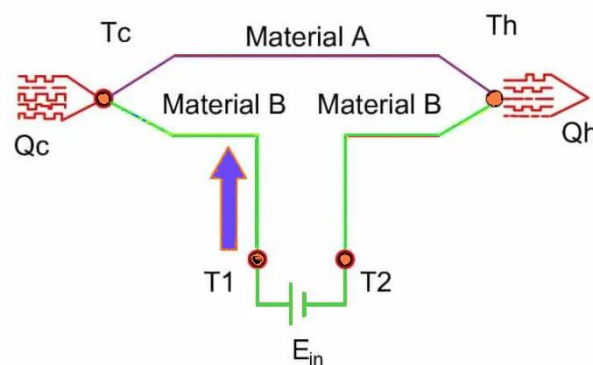


Fig 1.2 Peltier effect

Peltier effect is used for the designing of thermoelectric coolers (TEC) to produce heating/ cooling effects with an improved coefficient of performance (COP) and it is also used in thermoelectric radiant air conditioning systems in which thermoelectric modules are directly used as radiant panels for space heating. Peltier coolers are used as mini refrigerators, for cooling ophthalmic lasers and batteries in electric cars, in night vision devices to cool the image sensor, etc.

1.2.3. Thomson Effect

William Thomson (Lord Kelvin) studied the interrelationship between the Seebeck and Peltier effects and he found that the Peltier coefficient is the Seebeck coefficient times the absolute temperature,

$$\pi = ST \quad (1.2)$$

In 1851, he discovered the third thermoelectric effect, the Thomson effect. When current is passed through a material with a temperature gradient, heat is either absorbed or released. The amount of heat absorbed or released is proportional to the magnitude of current flowing through the material and the temperature gradient. The proportionality constant is called the Thomson coefficient τ .

The heat produced Q when a current I flow through a conductor of temperature gradient ΔT is,

$$Q = \tau I \Delta T \quad (1.3)$$

The Thomson coefficient is related to the Seebeck coefficient through the relation,

$$\tau = T \frac{dS}{dT} \quad (1.4)$$

Equations (1.2) and (1.4) are known as the Thomsons relations. The positive Thomson coefficient improves the efficiency of the thermoelectric cooler, while the negative coefficient decreases the performance.

There are two types of Thomson effects: positive and negative. In the positive Thomson effect, the hot end of the material is at high potential, whereas the cold end

is at low potential. When the current flows from the cold end to the hot end, heat is absorbed, and when it flows from the hot end to the cold end, heat is evolved. Cu, Ag, Sn, Zn, and Cd are some elements that show a positive Thomson effect. In the negative Thomson effect, the cold end is at high potential and the hot end is at low potential. When the current flows from the cold end to the hot end, heat is evolved, and if the current flows from the hot end to the cold end, heat is absorbed. Elements that show negative Thomson effects are Bi, Co, Fe, Pt, etc. the Thomson effect is illustrated in Fig 1.3 where T_0 is the cold junction temperature and $T_0 + \Delta T$ is the hot junction temperature.

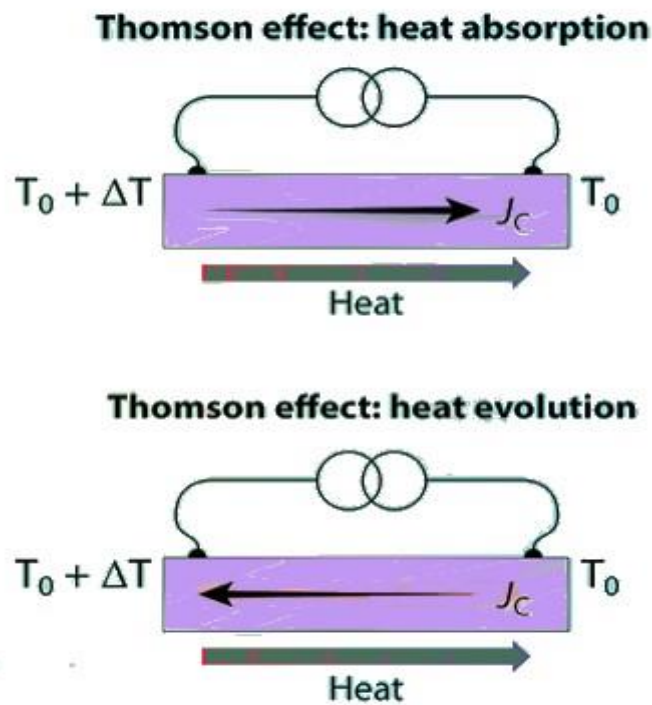


Fig 1.3 Thomson effect

1.3 Thermoelectric power generation and refrigeration

Power generation and refrigeration are the two important applications of thermoelectric materials which are shown in Fig 1.4. The Seebeck effect is the basis of thermoelectric power generation. One junction of p-type and n-type materials is maintained at high temperature and the other is maintained at low temperature, then the charge carriers will move away from the junction creating a voltage across the p

and n terminals, which is proportional to the temperature gradient developed between the hot and cold junctions. During refrigeration as a result of the Peltier effect, when the current flows both the electrons and holes will move away from the junction, thus resulting in cooling of the junction ¹⁰.

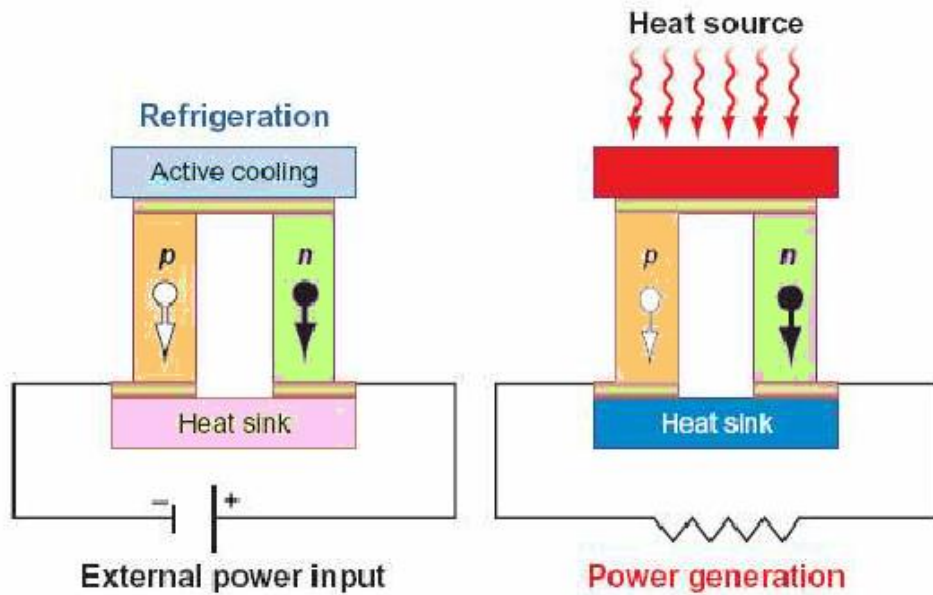


Fig 1.4 Power generation and refrigeration of thermoelectric materials

1.4 Thermoelectric parameters and efficiency

Thermoelectric converting systems are equivalent to heat engines which obey the laws of thermodynamics. The thermoelectric conversion efficiency (η) is given by,

$$\eta = \frac{\text{Energy supplied to the load}}{\text{Heat absorbed at the hot junction}} \quad (1.5)$$

Assuming the electrical conductivity, thermal conductivity and Seebeck coefficient are same at the cold and hot ends of the thermoelectric material, then the efficiency can be expressed as,

$$\eta = \frac{I^2 R}{\lambda(T_H - T_C) - \frac{1}{2} I^2 R} \quad (1.6)$$

Where λ is the thermal conductance, R is the electrical resistance, T_H is the temperature of the hot end and T_C is the temperature of the cold end.

The maximum efficiency η_{\max} is given by,

$$\eta_{\max} = \frac{(T_H - T_C) \sqrt{1 + ZT} - 1}{T_H \sqrt{1 + ZT} + \frac{T_C}{T_H}} \quad (1.7)$$

Here $T = (T_H + T_C)/2$ and $Z = S^2/R\lambda$, the figure of merit. The efficiency depends only on Z when the temperature of the hot (T_H) and cold (T_C) ends are held constant. When Z tends to infinity the efficiency approaches the Carnot limit.

The unit of Z is K^{-1} , therefore, the dimensional figure of merit ZT can be expressed as,

$$ZT = \frac{S^2 \sigma}{\kappa} T \quad (1.8)$$

Where, S is the Seebeck coefficient, σ is the electrical conductivity, κ is the thermal conductivity, and T is the absolute temperature. A good thermoelectric material will have a high Seebeck coefficient to obtain high voltage, and high electrical conductivity to reduce the internal resistance of the material and thereby minimize joule heating, and very low thermal conductivity to maintain large temperature differences¹¹. The term $S^2 \sigma$ is the power factor that assures the electrical transport in thermoelectric materials. The expression for thermoelectric efficiency ensures that it is difficult to attain high electrical conductivity and low thermal conductivity simultaneously. The ultimate goal in achieving the highest thermoelectric performance is to control the flow of electrical current and heat current independently.

Slack suggested that the characteristic of a good thermoelectric material is that, it would behave as a Phonon Glass -Electron Crystal (PGEC). That is, a thermoelectric material would possess the electrical characteristics of a crystal and the thermal properties of an amorphous material or glass¹². But it is very difficult to attain high electrical conductivity and Seebeck coefficient, and low thermal conductivity in the same materials since these three thermoelectric parameters strongly depend on the carrier concentration¹³. Fig 1.5 demonstrates how the parameters vary with carrier concentrations.

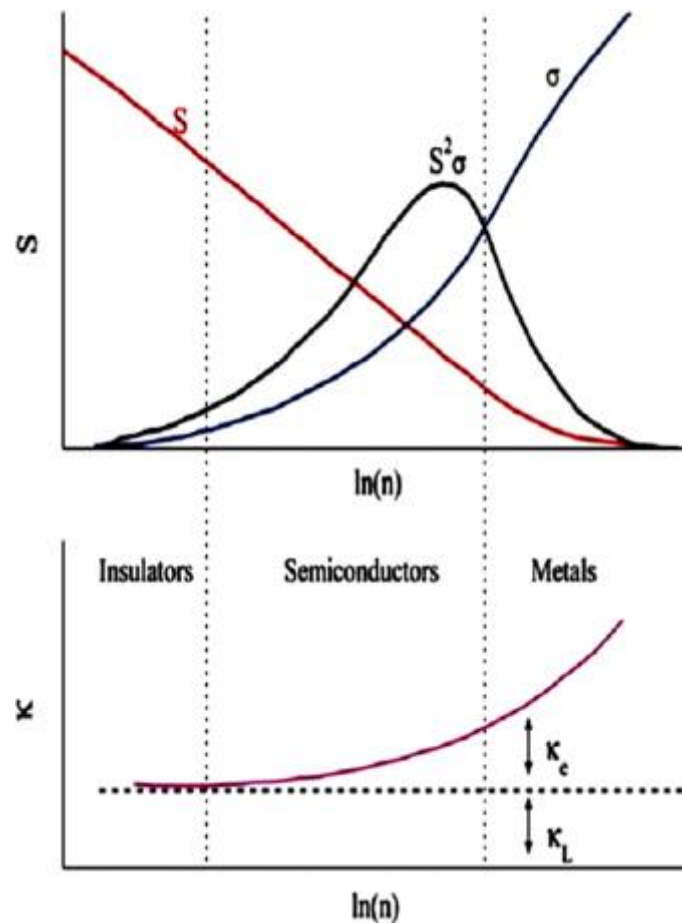


Fig 1.5 Variation of Seebeck coefficient (S), electrical conductivity (σ), and thermal conductivity (κ) with carrier concentration (n)¹⁴

The correlation between the thermoelectric parameters is a barrier in thermoelectric energy conversion, especially in conventional metals. The dependence of carrier concentration among the thermoelectric parameters reveals that semiconductors are the most suitable materials for thermoelectric conversion, as they possess a better power factor ($S^2\sigma$) and minimal thermal conductivity. As shown in Fig, materials with higher carrier concentration have high electrical conductivity but the Seebeck coefficient has an inverse relationship with carrier concentration. This contradiction imposes many difficulties to achieve higher efficiency. But we have to attain a high figure of merit to effectively convert heat into electricity. So, various strategies were adopted to enhance the thermoelectric performance of potential candidates.

1.4.1. Electrical transport properties

Electrical transport properties of thermoelectric materials include electrical conductivity and the Seebeck coefficient. Enhancing these properties will improve the power factor of the materials.

The electrical conductivity of a material is related to the carrier concentration through the relation,

$$\sigma = ne\mu \quad (1.9)$$

Where n is the carrier concentration, e is the electron charge and μ is the mobility. The electrical conductivity enhancement can be done through the introduction of more charge carriers and the increment in carrier mobility.

a) Doping or alloying

It is an effective method to induce more charge carriers by changing the electronic band structure of the host materials¹³. Thus, a dopant atom will create more density of states in the structure of heavily doped material. This will increase the electrical conductivity of the material. At the same time, dopant atoms may act as scattering centers to the charge carriers which will reduce the carrier mobility causing a reduction in conductivity. In semiconductors, a technique known as modulation doping is introduced, which will isolate the free charge carriers from the dopant atoms to reduce the scattering of carriers and the mobility of carriers increases¹⁵. The added dopant atoms are concentrated in a thin dopant layer which is isolated from the main transport path and thereby reduces the impurity scattering¹⁶.

A large Seebeck coefficient can be ensured by inducing one type of charge carrier in the material. If there are two types of carriers in a material, the n-type and p-type conduction will lead the charge carriers to move to the cold end of the material, thereby cancelling the induced Seebeck voltages¹⁷. High carrier concentration will reduce the Seebeck coefficient according to Mott's relation,

$$S = \frac{8\pi^2 k_B^2 m^* T}{3e\hbar^2} \left(\frac{\pi}{3n}\right)^{\frac{2}{3}} \quad (1.10)$$

Where m^* is the effective mass, n is the carrier concentration, and k_B is the Boltzmann constant. Low carrier concentration is preferred to attain a high Seebeck coefficient, insulators and semiconductors have a high Seebeck coefficient because of their low carrier density. The Seebeck coefficient is very low for metals (only a few $\mu\text{V/K}$) and high for semiconductors (a few hundred $\mu\text{V/K}$). Since the Seebeck coefficient depends on the sign of the charge carriers, a good thermoelectric material should be a heavily doped material, either p-type or n-type semiconducting material in order to prevent the simultaneous contribution from both types of charge carriers to the Seebeck coefficient. Seebeck coefficient can be enhanced through dedoping, but it will reduce the electrical conductivity of the material.

As the carrier concentration depends on the Seebeck coefficient and the electrical conductivity, the effective mass is also depending on these two transport parameters. Effective mass increases the Seebeck coefficient but decreases electrical conductivity. The effective mass indicated in Mott's relation is the density of state effective mass (m^*) which increases with flat, narrow bands with a high density of states at the Fermi surface. But heavy carriers will move with very low velocities, and hence their mobility will be low, which causes a decrement in electrical conductivity¹⁸.

b) Low dimensional systems

Low dimensional structures now proved to increase the density of states near the Fermi level and thus increase the Seebeck coefficient. Also, such systems enhance the phonon grain boundary scattering without significantly increasing electron scattering¹⁹. Low dimensionality will provide an opportunity to enhance carrier mobility at a given carrier concentration when quantum confinement effects are employed. Then, doping methods such as modulation doping and δ doping can be effectively utilized in such systems.

c) Resonant levels

Creating distortions in the density of states near the Fermi level can enhance the Seebeck coefficient through the technique known as resonant level mechanism. The

resonant level can be induced by the interaction between the dopant and host materials. The dopants usually having an electron configuration similar to that of the host, and normally the dopants are selected from neighbouring group elements²⁰. The resonant levels can be induced by doping where the impurity band lies in the conduction band or valance band of the host. These levels will cause an increase in the Seebeck coefficient by scattering the conduction electrons and thereby increasing the mobility of the carriers. Dopants which are capable of inducing resonant levels in a phase changing material in the low and high temperature phases are very beneficial in thermoelectric power generation applications. In the case of Cr and I doubly doped PbTe, Cr creates distortion in the conduction band of PbTe causing enhancement of density of states and iodine tunes the position of Fermi level by controlling electron density in the conduction band. The coincidence of the Fermi level with the distorted band will enhance the Seebeck coefficient of PbTe without reducing the electrical conductivity²¹.

d) Energy filtering

Energy filtering is another method to improve the electronic transport properties of a material without causing much reduction in electrical conductivity. Defects such as grain boundaries will scatter the charge carriers and thus decrease the electrical conductivity. But the presence of appropriate energy barriers will filter the low energy carriers and allow high energy carriers to pass through²². When two materials with different Fermi levels come into contact, electron transfer occurs between them. It causes energy band bending near the interfaces of the two materials. The low energy carriers were filtered out by the energy barrier formed due to the band bending. In the absence of an energy barrier, both the low energy carriers and high energy carriers will accumulate at the cold end of the material leading to a low Seebeck coefficient. If there is an energy barrier, it can filter the low energy carriers which are very close to the Fermi level. The height of the energy barrier should not be very large, and if the energy barrier is very large, it will filter all the charge carriers with low and high energies which will reduce the electrical conductivity of the material. If a metal nanoparticle with high Fermi energy is in

contact with a n-type semiconductor with low Fermi energy, then electron transfer takes place from the metal nanoparticle to the semiconductor. It leads to the band bending of the conduction band of the semiconductor at the metal-semiconductor interface. This energy barrier can scatter the electrons with low relaxation time, that is electrons with low energy were scattered causing an increase in the Seebeck coefficient²³. The height of the energy barrier is more important in this mechanism. Otherwise, if the temperature increases, the charge carriers acquire more kinetic energy enough to overcome the potential barrier, and thus the Seebeck coefficient decreases. As a solution to overcome the drawbacks, Jiang Zhang et al. introduced an architecture of hierarchical potential barriers to scatter the low energy carriers effectively in the entire temperature range to enhance the power factor of the material²⁴. Although the energy filtering increases the Seebeck coefficient, it brings a small reduction in electrical conductivity as charge carriers are filtered out. The small decrease in electrical conductivity is compensated by the large increase in the Seebeck coefficient and thereby the power factor is enhanced²⁵.

e) Band tailoring

Band convergence is attained by bringing different bands of different energy into the same energy. The energy of a particular band at a particular symmetry point can be increased or decreased to align with other bands located at another symmetry point through alloying. Relying on the material and position of the band, the energy of the bands may differ with the chemical composition of the alloys and temperature. In order to apply band convergence to improve thermoelectric performance of materials, ensure the presence of another band near to the primary band, which contribute more to the carrier transport. For n-type material, the second band will be situated above the primary band (in energy) and in p-type it is just below the primary band. When different bands are separated within a few energies of k_bT , then those bands can be aligned in terms of energy²⁶. When the bands are converged, N_v , the number of valley degeneracies increases which in turn increases the effective mass (m_d^*) according to the relation,

$$m_d^* = N_v^{2/3} m_b^* \quad (1.11)$$

In band convergence, m_d^* gets heavier, which is identical to effective mass m^* described in the Mott's relation. But the m_b^* , the inertial effective mass remains constant which increases the electrical conductivity. Thus, band convergence increases both the Seebeck coefficient and electrical conductivity. But in band flattening where, the density of states of a single band increase at all energy levels, m_b^* increases keeping N_v constant leading to the suppression of electrical conductivity. So, band convergence is an effective strategy to improve power factor as it enhances Seebeck coefficient and electrical conductivity simultaneously.

1.4.2. Thermal transport

In order to attain higher thermoelectric efficiency, it is essential to reduce the thermal conductivity of the material. For effective power generation, the thermal conductivity should be very small to maintain maximum thermal gradient between the material. Many methods are used to minimize the thermal contribution to thermoelectric efficiency such as nanostructuring, nanoprecipitates, introducing defects such as point defects, dislocation and interfaces to enhance grain boundary scattering^{27, 28}. The total thermal conductivity of a material is the contribution from the electrons (κ_{el}) and phonons (κ_{ph}) or lattice vibrations given by,

$$\kappa_{total} = \kappa_{el} + \kappa_{ph} \quad (1.12)$$

The electronic contribution to thermal conductivity can be determined from the Wiedemann Franz law,

$$\kappa_{el} = L_0 \sigma T \quad (1.13)$$

Where, L_0 is the Lorentz constant and its value is $2.45 \times 10^{-8} \text{ V}^2 \text{ K}^{-8}$. It relates the thermal conductivity in terms of electrical conductivity. So, attempt to reduce the electronic part of thermal conductivity will also reduce the electrical conductivity of the material. Since the electrical conductivity, Seebeck coefficient, and electronic thermal conductivity are the thermoelectric parameters which are closely bound to the carrier concentration and effective mass, deteriorating one parameter will adversely affect the other. Acoustic phonons including short, medium and long

wavelength phonons carry most of the heat in a material and contribute to the total thermal conductivity²⁹. So, it is beneficial to suppress the lattice part of thermal conductivity κ_{ph} since it depends on the phonons or lattice vibrations in the material. The lattice thermal conductivity is given by,

$$\kappa_{ph} = \frac{1}{3}v_s C_V L_{ph} \quad (1.14)$$

Where v_s is the velocity of sound, C_v is the specific heat capacity at constant volume and L_{ph} is the phonon mean free path. Materials which contain heavy elements (low v_s), solid solutions (short mean free path, L_{ph}) and many atoms in a unit cell (small C_v) possess very low thermal conductivity and good for thermoelectric conversion. Since C_v , v_s are constants, the lattice thermal conductivity can be controlled by reducing the phonon mean free path. Phonon scattering will enhance when the dimension of the dopants or defects were comparable to the mean free path. Nanostructures with dimensions smaller than the mean free path of phonons but greater than that of electrons can effectively reduce the lattice thermal conductivity while preserving electrical conductivity in a material. The mean free path of phonons is larger than the electrons. Nanostructuring induces large density of interfaces in which phonons of large mean free path will scatter more effectively than the electrons. Phonon scattering is achieved through different methods such as mass fluctuation scattering (a mixed crystal in ternary or quaternary compounds), grain boundary scattering, and the interface scattering in thin films or multilayer systems. Rattling scattering or introducing atoms inside a cage-like structure will also resonantly scatter the acoustic phonons.

The point defects such as vacancies, interstitials and substitutional defects formed in the material act as phonon scattering centres especially for the high frequency phonons and reduce the lattice thermal conductivity. Strong scattering of phonons occurs when introducing a foreign atom with similar valance in host lattice but does not scatter the charge carriers. Substitution of an atom with large mass and size difference will maximize the phonon scattering. Vacancies are effective point defects which cause large phonon scattering on account of the missing atom and missing

interatomic linkage. Vacancies are good electron acceptors also which increases the electrical conductivity of the material ³⁰.

1.5 Theory of thermoelectric phenomena in metals and semiconductors

The electronic conduction in solids was explained by Drude and Lorentz, by using the principles of classical physics but it is failed to explain the conduction mechanism properly. Sommerfield's quantum free electron theory can explain the electronic conduction in solids on the basis of the interaction between the electron and the periodic potential. As a result of this interaction, the energy of the electrons lies in discrete bands separated by energy gap or forbidden region.

According to the Fermi Dirac distribution function $f_0(E)$ (Fermi factor), the probability of an electron to occupy in a given energy level E under thermal equilibrium is given by,

$$f_0(E) = \left[\exp\left(\frac{E-E_F}{kT}\right) + 1 \right]^{-1} \quad (1.15)$$

Where k is the Boltzmann's constant and E_F depends up on the total number of electrons that can be occupied.

$f_0(E) = 0$ when $E - E_F \gg kT$ and $f_0(E) = 1$ when $E - E_F \ll kT$. When $f_0(E) = 1/2$ the energy E_F is known as the Fermi energy.

If $g(E)$ is the number of electron levels permitted within the energy range E and $E+dE$, then the total number of electrons is,

$$n = \int_0^{\infty} f_0(E)g(E) dE \quad (1.16)$$

$g(E)$, the density of state is small but increases rapidly at the conduction band edge. Therefore, for a metal, the Fermi level lies within the conduction band and there will be a large number of conduction electrons. In the case of an insulator, the Fermi level lies within the band gap and there will be no electrons for the conduction. The Fermi level of semiconductors is close to the conduction band edge and since there will be a small number of electrons for conduction, the electrical conductivity of

semiconductors lies between metals and insulators. The energy band diagram of metals, insulators, semiconductors and semi metals are shown in Fig 1.6.

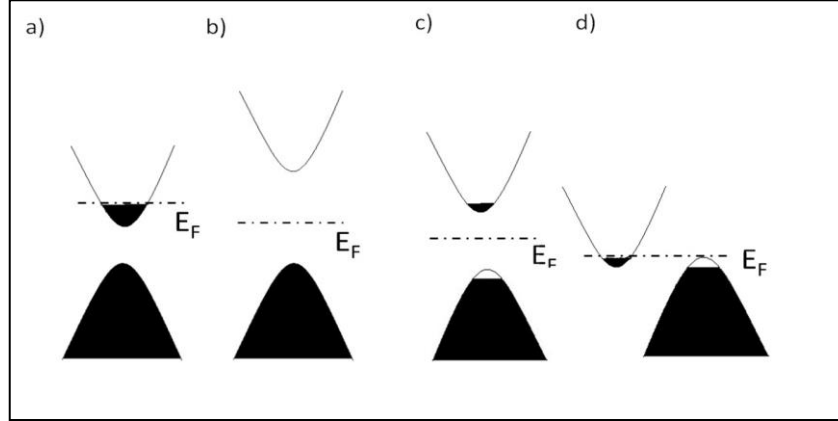


Fig 1.6 The energy band diagram of (a) metals (b) insulator (c) semiconductor (d) semimetal

The density of states near the conduction band edge is expressed as,

$$g(E)dE = \frac{4\pi(2m^*)^{3/2}}{h^3} \quad (1.17)$$

If the distribution function f disturbed from f_0 (the equilibrium value of f) then, the rate of change of f is given by the relation,

$$\frac{df(E)}{dt} = -\frac{f(E)-f_0(E)}{\tau_e} \quad (1.18)$$

Here as an approximation, τ_e is considered as the relaxation time expressed as $\tau_e = \tau_0 E^r$, where τ_0 and E^r are the constants of a given scattering process. For materials in which the charge carrier scattering mechanism is mainly due to the acoustic mode lattice vibrations, $r = -1/2$ and in the case of ionised impurity scattering $r = 3/2$.

The transport mechanism in metals and semiconductors are explained on the basis of Boltzmann equation which relates the effects of applied field and scattering of carriers. Suppose the disturbance to the distribution is small, then it can be expressed as,

$$\frac{f(E)-f_0(E)}{\tau_e} = u \frac{df_0(E)}{dE} \left(\frac{dE_F}{dx} + \frac{(E-E_F)}{T} \frac{dT}{dx} \right) \quad (1.19)$$

Where, u and E_F are the velocity of the carriers in the X-direction and Fermi energy respectively. From this equation the expression for current density and heat flux density can be deduced.

The electric current density i ,

$$i = \mp \int_0^{\infty} e u f(E) g(E) dE \quad (1.20)$$

Here e is the electronic charge.

The heat flux density,

$$j = \int_0^{\infty} u(E - E_F) f(E) g(E) dE \quad (1.21)$$

$(E - E_F)$ is the energy transported by the carrier. When $f=f_0$, there is no flow of any kind of carriers. The drift velocity of the carriers is small part of the total velocity, so it is better to replace u with $2E/3m^*$. Then the current density and heat flux can be rewrite as,

$$i = \mp \frac{2e}{3m^*} \int_0^{\infty} g(E) \tau_e E \frac{df_0(E)}{dE} \left\{ \frac{dE_F}{dx} + \frac{(E - E_F)}{T} \frac{dT}{dx} \right\} dE \quad (1.22)$$

$$j = \pm \frac{E_F}{e} i + \frac{2}{3m^*} \int_0^{\infty} g(E) \tau_e E^2 \frac{df_0(E)}{dE} \left\{ \frac{dE_F}{dx} + \frac{(E - E_F)}{T} \frac{dT}{dx} \right\} dE \quad (1.23)$$

The transport parameters can be determined by applying appropriate boundary conditions. The electrical conductivity is the ratio of i to the electric field when the temperature gradient dT/dx is zero. ie.,

$$\sigma = - \frac{2e^2}{3m^*} \int g(E) \tau_e \frac{df_0(E)}{dE} dE \quad (1.24)$$

κ_e , the electronic contribution to the thermal conductivity is equal to the ratio of j to $-dT/dx$ when the electric current is zero.

$$\kappa_e = \frac{2}{3m^*T} \left(\left\{ \frac{\left[\int_0^\infty g(E) \tau_e E^2 \frac{df_0(E)}{dE} dE \right]^2}{\int_0^\infty g(E) \tau_e \frac{df_0(E)}{dE} dE} \right\} - \int_0^\infty g(E) \tau_e E^3 \frac{df_0(E)}{dE} dE \right) \quad (1.25)$$

The Seebeck coefficient S under the same conditions is given by the ratio of the electric field to the temperature gradient,

$$S = \pm \frac{1}{eT} \left[E_F - \frac{\int_0^\infty g(E) \tau_e E^2 \frac{df_0(E)}{dE} dE}{\int_0^\infty g(E) \tau_e E \frac{df_0(E)}{dE} dE} \right] \quad (1.26)$$

The three transport parameters σ , κ_e and S can be expressed in the form,

$$K_s = -\frac{2T}{3m^*} \int_0^\infty g(E) \tau_e E^{s+1} \frac{df_0(E)}{dE} dE \quad (1.27)$$

The terms τ_e and g can be eliminated in favour of m^* , r and τ_0 . Then K_s is rewrite as,

$$K_s = \frac{8\pi}{3} \left(\frac{2}{\hbar^2} \right)^{\frac{3}{2}} (m^*)^{\frac{1}{2}} T \tau_0 \left(S + r + \frac{3}{2} \right) (kT)^{s+r+\frac{3}{2}} F_{s+r+\frac{1}{2}} \quad (1.28)$$

The function F_n are the Fermi Dirac integral functions and r is the scattering variable. The transport parameters in terms of K_s are,

$$\sigma = \frac{e^2}{T} K_1 \quad (1.29)$$

$$\kappa_e = \frac{1}{T^2} \left(K_2 - \frac{K_1^2}{K_0} \right) \quad (1.30)$$

$$S = \pm \frac{1}{eT} \left(E_F - \frac{K_1}{K_0} \right) \quad (1.31)$$

The above three (1.23, 1.24, 1.25) equations relate the thermoelectric figure of merit to the scattering parameter, carrier effective mass and Fermi energy.

The degenerate approximation can be applied to materials with $E_F > 4kT$, so this approximation can be employed in metals where $E_F \gg kT$. The expression of the Fermi Dirac integral for a degenerate conductor is

$$F_n(\eta) = \frac{\eta^{n+1}}{n+1} + n\eta^{n-1} \frac{\pi^2}{6} + n(n-1)(n-2)\eta^{n-3} \frac{7\pi^4}{360} + \dots \quad (1.32)$$

This series converges rapidly, and only the first term in this series is required to find the electrical conductivity.

$$\sigma = \frac{8\pi}{3} \left(\frac{2}{h^2}\right)^{\frac{3}{2}} e^2 (m^*)^{\frac{1}{2}} \tau_0 E_F^{r+\frac{3}{2}} \quad (1.33)$$

The Lorentz constant, L is found from the ratio of $\sigma T / \kappa_c$,

$$L = \frac{\pi^2}{3} \left(\frac{k}{e}\right)^2 \quad (1.34)$$

The Seebeck coefficient can be deduced from the first two terms of the equation (1.26) and is given by,

$$S = \mp \frac{\pi^2 k}{3 e} \frac{(r+\frac{3}{2})}{\eta} \quad (1.35)$$

In semiconductors, the nondegenerate or classical approximation is most applicable, where $\eta < 2kT$. The Fermi Dirac integral for nondegenerate conductor is,

$$F_n(\eta) = \exp(\eta) \Gamma(n+1) \quad (1.36)$$

Then the integral K_s becomes,

$$K_s = \frac{8\pi}{3} \left(\frac{2}{h^3}\right)^{\frac{3}{2}} (m^*)^{\frac{1}{2}} T \tau_0 (kT)^{s+r+\frac{3}{2}} \Gamma\left(s+r+\frac{5}{2}\right) \exp(\eta) \quad (1.37)$$

The electrical conductivity is,

$$\sigma = \frac{8\pi}{3} \left(\frac{2}{h^3}\right)^{\frac{3}{2}} e^2 (m^*)^{\frac{1}{2}} T \tau_0 (kT)^{r+\frac{3}{2}} \Gamma\left(r+\frac{5}{2}\right) \exp(\eta) \quad (1.38)$$

Drude model suggested that $\sigma = ne\mu$, here, n and μ are carrier density and mobility respectively.

$$n = 2 \left(\frac{2\pi m^* kT}{h^2}\right)^{\frac{3}{2}} \exp(\eta) \quad (1.39)$$

$$\mu = \frac{4}{3\sqrt{\pi}} \Gamma\left(r + \frac{5}{2}\right) \frac{e\tau_0(kT)^r}{m^*} \quad (1.40)$$

The Seebeck coefficient of non-degenerate semiconductor is expressed as,

$$S = \mp \frac{k}{e} \left[\eta - \left(r + \frac{5}{2} \right) \right] \quad (1.41)$$

The Lorentz number,

$$L = \left(\frac{k}{e} \right)^2 \left(r + \frac{5}{2} \right) \quad (1.42)$$

Semiconductors are widely used for thermoelectric applications since the lattice component of thermal conductivity is dominant over the electronic thermal conductivity and the Seebeck coefficient of semiconductors are higher than the metals. Because of these, thermoelectric research is focussed on semiconducting materials by enhancing the Seebeck coefficient without sacrificing electrical conductivity.

1.6 Materials for waste heat management

There are many materials capable of converting heat energy into electricity. Some materials have thermoelectric efficiency greater than 1. Materials with $ZT > 3$ are capable for thermoelectric refrigeration and materials possessing $ZT > 2$ are used for thermoelectric power generation. So, thermoelectric converting systems made up of such materials with higher efficiency can replace conventional energy converting systems³¹. Good thermoelectric materials obey the Phonon Glass- Electron Crystal (PGEC) approach to a great extent. But in most thermoelectric materials, the criteria of high electrical transport and low thermal conduction could not meet simultaneously. Some materials will satisfy these requirements to a considerable degree and possess high thermoelectric efficiency. But despite having high thermoelectric conversion efficiency, some of the materials have disadvantages such as not being eco-friendly, and less abundant, instability at elevated temperatures etc. There are so many materials that are highly abundant, nontoxic, and suitable for thermoelectric conversion in small and large sectors of energy production systems as well as in the low temperature and high temperature regions. Fig 1.7 represents the

state-of-the-art thermoelectric materials. The discussion on different thermoelectric materials will give an insight into the various method to be adopted to enhance the thermoelectric conversion efficiency of materials.

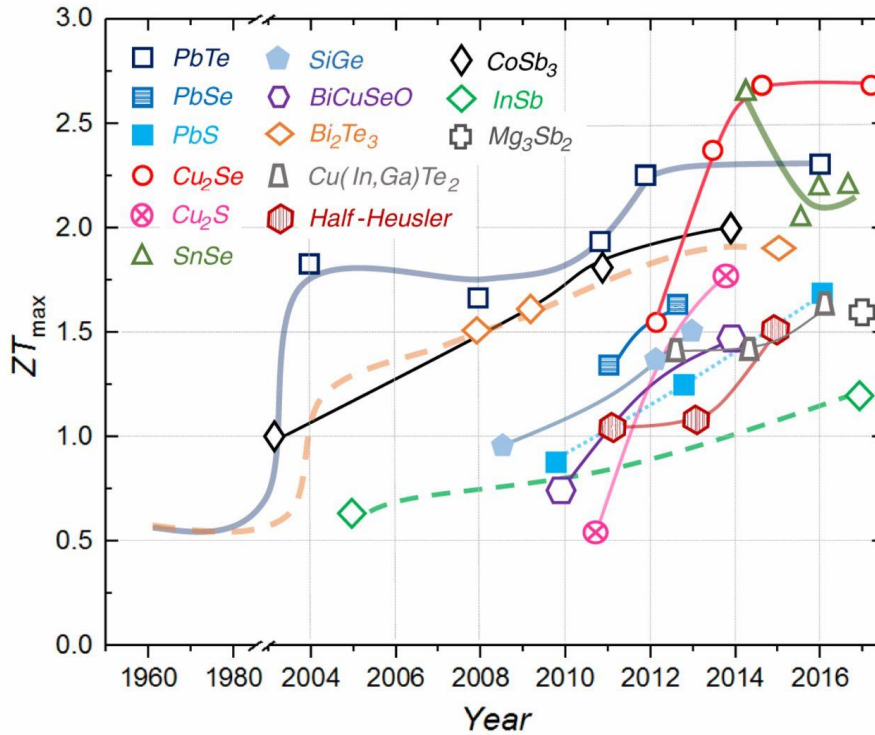


Fig 1.7 State-of-the-art thermoelectric materials ³²

1.6.1 Chalcogenides

Chalcogenides are compounds formed from chalcogen atoms like sulphur, tellurium, and selenium. Metal chalcogenide-based compounds are heavier compounds that are beneficial for reducing the thermal conductivity of the compounds. Because of their low electronegativity, the bonds in these materials are less covalent which leads to a higher power factor. For decades, telluride materials such as Bi₂Te₃ and PbTe are the most studied thermoelectric chalcogenide materials.

Bi₂Te₃ based materials are considered as the best thermoelectric materials for room temperature thermoelectric applications. The structure of Bi₂Te₃ allows for electronic doping and alloying without causing much reduction in mobility. The thermoelectric performance can be increased above room temperature by increasing the band gap through alloying with Sb₂Te₃ and Bi₂Se. Alloying with these materials

may cause band convergence which may increase the density of states and reduce the lattice thermal conductivity, and hence enhance the figure of merit ³³.

PbTe found in both n-type and p-type forms, possesses high thermoelectric efficiency at elevated temperatures. n-type PbTe attained a figure of merit of 1.2 between temperatures 700 K and 850 K ³⁴ and ZT of 2.2 at 800 K attained in co-doped lead antimony silver telluride ($\text{AgPb}_{18}\text{SbTe}_{20}$) through the inclusion of nanodomains ³⁵. Thallium telluride are attained attention since 2001, due to its high figure of merit of 1.2 with a very low lattice thermal conductivity of $0.4 \text{ Wm}^{-1} \text{ K}^{-1}$

SnSe is a p-type thermoelectric material, which can achieve lattice thermal conductivity $< 0.4 \text{ Wm}^{-1} \text{ K}^{-1}$ at 923 K and exhibit immense thermoelectric efficiency greater than 2.3 even without doping ³⁶. Doping in SnSe with donor and acceptor atoms is not successful because most dopants are rejected from the SnSe structure or the solubility limit of such dopants is very low. It is due to the layered anisotropic structure of SnSe and the highly covalent bonding around the Sn and Se atoms may destabilize guest atoms with large differences in chemical character. The enhanced Seebeck coefficient and high-power factor observed in SnSe are due to the Fermi level shift into the valance band up on hole doping which will create many Fermi level pockets in the structure ³⁷.

1.6.2 Skutterudites

Skutterudites are cubic structures with eight AB_3 groups, where A is a transition metal, such as Co, Ir, and Rh and B is pnictide elements like P, As, and Sb etc. The most investigated skutterudites thermoelectric are materials based on antimony such as CoSb_3 because of their high mobility, high atomic mass, and improved electrical conductivity and Seebeck coefficients. CoSb_3 is the most studied skutterudite, which has a power factor of $30 \mu\text{W}/\text{cm}^{-1}\text{K}^{-1}$, but its thermal conductivity is very high, $8.9 \text{ Wm}^{-1}\text{K}^{-1}$. Efforts are made to bring the thermal conductivity to an extremely low value. Generally, skutterudite structures contain voids and attempting to fill the voids within the structure with small diameter and large mass interstitials such as rare-earth ions will drastically reduce the thermal conductivity of these materials. Such guest atoms in the voids act as independent oscillators or ‘rattlers’ in the filled

skutterudites that interact with the normal phonon modes to reduce the lattice thermal conductivity. Rattlers also improve electrical conductivity, since the fillers are generally electropositive atoms which contributes more carriers to the structure. Rattlers which are more loosely bound will produce low frequency local vibrational modes and are more efficient to scatter the low frequency heat carrying phonons. The voids filled with heavier and smaller ions will produce more defects leading to a decrement in thermal conductivity³⁸. Yb-filled skutterudites yield a figure of merit of 1.26 at 800 K and a lowest thermal conductivity of $1.8 \text{ Wm}^{-1}\text{K}^{-1}$, proving that rare earth elements are very efficient for creating additional vibrational modes at low frequencies and thereby scatter phonons and reduce the thermal conductivity³⁹. Nanocomposites and nanostructuring induces more defects in the form of grain boundaries and interfaces which reduce the thermal conductivity of skutterudite structures.

1.6.3 Half-Heusler alloys

Potential thermoelectric material Half Heusler alloys are intermetallic compounds with compositions XYZ, where X and Y are transition metals. X is the least electronegative element, sometimes Y includes the most electronegative f-block rare earth element and Z is a p-block element. The most studied half Heusler systems are MNiSn and MCoSb (where, M=Zr, Ti, Hf). These are small band gap semiconductors with a gap of 0.1 eV-0.5 eV. These materials have an MgAgAs crystal structure with three interpenetrating fcc sublattices with one vacant Ni sublattice. Half Heusler alloys possess very small electrical resistivity and a high negative Seebeck coefficient. They are stable at high temperatures and have high power factors. But large thermal conductivity limits their application in thermoelectric power generation. Many current researches are focused to reduce the thermal conductivity while maintaining a high power factor. Chen et al. reported ZT of 1.2 with power factor of 5 mW/mK^2 in (Hf, Zr)NiSn half Heusler system⁴⁰.

1.6.4 Clathrates

Clathrates are another class of thermoelectric materials, and these materials are cage like structures that allow the rattling mechanism to tune the thermal conductivity of

the crystal structure. There are many types of clathrates, the type-I clathrates are represented by the formula $X_2Y_6E_{46}$ where X and Y are alkali, alkaline earth, or rare earth metals guest atoms and E is Si, Ge, or Sn. The material $Ba_8Ga_{16}Ge_{30}$ is the best clathrates with high thermoelectric conversion efficiency.

The distinct feature of clathrates from other thermoelectric is the crystal structure because they are characteristic the spatial separation of two substructures - the host clathrate framework and rattling guests. The clathrate framework ensures the effective transport of charge carriers to improve the electrical conductivity and Seebeck coefficient, while the rattling guest in the cage like framework reduces the thermal conductivity by increasing phonon scattering or decreasing the phonon group velocity. The spatial separation of host-guest structures in the clathrates is the manifestation of the PGEC approach introduced by Slack. The introduction of rare-earth guests and formation of complex superstructure will drastically reduce the thermal conductivity in narrow band gap clathrates ⁴¹.

There are no clathrates show pure metallic behaviour, the electrical conductivity of most of the clathrates lies between the metallic and semiconducting regime. At high temperatures, clathrates are very good conductors and at low temperatures, many of the clathrates show very high electrical resistivity. But many of the Si based clathrates are superconducting at below 10 K.

1.6.5 Oxide materials

The largest figure of merit ($ZT > 1$) can be achieved with the tellurium, selenium, germanium-based materials. But these materials are not stable at high temperatures and are toxic in nature. Oxides are promising thermoelectric materials capable of harvesting waste heat in the high temperature region. The figure of merit of the oxides is inferior to the above-mentioned materials, but they possess high temperature and chemical stability, and they cause less environmental issues.

Layered cobaltites such as $Ca_3Co_4O_9$, Na_xCoO_2 are the two p-type oxide thermoelectric materials. These materials are formed from alkali or alkaline-earth cobaltite compounds with layered structures. Bismuth is the most used dopant in

$\text{Ca}_3\text{Co}_4\text{O}_9$ which increases both electrical conductivity and Seebeck coefficient and decrease thermal conductivity. Silver addition causes an increase in electrical conductivity due to the increment in carrier concentration and mobility. The massive silver dopant may increase or decrease the thermopower but decrease the thermal conductivity. Most of the transition metal doping increases the thermopower of $\text{Ca}_3\text{Co}_4\text{O}_9$ rather than enhancing the electrical conductivity. Rare-earth doped $\text{Ca}_3\text{Co}_4\text{O}_9$ shows an improved Seebeck coefficient and decrement in electrical conductivity, but these dopants reduce thermal conductivity of the material⁴². The electrical conductivity of layered cobaltite Na_xCoO_2 is greater than $\text{Ca}_3\text{Co}_4\text{O}_9$. Silver doping in Na_xCoO_2 increases both electrical conductivity and thermopower, and causes reduction in thermal conductivity, but lanthanide dopants decrease both electrical and thermal conductivities causing no improvement in thermoelectric efficiency.

Among the n-type oxides, SrTiO_3 , CaMnO_3 , and ZnO are promising materials in thermoelectric conversion. SrTiO_3 has a perovskite structure, but when doped it can form superlattice structures, that reduce the thermal conductivity of the material. The electrical conductivity of SrTiO_3 can be tuned from insulating to metallic with the addition of La^{3+} and Nb^{5+} ⁴³. CaMnO_3 has higher electrical resistivity and thermal conductivity, but its extremely high Seebeck coefficient makes it a good thermoelectric material. The addition of a high valent cation into the CaMnO_3 structure will increase electrical conductivity due to the increase in charge carrier concentration. The size difference between the lanthanides and Ca^{2+} will reduce the lattice thermal conductivity⁴⁴.

This thesis is based on the thermoelectric properties of doped zinc oxide. ZnO is a promising metal oxide used to harvest electricity from waste heat. It is the most investigated high temperature oxide thermoelectric material and the properties of ZnO are discussed briefly.

ZnO is a wide band gap n-type semiconductor. Since it has interesting electrical and magnetic properties, it is widely used in optoelectronic, field effect transistors, solar cells, photoluminescence applications etc. Zn is considered as a 3d transition metal,

but ZnO is not a transition metal oxide as its 3d orbital of Zn^{2+} is fully filled. Generally, the valence band of metal oxides mainly consists of the 2p orbital of the O^{2-} anions. The empty or half-filled orbitals with the lowest energy in the metal oxide cation dominate the characteristics of the conduction band. The conduction electrons in the 3d transition metal oxides are greatly influenced by the 3d orbitals of the metal cations. But the conduction band of ZnO mainly consists of the lowest unoccupied 4s and 4p orbital of Zn^{2+} , so the conduction electrons have high mobility. The large electronegativity of Zn and its low ionicity and a strong preference for sp^3 hybridization of the Zn-O bonds leads to high carrier mobility in ZnO materials⁴⁵.

Since ZnO has excellent electronic transport properties, but high thermal conductivity limits its thermoelectric performance. The high thermal transport in ZnO arises mainly from the hexagonal wurtzite lattice structure which results in the increased phonon or lattice vibrations, and the strong interaction between the ionic and covalent bonds⁴⁶. Doping is a tool to tailor the electrical, chemical, magnetic, and optical properties of ZnO. Doping induces more charge carriers into the lattice structure and increases the electrical conductivity of ZnO. The thermal conductivity of ZnO can be reduced by doping and nanostructuring which increases the phonon scattering in the material. Many dopants either as single dopants and codopant are used to enhance the thermoelectric efficiency of ZnO. Nanostructured ZnO materials increase the electrical transport while reducing the lattice thermal conductivity.

1.7 Methods to enhance thermoelectric properties of zinc oxide

1.7.1. Doping

Doping is an effective method to tune the thermoelectric properties of ZnO which enhances the electrical transport properties by inducing more charge carriers and alter the electronic band structure of the host structure. The addition of foreign atoms in ZnO inhibits the grain growth and reduces the thermal conductivity of the material. But above the optimum doping concentration, the excess number of charge carriers will decrease the Seebeck coefficient of ZnO, which will affect the overall thermoelectric performance of ZnO. Although doping enhances the thermoelectric

performance of ZnO, single doping shows individualized advantages and demerits. Al doping increases electrical conductivity as a result of the increased carrier concentration, without decreasing the Seebeck coefficient⁴⁷. But Sn doping shows enhancement in electrical conductivity, but the presence of high carrier concentration reduces the Seebeck coefficient⁴⁸. Mixed or multiple doping of Al and Sn may enhance the thermoelectric properties of ZnO with higher electrical conductivity and Seebeck coefficient. So, the inclusion of more than one atom is an effective strategy to tune the thermoelectric efficiency of ZnO.

1.7.2 Nanostructuring

Nanostructuring will reduce the thermal conductivity of many thermoelectric materials and enhances thermoelectric efficiency. Nanostructuring refines the grain size and strengthens the phonon scattering at the grain boundaries which result in low thermal conductivity. Since nanostructuring will also scatter the electrons in the material, it may cause a reduction in the power factor of ZnO. So, a novel approach to enhance the power factor and reduce thermal conductivity is the simultaneous application of doping and nanostructuring into the same material.

1.7.3 Quantum confinement

The mechanisms to improve the efficiency in low dimensional systems are to reduce the lattice component of thermal conductivity due to the size effect and improve the power factor by quantum confinement effect which enhance the density of states in one dimensional quantum wires/nanowires and zero dimensional quantum dots/nanoparticles⁴⁹. Nanostructured thin films will enhance the density of states which leads to enhancement in the Seebeck coefficient and thereby improves the thermoelectric efficiency of ZnO.

1.8 Motivation and objectives

The most suitable means to overcome the current energy depletion is to switch to renewable energy sources. Most of the energy generating systems release a huge amount of waste heat, which creates many environmental issues. Thermoelectricity is an effective energy harvesting method and it is considered as the most reliable

method of thermal management. There are many thermoelectric materials but some materials are not eco-friendly, less abundant, and unstable at elevated temperatures. This causes the scientific community to search for eco-friendly high temperature thermoelectric materials with high thermoelectric efficiency.

The objective of this work is to search for new oxide materials for the conversion of heat into electricity. Since ZnO based materials are suitable for high temperature thermoelectric energy conversion, this investigation is focussed on how to enhance the thermoelectric efficiency of ZnO. The dual doping technique, which introduces more carriers and more defects into the crystal structure than single doping, is employed to enhance the efficiency of ZnO. The polycrystalline materials of dual doped ZnO materials were synthesized through the solid-state reaction method. Dopants such as metallic conductors, and rare earth elements are used for the structural modifications to tailor the thermoelectric properties of zinc oxide.

References

1. M. H. Elsheikh, D. A. Shnawah, M. F. M. Sabri, S. B. M. Said, M. H. Hassan, M. B. A. Bashir and M. Mohamad, *Renewable and sustainable energy reviews* **30**, 337-355 (2014).
2. M. Von Lukowicz, E. Abbe, T. Schmiel and M. Tajmar, *Energies* **9** (7), 541 (2016).
3. H. Mamur, Ö. F. Dilmaç, J. Begum and M. R. A. Bhuiyan, *Cleaner Materials* **2**, 100030 (2021).
4. M. S. b. Dzulkfli, A. Pesyridis and D. Gohil, *Energies* **13** (14), 3742 (2020).
5. S. A. Abdul-Wahab, A. Elkamel, A. M. Al-Damkhi, A. Is' Haq, H. S. Al-Rubai'ey, A. K. Al-Battashi, A. R. Al-Tamimi, K. H. Al-Mamari and M. U. Chutani, *Renewable Energy* **34** (1), 30-34 (2009).
6. S. B. Riffat and X. Ma, *Applied thermal engineering* **23** (8), 913-935 (2003).
7. S. Kasap, Canada: Department of Electrical Engineering University of Saskatchewan (2001).
8. A. Ly, University of California, Irvine, 2018.
9. C. Godart, A. P. Gonçalves, E. Lopes and B. Villeroy, presented at the Properties and Applications of Thermoelectric Materials: The Search for New Materials for Thermoelectric Devices, 2009 (unpublished).
10. F. J. DiSalvo, *Science* **285** (5428), 703-706 (1999).
11. M. A. Zoui, S. Bentouba, J. G. Stocholm and M. Bourouis, *Energies* **13** (14), 3606 (2020).
12. D. M. Rowe, *CRC handbook of thermoelectrics*. (CRC press, 2018).
13. S. Lv, Z. Qian, D. Hu, X. Li and W. He, *Energies* **13** (12), 3142 (2020).
14. Z.-G. Chen, G. Han, L. Yang, L. Cheng and J. Zou, *Progress in Natural Science: Materials International* **22** (6), 535-549 (2012).
15. D. Wang, X.-B. Li and H.-B. Sun, *Nano Letters* **21** (14), 6298-6303 (2021).
16. B. Yu, M. Zebarjadi, H. Wang, K. Lukas, H. Wang, D. Wang, C. Opeil, M. Dresselhaus, G. Chen and Z. Ren, *Nano letters* **12** (4), 2077-2082 (2012).
17. G. J. Snyder and E. S. Toberer, *Nature materials* **7** (2), 105-114 (2008).
18. A. M. Dehkordi, M. Zebarjadi, J. He and T. M. Tritt, *Materials Science and Engineering: R: Reports* **97**, 1-22 (2015).
19. M. Dresselhaus, G. Dresselhaus, X. Sun, Z. Zhang, S. Cronin and T. Koga, *Physics of the Solid State* **41**, 679-682 (1999).
20. L. Wu, X. Li, S. Wang, T. Zhang, J. Yang, W. Zhang, L. Chen and J. Yang, *NPG Asia Materials* **9** (1), e343-e343 (2017).

21. B. Paul, P. Rawat and P. Banerji, *Applied Physics Letters* **98** (26), 262101 (2011).
22. P. Pradyumnan and T. Parvathy, in *Nanotechnology-Based E-noses* (Elsevier, 2023), pp. 165-192.
23. X. Guan and J. Ouyang, *CCS Chemistry* **3** (10), 2415-2427 (2021).
24. J. Zhang, D. Wu, D. He, D. Feng, M. Yin, X. Qin and J. He, *Advanced Materials* **29** (39), 1703148 (2017).
25. V. Nicolosi, A. Pakdel, Q. Guo and T. Mori, (2018).
26. K. H. Lee, S.-i. Kim, H.-S. Kim and S. W. Kim, *ACS Applied Energy Materials* **3** (3), 2214-2223 (2020).
27. M. Ohtaki, *Journal of the Ceramic Society of Japan* **119** (1395), 770-775 (2011).
28. A. Nag and V. Shubha, *Journal of electronic materials* **43**, 962-977 (2014).
29. X. Zhang and L.-D. Zhao, *Journal of Materiomics* **1** (2), 92-105 (2015).
30. C. Wan, Y. Wang, N. Wang, W. Norimatsu, M. Kusunoki and K. Koumoto, *Science and Technology of Advanced Materials* (2010).
31. K. B. Masood, P. Kumar, R. Singh and J. Singh, *Journal of Physics Communications* **2** (6), 062001 (2018).
32. J. He and T. M. Tritt, *Science* **357** (6358), eaak9997 (2017).
33. I. T. Witting, T. C. Chasapis, F. Ricci, M. Peters, N. A. Heinz, G. Hautier and G. J. Snyder, *Advanced Electronic Materials* **5** (6), 1800904 (2019).
34. Y. Pei, A. LaLonde, S. Iwanaga and G. J. Snyder, *Energy & Environmental Science* **4** (6), 2085-2089 (2011).
35. K. F. Hsu, S. Loo, F. Guo, W. Chen, J. S. Dyck, C. Uher, T. Hogan, E. Polychroniadis and M. G. Kanatzidis, *Science* **303** (5659), 818-821 (2004).
36. L.-D. Zhao, S.-H. Lo, Y. Zhang, H. Sun, G. Tan, C. Uher, C. Wolverton, V. P. Dravid and M. G. Kanatzidis, *nature* **508** (7496), 373-377 (2014).
37. L.-D. Zhao, C. Chang, G. Tan and M. G. Kanatzidis, *Energy & Environmental Science* **9** (10), 3044-3060 (2016).
38. T. M. Tritt, (2002).
39. M. Rull-Bravo, A. Moure, J. Fernández and M. Martín-González, *Rsc Advances* **5** (52), 41653-41667 (2015).
40. L. Chen, S. Gao, X. Zeng, A. Mehdizadeh Dehkordi, T. Tritt and S. Poon, *Applied Physics Letters* **107** (4), 041902 (2015).
41. A. V. Shevelkov, *Thermoelectrics for Power Generation—A Look at Trends in the Technology*; Nikitin, M., Skipidarov, S., Eds, 239-262 (2016).
42. J. W. Fergus, *Journal of the European Ceramic Society* **32** (3), 525-540 (2012).

43. H. Ohta, *Materials today* **10** (10), 44-49 (2007).
44. C. Li, Q. Chen and Y. Yan, *Materials* **11** (10), 1807 (2018).
45. T. Tsubota, M. Ohtaki, K. Eguchi and H. Arai, *Journal of Materials Chemistry* **7** (1), 85-90 (1997).
46. D. T. Morelli and G. A. Slack, *High thermal conductivity materials*, 37-68 (2006).
47. N. Ma, J.-F. Li, B. Zhang, Y. Lin, L. Ren and G. Chen, *Journal of Physics and Chemistry of Solids* **71** (9), 1344-1349 (2010).
48. W. Guan, L. Zhang, C. Wang and Y. Wang, *Materials Science in Semiconductor Processing* **66**, 247-252 (2017).
49. Y. Tian, M. R. Sakr, J. M. Kinder, D. Liang, M. J. MacDonald, R. L. Qiu, H.-J. Gao and X. P. Gao, *Nano letters* **12** (12), 6492-6497 (2012).

Chapter 2

Material Preparation and Characterization Techniques

This chapter briefly describes the experimental method used to synthesize the dual doped ZnO materials and various characterization techniques adopted to study the structural, morphological, optical, and physical properties including thermoelectric properties of the synthesized materials.

2.1 Introduction

This chapter discusses the experimental procedure used for the material preparation and the characterization techniques used to analyze various characteristics of the synthesized materials. The synthesis of the dual doped ZnO materials was done through the solid-state reaction method. The characterization discussion includes X-ray diffraction, FESEM analysis, EDAX, UV-Vis spectroscopic analysis, Hall measurement analysis, and thermoelectric studies such as electrical conductivity, Seebeck coefficient, and thermal conductivity measurements.

2.2 Solid-state reaction technique

Various methods are used for the synthesis of bulk materials such as the solid-state reaction, sol-gel, chemical, and co-precipitation¹⁻⁶. Among these, solid state reaction is capable of large-scale production of polycrystalline materials. At low temperatures, the solid-state reaction occurs at a slow rate, and high temperatures are necessary for an efficient solid-state reaction. In this reaction, both the reagents and products are in solid form. Chemical and morphological properties such as reactivity of reagents, surface area, free energy change, and other conditions such as temperature, pressure, and reaction environment will affect solid state reactions⁷. Various steps involved in the preparation of samples used for the investigations are discussed briefly.

2.2.1 Mixing & grinding

The solid-state reaction starts with the homogenous mixing of the powders; pure oxide powders (99.99% purity) were mixed according to the required stoichiometric ratio. The powders with extra pure acetone are well ground in an agate mortar and the grinding of the mixtures was done for several hours to make them homogenous. Grinding of the powders will cause a reduction in particle size and porosity, and it also introduces defects and dislocations which will accelerate the diffusion of dopants and solid solution formation.

2.2.2 Calcination

It is a process of heating solids at high temperatures to remove the volatile impurities in the solid materials. Removing the volatile impurities reduces the internal shrinkage that will occur in the latter processing such as warping, internal stresses, etc ⁸. During calcination, decomposition of the oxides occurs and then initiation of nucleation for the grain growth. The heating of the mixtures occurs at an intermediate temperature less than the sintering temperature. Here, the fine ground powders were calcinated at 450°C for 4 hours.

2.2.3 Pelletization

To sinter the powders, it is essential to bring the powders into a definite shape with high density. Pelletization is essential for effective sintering and pellets of desired shapes are used for the characterizations and it increases the surface area of contact with heat. Calcinated powders were filled in a die of the required shape and made into pellets using a hydraulic pelletizer.

2.2.4. Sintering

The densified pellets were sintered at high temperatures below the melting point of the materials for several hours and the sintered materials were cooled at a particular rate. Sintering improves mechanical strength and density and eliminates pores. During sintering, solid state interdiffusion of different compounds occurs due to the variation in chemical potential arising from the difference in concentration ⁹. The dual doped samples of ZnO were sintered at 1300°C for 4 hours at a heating/cooling rate of 5°C in a programmable high temperature furnace shown in Fig 2.1. The steps involved in solid state reaction method are depicted in Fig 2.2



Fig 2.1 Therelek electrically heated high temperature furnace

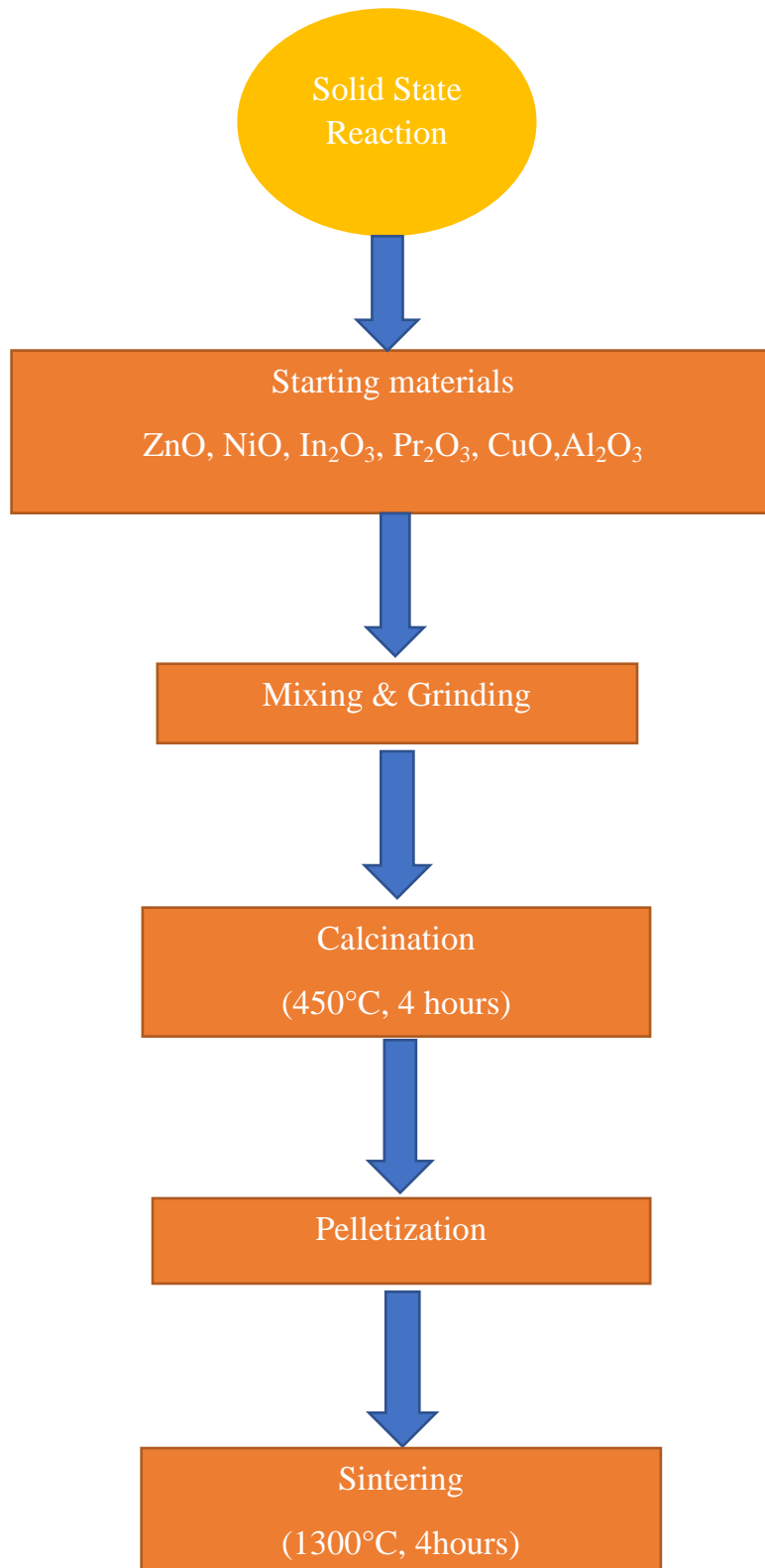


Fig 2.2 Procedure for solid-state reaction of dual doped ZnO materials

2.3 Characterization techniques

The as-sintered materials in the powder form and pellet forms were used for various characterizations and the characterization techniques used are discussed briefly.

2.3.1 Powder X-ray diffraction

The X-ray diffraction technique is a non-destructive analytical method for the structural characterization of materials in bulk, nano, and thin film forms. This technique is used to determine the crystal size, phase identification, crystal structure, residual stress and strain lattice parameters, dislocation density, crystallographic orientation, thermal expansion coefficient, etc ¹⁰. The powder X-ray diffraction method is suitable for the structural studies and phase identification of polycrystalline materials and it gives data about the atomic arrangement in the crystals. The underlying principle of X-ray diffraction is Bragg's law, according to which a crystal consists of layers or planes with indices (h, k, l) and distance d, the X-rays are reflected from the plane at an angle θ when impinging on the plane of atoms. The intensity of the reflected beam will be maximum when the path difference between the two reflected waves from two different planes is an integral multiple of the wavelength of the X-ray, λ ¹¹. Bragg's law is given by,

$$2d \sin\theta = n\lambda \quad (2.1)$$

Here n is the order of diffraction. Bragg's equation gives the condition for constructive interference. Fig 2.3 is the illustration of X-ray diffraction in materials. The X-rays are generated from the filament of a cathode ray tube. The accelerated electrons from the highly heated filament will interact with the target materials such as Cu, Fe, Mo, and Cr, and the interaction will knock out electrons from the inner shell of the atoms which give rise to X-rays, and the wavelength of X-rays are characteristics of the target material. This X-rays will direct into the specimen which is rotated in the path of the collimated X-ray beam at an angle θ and the resulting XRD patterns are recorded.

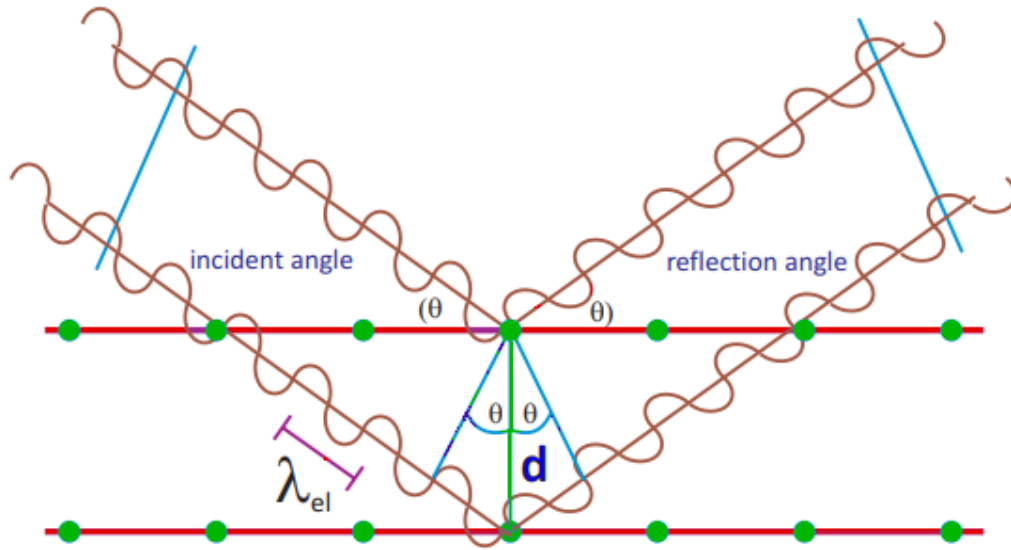


Fig 2.3 Illustration of X-ray diffraction

The crystallite size can be estimated from the Scherrer formula,

$$D = \frac{K\lambda}{\beta \cos\theta} \quad (2.2)$$

Where D is the crystallite size, K is the shape factor, β is the full width at half maximum, θ is the angle of diffraction, and λ is the wavelength of X-ray. A decrease in crystallite size is identified from the increase in peak width which indicates that there are not enough planes in the small crystallite to produce destructive interference. A narrow XRD peak indicates the increase in crystallite size of the material under investigation, in which complete destructive interference will occur below and above the Bragg angle. The photon scattered from the top (h,k,l) plane will be out of phase with the photon scattered from the deep plane within the crystallite¹².

The crystallite size is also determined using the Williamson-Hall (W-H) plot, using the W-H equation,

$$\beta \cos\theta = \frac{K\lambda}{D} + 4\epsilon \sin\theta \quad (2.3)$$

The intercept and slope of the graph plotted between $\beta \cos\theta$ and $4\sin\theta$ give the induced residual strain and crystallite size of the materials under investigation. Using the strain, the stress developed in the material also can be calculated.

Each material has specific XRD patterns with a particular relative intensity and interplanar spacing. So, analysing the peak positions and peak intensities, the corresponding interplanar spacing can be determined using the formulae,

$$\text{Cubic system, } \frac{1}{d^2} = \frac{h^2+k^2+l^2}{a^2} \quad \text{where, } a=b=c, \alpha=\beta=\gamma=90^\circ \quad (2.4)$$

$$\text{Tetragonal system, } \frac{1}{d^2} = \frac{h^2+k^2}{a^2} + \frac{l^2}{c^2} \quad \text{where } a=b \neq c, \alpha=\beta=\gamma=90^\circ \quad (2.5)$$

$$\text{Hexagonal system. } \frac{1}{d^2} = \frac{4}{3} \left(\frac{h^2+hk+k^2}{a^2} \right) + \frac{l^2}{c^2} \quad \text{where } a=b \neq c, \alpha=\beta=90^\circ, \gamma=120^\circ \quad (2.6)$$

$$\text{Orthorhombic system } \frac{1}{d^2} = \frac{h^2}{a^2} + \frac{k^2}{b^2} + \frac{l^2}{c^2} \quad \text{where } a \neq b \neq c, \alpha=\beta=\gamma=90^\circ \quad (2.7)$$

$$\text{Rhombohedral system } \frac{1}{d^2} = \frac{h^2+k^2+l^2 \sin^2\alpha + 2(hk+kl+hl) (\cos^2\alpha - \cos\alpha)}{a^2(1-3\cos^2\alpha+2\cos^3\alpha)}$$

$$\text{where, } a=b=c, \alpha=\beta=\gamma \neq 90^\circ \quad (2.8)$$

$$\text{Monoclinic system } \frac{1}{d^2} = \frac{1}{\sin^2\beta} \left(\frac{h^2}{a^2} + \frac{k^2 \sin^2\beta}{b^2} + \frac{l^2}{c^2} - \frac{2hl \cos\beta}{ac} \right)$$

$$\text{where } a \neq b \neq c, \alpha=\gamma=90^\circ \neq \beta \quad (2.9)$$

$$\text{Triclinic system } \frac{1}{d^2} = \frac{1}{V^2} (S_{11}h^2 + S_{22}k^2 + S_{33}l^2 + 2S_{12}hk + 2S_{23}kl + 2S_{13}hl),$$

$$\text{Where } a \neq b \neq c, \alpha \neq \beta \neq \gamma \quad (2.10)$$

The d values obtained from the above equations are used to calculate the lattice constants of the materials. The unknown material can be identified from the XRD pattern by comparing the peak positions and interplanar spacing with the recorded value in a data base system such as JCPDS, ICDD or ICSD.

We have used the Rigaku-Miniflex X-ray diffractometer shown in Fig 2.4 , with X-ray wavelength ($\text{CuK}\alpha$) $\lambda = 1.542 \text{ \AA}$, to investigate the structure of dual-

doped materials within the 2theta range 20° - 80° . The analysis of the obtained XRD pattern was done with the PDXL software. The experimental XRD pattern was compared with the standard ICDD (International Centre for Diffraction Data) database.



Fig 2.4 Rigaku Miniflex X-ray diffractometer

2.3.2 Field emission scanning electron microscopy (FESEM)

Scanning electron microscopic analysis provides information about the topography, morphology, phase distribution, presence and location of defects, and composition differences. It uses electrons to scan the surface of a specimen and produce highly magnified images with high resolution. Electrons, from an electron gun, emitted thermionically or emitted through field emission will move toward the anode between the electromagnetic fields and lenses, and the electron beam is focused on the sample. This low-energy electron will scan over the sample as an electron probe and this will simulate the emission of high-energy backscattered electrons (BSE) and

low-energy secondary electrons (SE) from the specimen. The electron impinging on the sample interacts with the atoms of the sample in different ways. In inelastic interaction, energy is transferred from the electron beam to the sample, while in elastic interaction the trajectory of the electron beam changes without losing energy. Secondary electrons (energy of 2eV-5eV) are ejected from the outer shell of the specimen as a result of the inelastic interaction. Backscattered electrons are the electrons from the incident probe resulting from the elastic interaction with the specimen, which changes the trajectory and escapes the sample¹³. The backscattered and secondary electrons will produce signals that contain information about the surface morphology of the specimen.

A SEM system consists of

1. An electron gun to generate electrons of high energy
2. A column for traveling the electrons through two or more magnetic lens
3. Deflection system of scanning coils
4. Electron detectors to detect BSE and SE
5. Specimen chamber
6. A computer or TV to view the image in high resolution

The electron gun emits and accelerate the electron and a series of lenses are used to demagnifies and focus the beam into the sample. Scanning implies the positioning of the electron probe into the specimen and the positioning of the beam, which carries signal intensity information, to the viewing device such as a camera or monitor. Three types of electron guns – tungsten, lanthanum hexaboride thermionic electron gun and the field emission gun are used. Tungsten and lanthanum hexaboride are usually used as filaments in thermionic electron guns. A high vacuum is required for the operation of a field emission gun, so it is very expensive but gives more brightness with high resolution. Scanning, positioning, and focusing of the electron beam are done with the electromagnetic or electrostatic fields provided by the magnetic lenses. Scanning coils control the electron beam position on the sample.

Besides, some other functions of scanning coils are scanning the beam to produce images, determining the image magnification, and electronic shifting of the imaged area, etc. Different detectors are used to detect the backscattered electrons and secondary electrons. BSE detectors are solid-state and scintillation detectors and they cannot detect the low energy electrons. The Everhart-Thornley (ET) detector detects the secondary electron and produces images with high-resolution. The schematic representation of SEM is depicted in Fig 2.5

In this work, the surface morphological analysis was done with Carl Zeiss Sigma model Field Emission Scanning Electron Microscopy (FESEM) equipped with an energy dispersive X-ray (EDAX) analysis facility which is shown in Fig 2.6

2.3.3 Energy dispersive X-ray spectroscopy (EDAX/EDS)

EDAX is inbuilt with the SEM apparatus; it is used to identify the elemental composition of materials. The basic principle in EDAX is that characteristic X-rays are produced when high-energy electrons impinge on a material. The energy of the generated X-rays depends on according to the nature and characteristics of the element present in a sample. So, this method accurately detects the elements and concentration of the elements present in the sample. When the material is irradiated, an electron will excite from the innermost shell of its parent atom, then a high-energy electron from the outer shell occupied the vacancy. The energy difference between the two shells is emitted as an X-ray and the X-rays produced in this way is called characteristic X-ray because the energy or wavelength of these X-rays is indicative of the element from which it was emitted. Thus, when electrons from the K, L, and M shells are excited, and these shells emit X-rays, then the corresponding X-rays as termed as K Lines, L Lines, and M Lines respectively. The four components of EDAX are an electron beam source, X-ray detector, pulse processor to measure the voltage with respect to X-rays, and a computer system or analyser¹⁴.

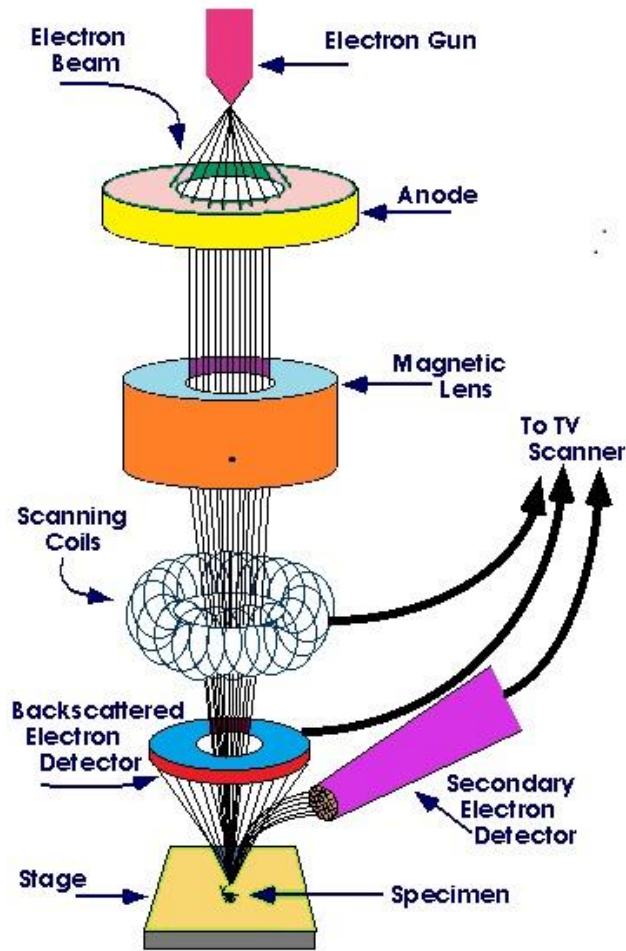


Fig 2.5 Illustration of SEM



Fig 2.6 Carl Zeiss Sigma model FESEM with EDAX facility

2.3.4 UV-Vis spectroscopic analysis

UV-Vis spectroscopy measures the discrete wavelengths of UV or visible light when it is transmitted through or reflected by a material. It is used to measure the electronic properties of materials. The spectral range of UV-Vis spectrometer is 190 nm to 900 nm and high end commercial spectrophotometers extend the spectral range into the NIR region of 3300 nm which measures the NIR properties of the material under investigation.

When light interacts with a matter it will transmit through, reflect or absorbed by the matter. During the light - matter interaction, electrons from the ground state excited into the higher energy state and the electronic transition takes place in two ways- direct and indirect. Direct transition is photon assisted while in indirect transition both phonon and photon involve. Information related to absorption, reflection and transmission such as refractive index, optical band gap energy, reflectance, absorbance, transmittance is obtained from UV-Vis spectroscopy. The reflectance R can be estimated from the equation in terms of the Kubelka-Munk function, F(R), absorption (K) and scattering coefficient (S) expressed as,

$$\frac{K}{S} = \frac{(1-R)^2}{2R} = F(R) \quad (2.11)$$

In our work, the optical band gap energy of materials is determined from the Tauc relation, connecting the photon energy ($h\nu$) and absorption coefficient (α) and is given by,

$$(\alpha h\nu)^n = A(h\nu - E_g) \quad (2.12)$$

Here, E_g , A, and n represents the optical band gap energy, a constant and nature of electronic transition respectively. For direct allowed transition $n = \frac{1}{2}$, for direct forbidden transition $n = \frac{3}{2}$, for indirect allowed transition $n = 2$, for indirect forbidden transition $n = 3$ ¹⁵.

The optical band gap of the materials can be estimated by extending straight line portion of the graph plotted between $(h\nu)$ versus $(\alpha h\nu)^2$ to the energy axis $(h\nu)$ ¹⁶.

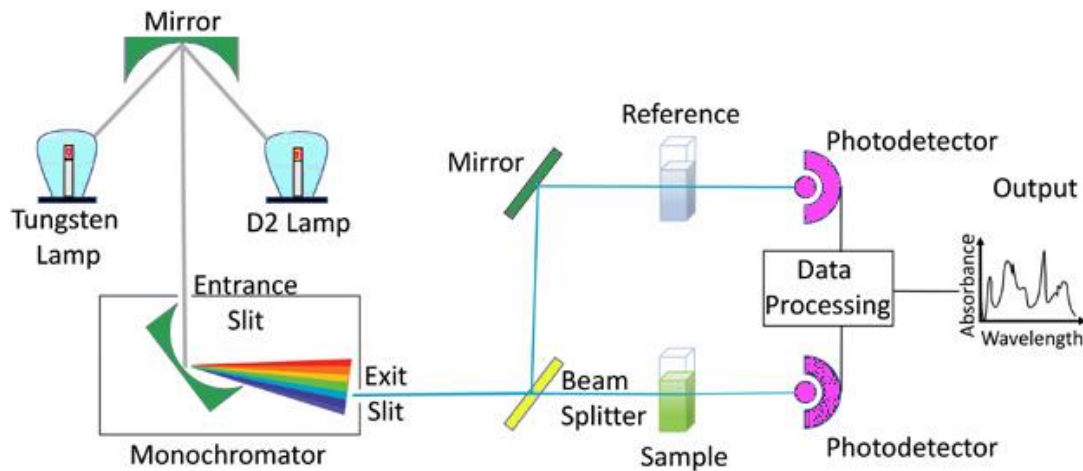


Fig 2.7 Schematic representation of UV-Vis spectrophotometer

The schematic representation of the UV-Vis spectrophotometer is shown in Fig 2.7. The tungsten lamp produces visible light and the D2 lamp emits ultra violet radiation. The generated waves are directed to the monochromator which chooses wavelengths and it is separated into two beams of equal intensity by a beam splitter. One beam is allowed to incident on the sample and the other beam into the reference sample kept in a cuvette. The detector records the light from the samples¹⁷. The ratio of the two intensities is measured as the percentage of transmittance. In the reflectance mode, the percentage of reflectance is the ratio of reflectance from the sample to the reflectance from the reference sample.

2.3.5 Hall measurement

The Hall measurement analysis is essential to determine the electronic transport parameters of a material. In this investigation, the carrier density of doped materials is determined from the Hall measurements. The basics of Hall measuring system is the Hall effect discovered by E.H. Hall in 1879. When a current carrying solid conductor is placed in a magnetic field perpendicular to the direction of current, a transverse electric field and hence a voltage is developed. The transverse voltage produced is the Hall voltage (V_H) and it is proportional to the current (I) and the applied magnetic field (B). The illustration of Hall effect is shown in Fig 2.8.

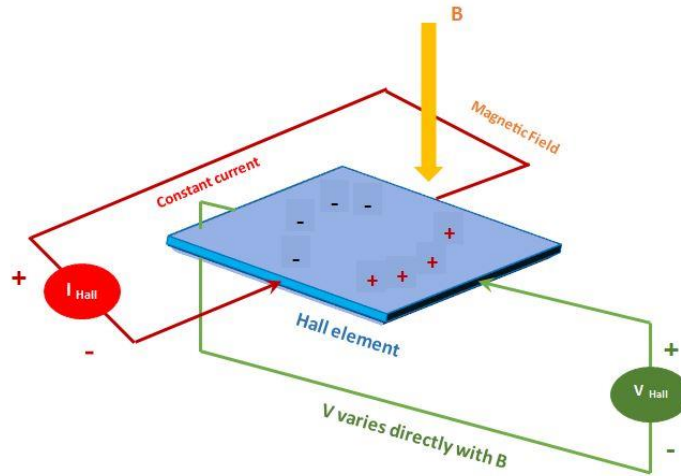


Fig 2.8 Illustration of Hall effect

The sample in square shape with 1x1cm dimension and a permanent magnet of magnetic field of intensity 0.5 T are used for the measurements. Current is provided from a constant current source in accordance with the resistance of the sample used.

The Hall coefficient is determined from the formula,
$$R_H = \frac{V_H t}{IB} \quad (2.13)$$

Where t is the thickness of the sample

The carrier concentration is given by
$$n = \frac{1}{(e R_H)} \quad (2.14)$$

Also, the mobility (μ) of the charge carriers can be calculated using the equation connecting electrical conductivity (σ), and carrier concentration (n),

$$\sigma = ne\mu \quad (2.15)$$

ie .,
$$\mu = \frac{\sigma}{ne} \quad (2.16)$$

2.3.6 Thermoelectric measurements

The thermoelectric parameters - Seebeck coefficient and electrical conductivity of the material are measured by the thermoelectric measurement system -ULVAC ZEM-3(M8) shown in Fig 2.9. Simultaneous measurement of electrical resistivity and Seebeck coefficient are possible in this system. The electrical resistivity is

measured from the four-probe method. This instrument uses ADCMT-6146 DC current source to provide current and KEITHLEY-2010 multimeter to measure the voltage. The sample is kept vertically between the upper and lower blocks of an infrared furnace as shown in Fig 2.10. Before the measurements, the system is evacuated and the measurements were done from room temperature to 700° C in a helium atmosphere to avoid oxidation of the sample.

By applying current between the two ends of the cylindrical or rectangular sample through the lower and upper electrodes, and measuring the voltage at the other two ends, the resistance of the sample can be estimated. The resistivity can be determined from the resistance and the dimensions of the sample. In general, the resistance (R) and resistivity (ρ) are related as,

$$R = \frac{\rho l}{A} \quad (2.17)$$

Here, the length of the material is measured as l - the distance between the probes, and the area A measured from the width (W) and thickness (D) of the material. The measurement system automatically chose the best value of current to measure the resistivity of the sample.

The Seebeck coefficient is measured from the voltage difference developed in the sample by creating a temperature difference between the two ends of the sample. Temperature differences of 10°, 20° and 30° are maintained in the sample. The heater in the lower block creates a temperature difference and the thermocouples measure the potential difference (ΔV) developed and the temperatures T_1 , T_2 of the two ends of the sample. From the temperature difference and the voltage difference, the Seebeck coefficient ($S = \Delta V / \Delta T$) of the material can be determined. In addition, the error calculations of the measurements were done by the system internally.



Fig 2.9 ULVAC ZEM-3 (M8) measurement system

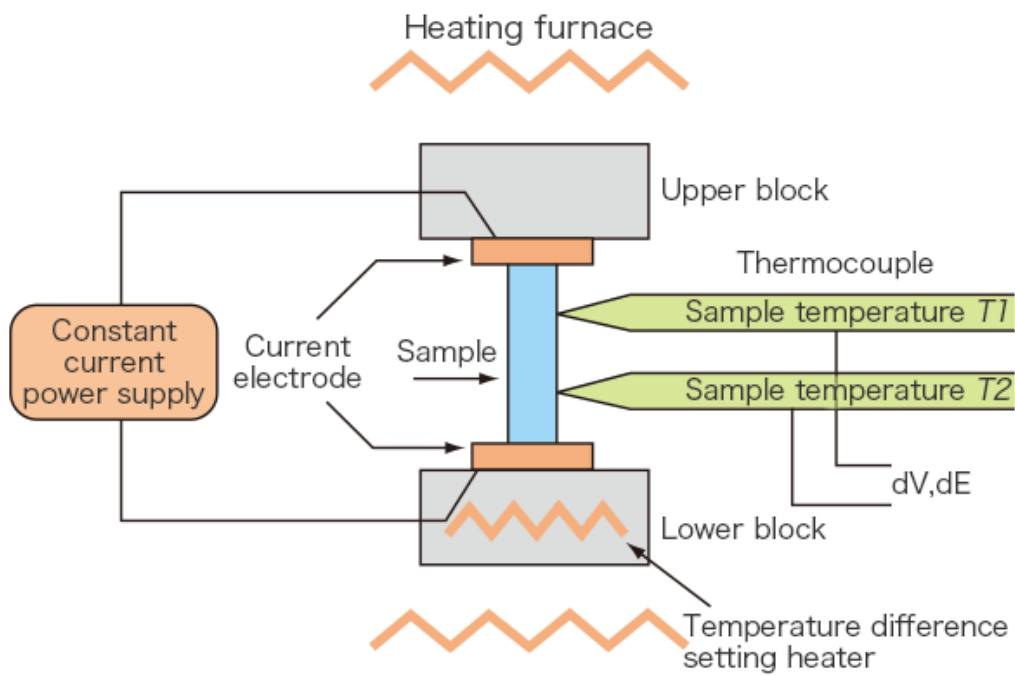


Fig 2.10 Schematic representation of ULVAC-ZEM-3

2.3.7 Thermal conductivity measurements

The thermal conductivity (κ) of a material measures the ability to conduct heat and it is defined as the heat flux per unit area and temperature gradient. Heat always flows from higher temperature to low temperature ¹⁸.

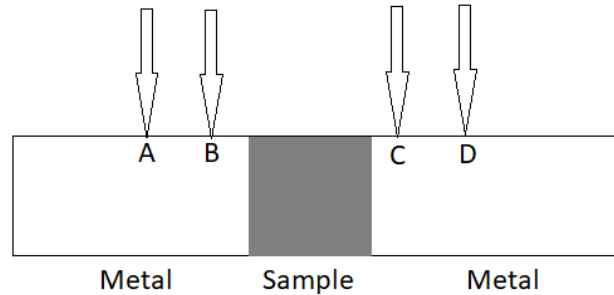


Fig 2.11 Schematic representation of divider bar method

In this work, divided bar method is used for the measurement of thermal conductivity and the schematic representation of the method is given in Fig 2.11. In this method, the sample is kept in between two metal blocks. The cross section of the sample is in the same shape and area as that of the metal blocks. This arrangement is kept in a chamber to minimize the heat loss as shown in Fig 2.12. Heat is allowed to pass through the first metal block, then through the sample and finally heat reaches to the second metal block. When the steady state is achieved, the thermal gradient $(dT/dx)_m$ between the metal blocks can be determined from the temperatures at positions A, B, C, and D. The thermal gradient in the sample $(dT/dx)_s$ can be calculated by the extrapolation of line AB and CD to the metal-sample interface as depicted in Fig 2.13.

The thermal conductivities of metal (k_m) and samples (k_s) are related by the equation,

$$k_m A \left[\frac{dT}{dx} \right]_m = k_s A \left[\frac{dT}{dx} \right]_s \quad (2.18)$$

Then, thermal conductivity of the sample is given by,

$$k_s = \frac{k_m \left[\frac{dT}{dx} \right]_m}{\left[\frac{dT}{dx} \right]_s} \quad (2.19)$$



Fig 2.12 Thermal conductivity measurement set up

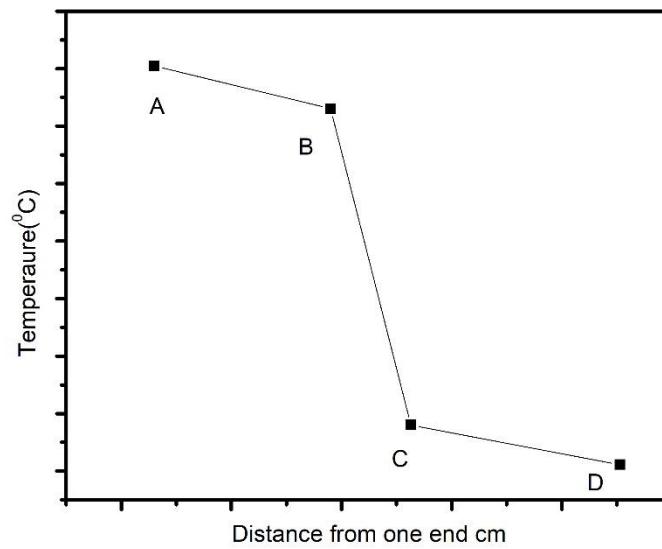


Fig 2.13 Temperature versus distance from one end of the block

References

1. P. Schiffer, A. Ramirez, W. Bao and S.-W. Cheong, *Physical Review Letters* **75** (18), 3336 (1995).
2. M. Saleemi, M. S. Toprak, S. Li, M. Johnsson and M. Muhammed, *Journal of Materials Chemistry* **22** (2), 725-730 (2012).
3. Z. Zhang, M. Sun, J. Liu, L. Cao, M. Su, Q. Liao, Y. Deng and L. Qin, *Scientific Reports* **12** (1), 10045 (2022).
4. L. Xue, Z. Zhang, W. Shen, H. Ma, Y. Zhang, C. Fang and X. Jia, *Journal of Materiomics* **5** (1), 103-110 (2019).
5. A. Kołodziejczak-Radzimska and T. Jesionowski, *Materials* **7** (4), 2833-2881 (2014).
6. M. J. Haque, M. M. Bellah, M. R. Hassan and S. Rahman, *Nano Express* **1** (1), 010007 (2020).
7. S.-J. Cho, M.-J. Uddin and P. Alaboina, in *Emerging nanotechnologies in rechargeable energy storage systems* (Elsevier, 2017), pp. 83-129.
8. B. Rand, in *Concise Encyclopedia of Advanced Ceramic Materials* (Elsevier, 1991), pp. 49-51.
9. F. Lemoisson and L. Froyen, (2005).
10. E. Ameh, *The international journal of advanced manufacturing technology* **105**, 3289-3302 (2019).
11. D. D. Le Pevelen, (2010).
12. S. Misture and R. Snyder, *Encyclopedia of materials: science and technology*, 9799-9808 (2011).
13. E. N. Kaufmann, *Characterization of Materials, 2 Volume Set.* (2003).
14. N. Raval, R. Maheshwari, D. Kalyane, S. R. Youngren-Ortiz, M. B. Chougule and R. K. Tekade, in *Basic fundamentals of drug delivery* (Elsevier, 2019), pp. 369-400.
15. S. Sarkar, S. Garain, D. Mandal and K. Chattopadhyay, *RSC Advances* **4** (89), 48220-48227 (2014).
16. P. Jubu, F. Yam, V. Igba and K. Beh, *Journal of Solid State Chemistry* **290**, 121576 (2020).
17. F. S. Rocha, A. J. Gomes, C. N. Lunardi, S. Kaliaguine and G. S. Patience, *The Canadian Journal of Chemical Engineering* **96** (12), 2512-2517 (2018).
18. J. Mulopo and J. Abdulsalam, in *Graphene-Based Nanotechnologies for Energy and Environmental Applications* (Elsevier, 2019), pp. 155-179.

Chapter 3

Preparation, characterization, and thermoelectric performance of Ni-In dual doped zinc oxide

This chapter deals with the investigation of the effect of structural and morphological deformation on the enhancement of the thermoelectric efficiency of ZnO through nickel and indium dual doping. Dual cation doping improves the figure of merit by enhancing electrical transport properties with significantly reducing thermal conductivity.

3.1 Introduction

Thermoelectric materials have drawn significant attention as it is one of the most eco-friendly waste heat energy-recovering techniques and can be used to make precise power generator and cooling systems without any moving parts. Effective thermoelectric conversion necessitates materials with high efficiency and the ideal characteristics of a thermoelectric material are high power factor ($S^2\sigma$) and thermal resistance. It is challenging to achieve high electrical transport properties and low thermal conduction in a material and it is demonstrated that the presence of impurity atoms and the nanostructuring of the material greatly lessen the challenges associated with locating materials with high electrical conductivity, low thermal conductivity, and high Seebeck coefficient^{1, 2}.

Doping will enhance the thermoelectric characteristics of ZnO and studies show that multiple doped materials have higher thermoelectric performance than singly doped materials³⁻⁷. The single doped and codoped ZnO with group 13 elements enhances the thermoelectric properties⁸. The dual doping of Al and Ga increases the figure of merit of ZnO to 0.65 at 1247 K⁹. Simultaneous substitution of multiple dopants such as Ni, S, C and Fe resulted in a 2.4 times increase in the figure of merit with a 60 % increase in power factor¹⁰. M.Ullah et al. reported a 1.4 times increment in the power factor of Al and Ga dual doped ZnO ceramics¹¹.

This work investigates the enhancement of thermoelectric properties of ZnO up on dual doping of nickel and indium. Ni is one of the transition metals very well substituted into the ZnO structure due to their similar valance and ionic radii. In³⁺ ions with large ionic radii will increase the charge carrier density and lattice distortions in the lattice. Colder et al. reported that nickel doping increases the power factor to $0.56 \text{ mWm}^{-1} \text{ K}^{-2}$ than the pure ZnO¹². Trivalent impurity addition is beneficial for the enhancement of electrical conductivity as the impurity ions such as In³⁺ provide more electrons and thereby increase the carrier density of the host material. The electrical resistivity of In doped ZnO decreased to $1.88 \text{ m}\Omega\text{cm}$ and a power factor increased to $4.66 \times 10^{-4} \text{ Wm}^{-1} \text{ K}^{-2}$ ¹³. So, dual doping of Ni and In into

the ZnO lattice will enhance the thermoelectric properties more than single doping with indium and nickel.

3.2 Experimental method

Nickel and indium doped zinc oxide ($(\text{Zn}_{1-x-y}\text{Ni}_x\text{In}_y)\text{O}$, $x=0.01$, $y=0.0025$, 0.005 , 0.01 , 0.02 , 0.03) materials were prepared via solid-state reaction method. Zinc oxide, nickel oxide and indium oxide powders (purity 99.9%) were weighed according to the stoichiometric ratio and well-ground for 1 hour. Fine ground powder mixtures were calcinated for 4 hours at 450°C and the calcinated powders were pelletized using a hydraulic pelletizer of 10 Ton force. The densified pellets were kept for sintering at 1300°C for 4 hours and characterisation studies such as structural, morphological, optical and thermoelectric analysis were carried out with the sintered materials. Detailed description regarding the synthesis and characterisations conducted are given in Chapter 2. The prepared dual doped samples are termed as $\text{N}_1\text{I}_{0.25}$ (Ni=1%, In= 0.25%), $\text{N}_1\text{I}_{0.5}$ (Ni=1%, In= 0.5%), N_1I_1 (Ni =1%, In=1%), N_1I_2 (Ni=1% In=2%) and N_1I_3 (Ni=1% In=3%).

3.3 Results and discussions

3.3.1 Structural characterisations

The powder XRD patterns of the $\text{Zn}_{(1-(x-y))}\text{Ni}_x\text{In}_y\text{O}$ samples are shown in Fig 3.1. All the characteristic peaks were compared and indexed with the ICDD card no. 00-005-0664. All the peaks were resembling pure ZnO peaks, and no impurity secondary phases of nickel and indium were observed up to the solubility of N_1I_2 , indicating that Ni and In dopants were well incorporated into the ZnO lattice. An unknown peak with very small relative intensity is observed in the pattern of the In 3% doped sample, which may be attributed to the presence of multiphase growth of Ni and In in the ZnO lattice for higher doping concentrations. The doped and pristine materials were belonging to the space group P63mc. The strain produced in the lattice and the shift in peaks to higher and lower angles substantiate the substitution of dopants as presented in Fig 3.2. The lower angle peak shift is due to the decrease in strain produced due to the inclusion of cations with large ionic radii

into the ZnO lattice, which causes lattice expansion^{4, 14}. The higher angle peak shift observed in the XRD pattern of N₁I₁ is due to the increased strain in the lattice. The increase in In³⁺ ion substitution in the host lattice may be the reason for the lower angle peak shift observed in the samples with N₁I₂ and N₁I₃ even if the strain produced is larger compared to all other samples.

The average crystallite size was calculated using Scherrer's formula,

$$D = \frac{K\lambda}{\beta \cos\theta} \quad (3.1)$$

Where β is the FWHM, K is the shape factor and λ is the wavelength of CuK α radiation.

The strain-induced ε in the sintered samples were attributed to the distortions and lattice imperfections produced in the structure of host ZnO due to the incorporation of Ni²⁺ and In³⁺ ions with ionic radii of Ni²⁺=0.69 Å, In³⁺= 0.8 Å, Zn⁺=0.74 Å, can be calculated by the formula,

$$\varepsilon = \frac{\beta}{4 \tan\theta} \quad (3.2)$$

From equations (3.1) and (3.2), we get the W-H equation

$$\beta \cos\theta = \frac{K\lambda}{D} + 4\varepsilon \sin\theta \quad (3.3)$$

The slope of the graph plotted between $\beta \cos\theta$ and $4 \sin\theta$ gives the strain and the y-intercept gives the average crystallite size of the samples. The induced strain and average crystallite size measured are given in Table 3.1. The average crystallite size of the doped samples was found to decrease with the doping concentration, which is due to the increased distortion produced in the lattice resulting in reduction in the nucleation and subsequent growth of ZnO. The negative strain indicates the bond

length contraction and compression of the lattice, which leads to a reduction in cell volume¹⁵.

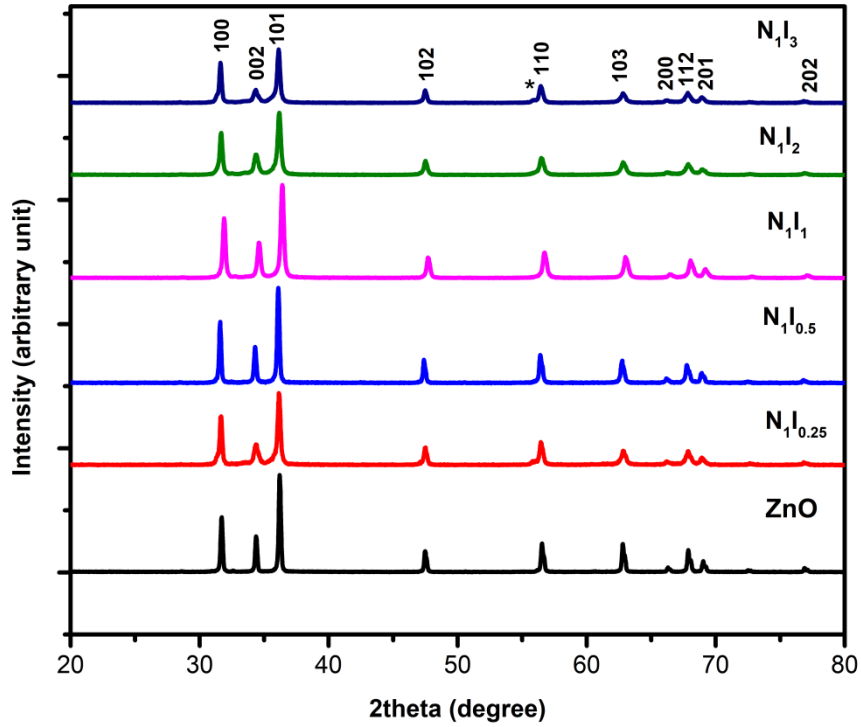


Fig 3.1 Powder XRD pattern of undoped and doped samples

Sample	Crystallite size D (nm)	Strain ϵ (10^{-4})
ZnO	56.25	-0.25
Ni ₁ I _{0.25}	36.6	-17.9
Ni ₁ I _{0.5}	53.68	1.27
Ni ₁ I ₁	47.16	4.11
Ni ₁ I ₂	40.07	8.45
Ni ₁ I ₃	23.86	-9.50

Table 3.1 Average crystallite size and the induced strain of the materials

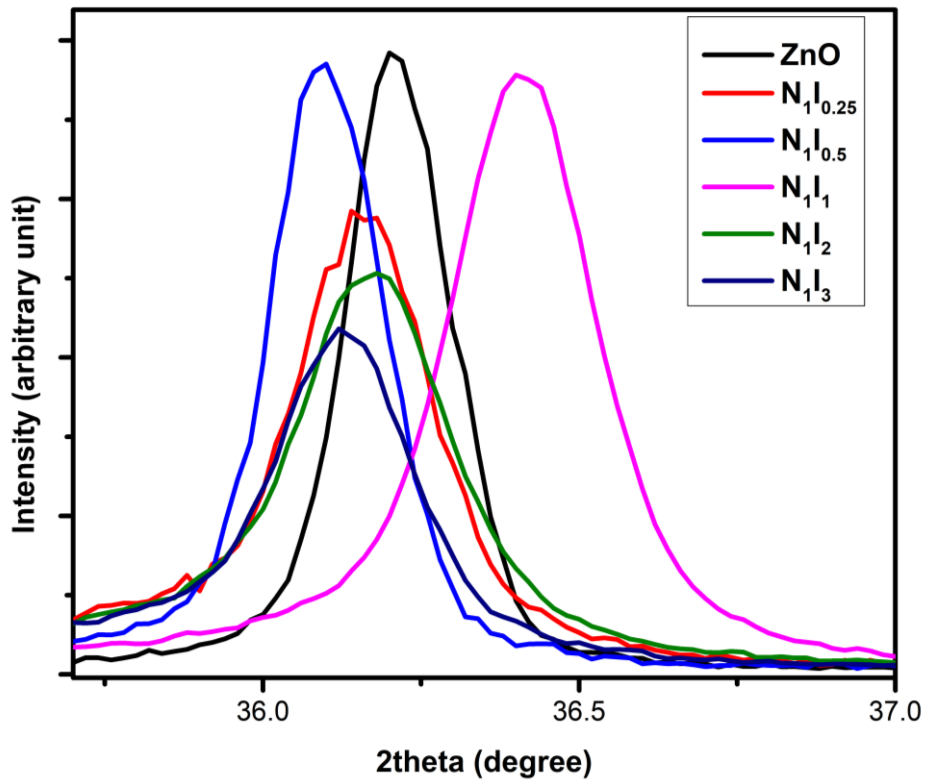
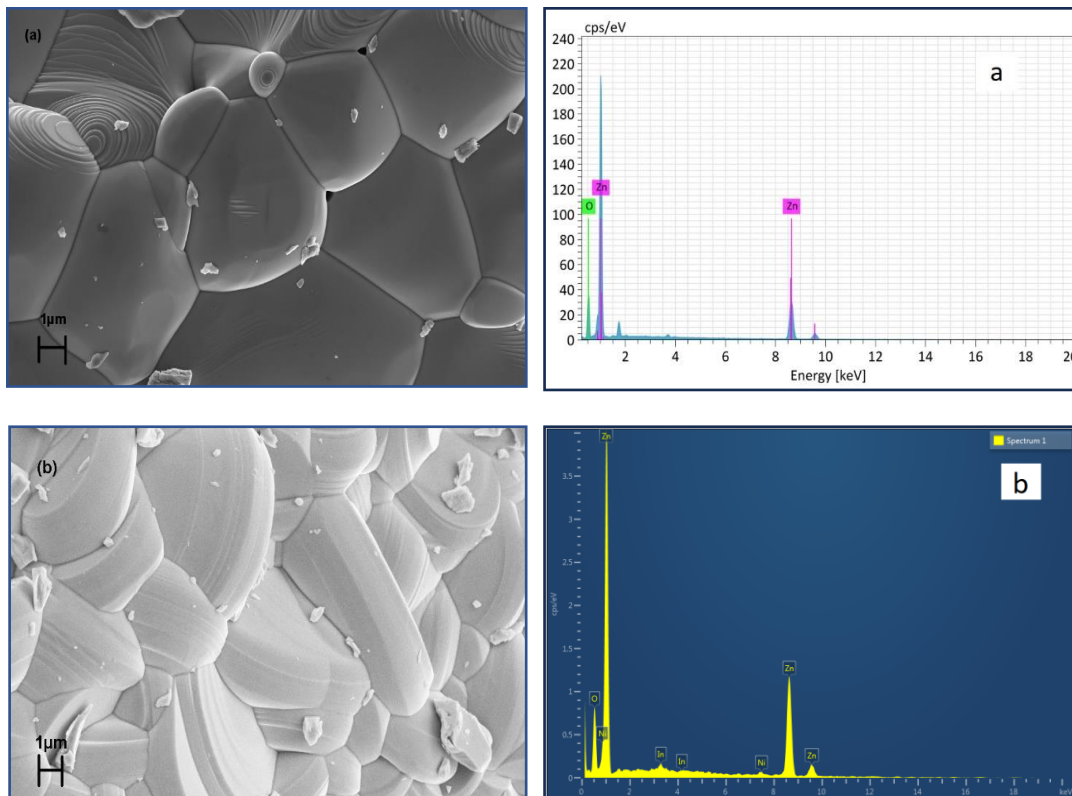


Fig 3.2 Powder XRD Peak shift of (101) plane



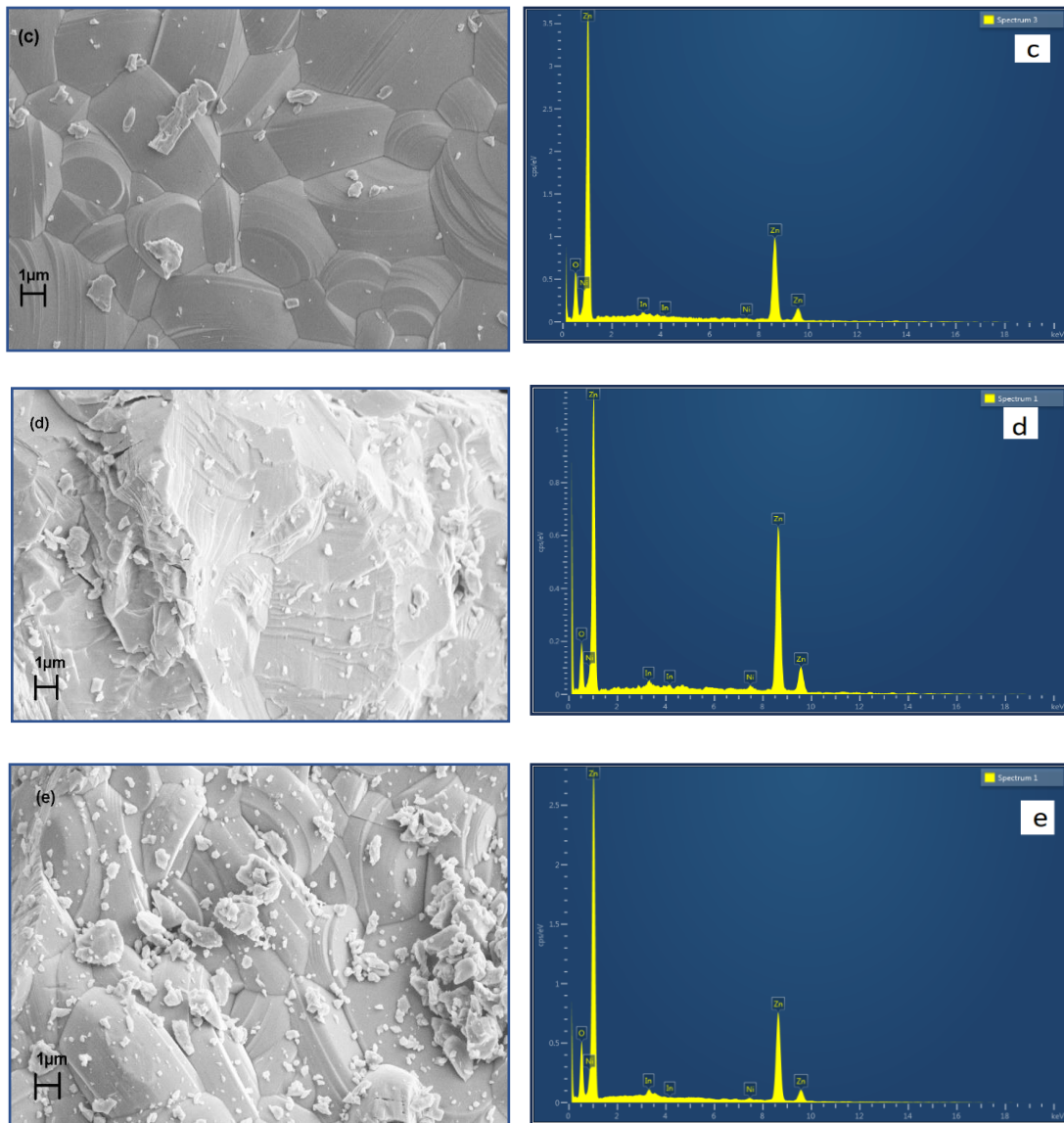


Fig 3.3 FESEM and EDAX images of (a) ZnO (b) $Ni_1I_{0.25}$ (c) $Ni_1I_{0.5}$ (d) Ni_1I_1 (e) Ni_1I_2

3.3.2 FESEM and EDAX analysis

FESEM and EDAX images of the as prepared samples are shown in the Fig 3.3. SEM image of pure ZnO were dense with grains of larger size. The substitution of Ni^{2+} and In^{3+} into the host lattice can be evident from the variations in the SEM micrographs of doped samples with smaller grains than the undoped sample. Larger concentration of the dopants introduces more grains with larger sizes than the samples doped with lower concentrations. These are the clear indication of Ni^{2+} and

In^{3+} doping increases grain boundary scattering which will reduce the thermal conductivity of the materials.

The elemental analysis of the materials was performed with the Energy Dispersive X-ray Analysis (EDAX) and agrees with the doping concentration chosen for the sample preparation. Zn, O, Ni, In peaks can be identified from the spectrum and no other impurity peaks were detected. The elemental mapping of sample N_1I_1 is shown in Fig 3.4.

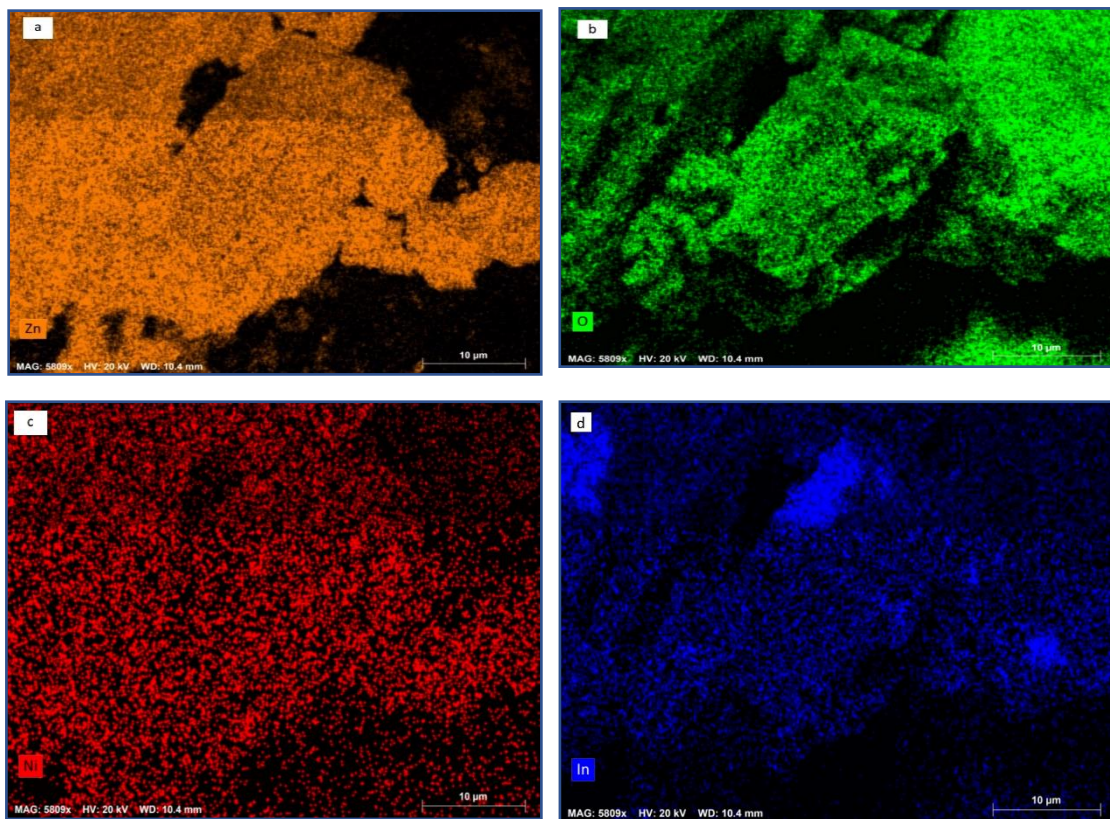


Fig 3.4 EDS mapping of N_1I_1 (a) Zinc (b) Oxygen (c) Nickel (d) Indium

3.3.3 UV-Vis spectroscopic analysis

The optical band gap energy of a material depends upon several factors like crystallite size, charge carrier concentration, stress and strain produced during impurity addition^{16, 17}. ZnO is a direct transition material, and the absorption coefficient can be expressed by the Tauc's relation¹⁸.

$$(\alpha h\nu)^2 = A(h\nu - E_g) \quad (3.4)$$

Where α is the absorption coefficient, h is Planck's constant, ν is the frequency of the incident photon, E_g is the optical bandgap energy, and A is the constant of direct transition. The band gap energy is determined by plotting $(\alpha h\nu)^2$ versus $h\nu$ and the linear extrapolation of the $(\alpha h\nu)^2$ plot to the energy axis gives the optical band gap energy of the undoped and doped samples.

The strong absorption in the ultraviolet region is attributed to the band edge absorption, caused due to the electron transfer from the valence band to the conduction band. There is no absorption in the visible region of the pure ZnO, but a red shift in the optical absorption edge occurred for the doped samples. A reduction in the optical band gap energy is observed in the dual doped samples due to the red shift in the absorption edge with increasing dopant concentration¹⁹. The band gap energy decreased from 3.1 eV to 2.2 eV while incorporating Ni and In into the ZnO lattice as shown in Fig 3.5. Similar results were reported for the ZnO doped with Li, In and Ni²⁰⁻²². Small amount of nickel will drastically reduce the optical band gap energy of pure ZnO, from 3.47 eV to 2.87 eV²². The same phenomenon occurs during the substitution of indium into the ZnO lattice, reduction from 3.233 eV to 3.095 eV²¹. The narrowing of optical band gap energy is due to the presence of Ni²⁺ and In³⁺ ions at the top of the valence band giving rise to the formation of new recombination centres with lower energy near the conduction band.

The size and band gap energy are interrelated; the N₁I_{0.5} sample has large size with lower band gap energy which is consistent with the size effect according to which, the band gap energy and size have an inverse relationship²³. The band gap energy of N₁I_{0.25}, which has small crystallite size, is very close to the band gap energy of the sample doped with Ni_{0.01} and In_{0.01} which may be due to the increased strain produced in the lattice during Ni_{0.01} and In_{0.0025} doping.

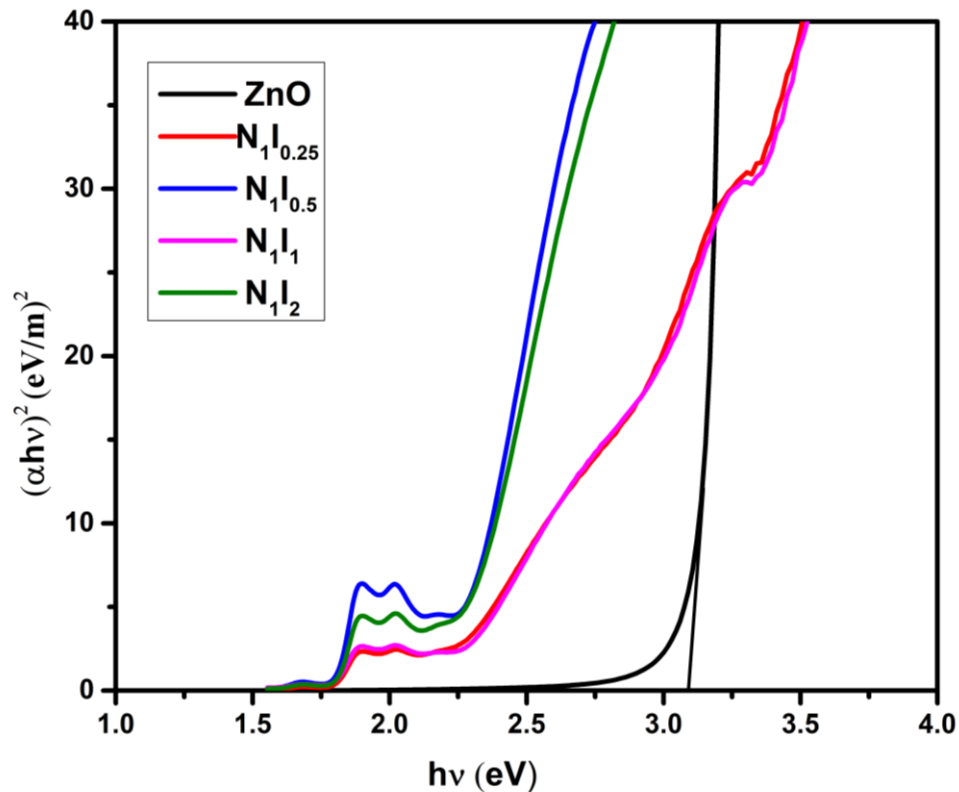


Fig 3.5 Tauc's plot of undoped and doped samples

3.3.4 Thermoelectric property studies

3.3.4.1 Electrical conductivity

The presence of small amount of defects, in the form of vacancies, interstitials or due to dopants may significantly change the electrical conductivity of ZnO. The electrical conductivity of the prepared samples was higher than the undoped ZnO as shown in Fig 3.6 (inset shows the electrical conductivity of $NiI_{0.25}$ and NiI_2 samples). The electrical conductivity of the doped samples shows metallic to semiconducting transition. The conductivity of the $NiI_{0.25}$ and $NiI_{0.5}$ increased to a value of 231.21 S/m at 873 K and 20300 S/m at 473 K and then decreases as shown in the inset. Among all the samples highest electrical conductivity was obtained for the sample NiI_1 , in which the conductivity reached a value of 50600 S/m at 473 K and then shows a decrease in the electrical conductivity, which means that the samples with indium content 0.0025, 0.005 and 0.01 show metallic behaviour¹³. The

same result was obtained when In and Ni codoped with Ga and Al respectively^{3, 5}. The conductivity of 398 S/m at 973 K was obtained for the N_1I_2 sample which shows a semiconducting nature as pure ZnO.

The electrical conductivity of a material is related to carrier concentration by the relation,

$$\sigma = ne\mu \quad (3.5)$$

where n is the carrier concentration, e is the electronic charge and μ is the mobility of charge carriers. The dual doping of Ni and In in the ZnO matrix increases the carrier concentration which increases the electrical conductivity of the samples. Hall measurement analysis shows that the carrier concentration of doped samples increases with doping concentration. The order of carrier concentration in the undoped ZnO is 10^{19} m^{-3} while doping with Ni and In it is increased into the order of 10^{21} m^{-3} . $6.20 \times 10^{19} \text{ m}^{-3}$, $1.43 \times 10^{21} \text{ m}^{-3}$, $2.64 \times 10^{21} \text{ m}^{-3}$, $3.58 \times 10^{21} \text{ m}^{-3}$, $5.34 \times 10^{21} \text{ m}^{-3}$ are the carrier concentrations of ZnO, and doped samples (Ni=1, In=0.25, 0.5, 1, 2) respectively. The increase in carrier concentration may due to the substitution of In^{3+} and Ni^{2+} ions into the ZnO lattice which contributes more charge carriers to the lattice⁵. It is expected that each In^{3+} ion substitution will contribute one electron to the host matrix. It is proved that the addition of trivalent elements increases the carrier concentration of the material^{8, 18}. The samples with low dopant concentration have low carrier density which leads to a reduction in the electrical conductivity. Increased addition of Ni^{2+} and In^{3+} ions induce defects scattering centres in the host lattice, which will cause trapping of free electrons donated by the dopants. Also, a fraction of the dopants remain unionised and will be clustered in the lattice. These clusters will act as carrier scattering centres which adversely affect the mobility of the charge carriers leading to the reduction of electrical conductivity of heavily doped samples such as N_1I_2 ^{3, 12}. As the temperature increases, the electrons in the Fermi level begin to move to the conduction band and the increased number of charge carriers may result in to decrease in carrier mobility. At high temperature, the collision between the charge carriers increases which adversely affect the mobility of charge carriers leading to a reduction in conductivity¹³.

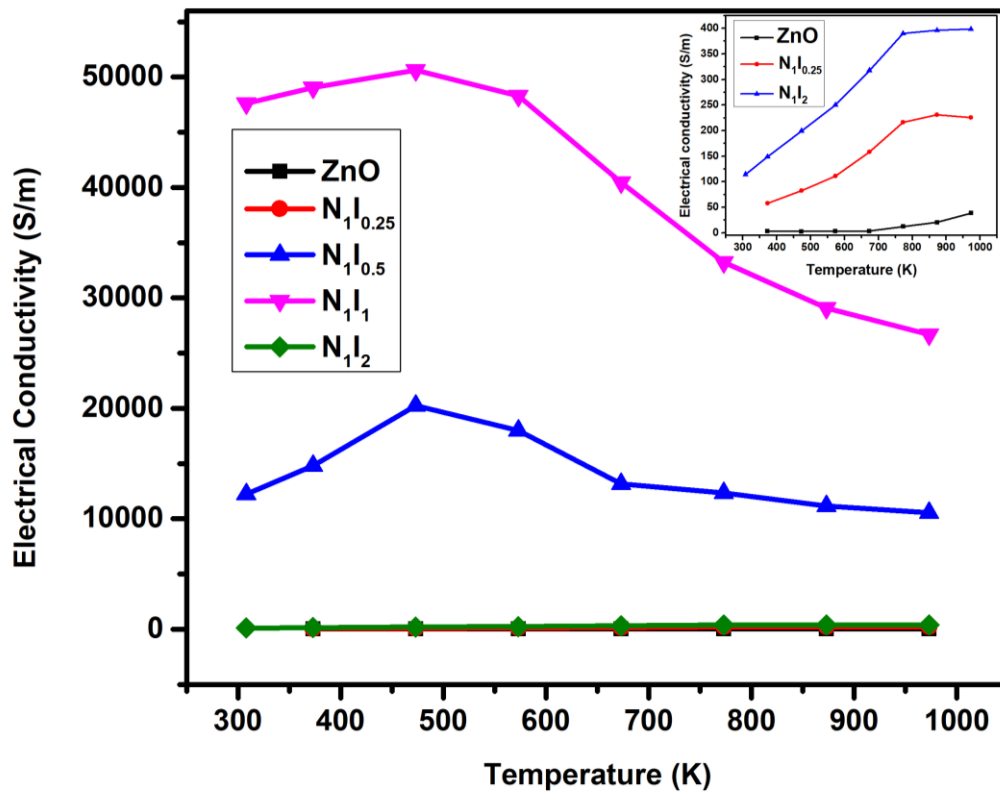


Fig 3.6 Electrical conductivity of the samples with temperature

3.3.4.2 Seebeck coefficient

Seebeck coefficient is the measure of potential difference developed in a material under a temperature difference. The variation of the Seebeck coefficient of samples with temperature is shown in Fig 3.7. The negative Seebeck coefficient in the whole measuring temperature range indicates that the conduction mechanism is mainly governed by electrons and the samples have n-type conductivity.

The Seebeck coefficient measurement is in agreement with the electrical conductivity measurements, the samples with higher electrical conductivity have lower Seebeck coefficient. Due to low carrier concentration, undoped ZnO has the highest Seebeck coefficient of $-584.95 \mu\text{V/K}$ at 973 K which is greater than the doped samples. The Seebeck coefficient of doped samples is found to be decreasing than the pristine ZnO. The Ni₁I_{0.25} sample possesses higher value of Seebeck coefficient among the doped samples. It is found that as the temperature increases,

all the doped samples show an increase in the value of the Seebeck coefficient. The Seebeck coefficient decreases up to sample N₁I₁ and the sample N₁I_{0.02} shows an increase in the Seebeck coefficient.

The Seebeck coefficient and the carrier concentrations (n) have an inverse relationship as per Mott's relation,

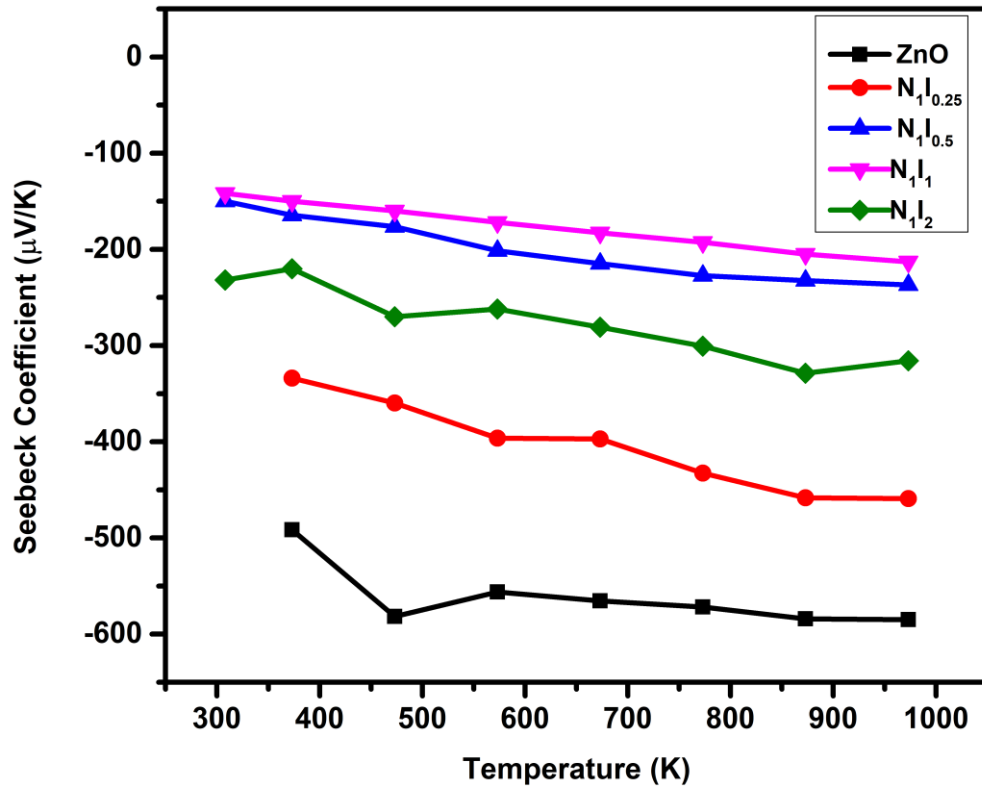
$$S = \frac{8\pi^2 k_B^2 m^* T}{3e\hbar^2} \left(\frac{\pi}{3n}\right)^{2/3} \quad (3.6)$$

Where m^* is the effective mass, k_B is the Boltzmann constant. Low carrier concentration and high effective mass are favourable for the enhancement of the Seebeck coefficient. Doping increases carrier concentration, the Seebeck coefficient decreases accordingly. The different electronegativity of Ni (1.91) and In (1.78) causes a fluctuating potential in the crystal structure leading to a decrease in the mobility of carriers. Reduced mobility results in high effective mass. It can be seen that even though doping induces more charge carriers, the effective mass and thereby Seebeck coefficient increases with an increase in doping concentration⁵.

The derived Fermi level energy, $E_c - E_f$ from the conduction band edge are listed in the Table 3.2. It is evident that the derived Fermi level energy of both doped and undoped samples are negative indicating that all the samples are degenerate and their Fermi energy will shift above the conduction band¹⁴. Materials with lowest Fermi energy have lower Seebeck coefficient, and the thermally induced shift of the valance band and conduction band cause an increase in the Seebeck coefficient of the doped samples²⁴. At high temperatures, phonon-phonon interaction dominates over electron-phonon interaction, which causes a rise in the Seebeck coefficient.

Table 3. 2 Fermi level shift from the conduction band edge of doped and undoped samples

Sample	$E_c - E_f$ (eV)
ZnO	-0.0531 ± 0.002
$N_1I_{0.25}$	-0.0773 ± 0.007
$N_1I_{0.5}$	-0.0500 ± 0.001
N_1I_1	-0.0313 ± 0.003
N_1I_2	-0.0549 ± 0.006

**Fig 3.7** Variation of Seebeck coefficient of the samples with temperature

3.3.4.3 Power factor

The power factor $S^2\sigma$, which is the function of the Seebeck coefficient and electrical conductivity, represents the electrical contribution to the thermoelectric performance of a material. The enhanced electrical conductivity and Seebeck coefficient result in the highest power factor for the doped samples as depicted in Fig 3.8. A power factor of $13.2 \mu\text{W}/\text{mK}^2$ is obtained for pure ZnO, whereas $48.6 \mu\text{W}/\text{mK}^2$ at 873 K, $638 \mu\text{W}/\text{mK}^2$ at 773 K, $1427 \mu\text{W}/\text{mK}^2$ at 573 K, $42.8 \mu\text{W}/\text{mK}^2$ at 873 K are the power factors obtained for the In 0.0025, 0.005 0.01, 0.02 doped samples respectively. Among the doped samples, N_1I_1 has the highest power factor which is more than 100 times greater than the power factor of pure ZnO. This power factor is greater than the values obtained for Ni, In singly doped ZnO samples and Mn and Al, Al and B, Fe and Co, In and Ga, Ce and Dy dual doped ZnO samples^{4, 5, 12, 13, 25-27}. Therefore, nickel and indium dual-doped samples can be considered a good candidate for thermoelectric applications.

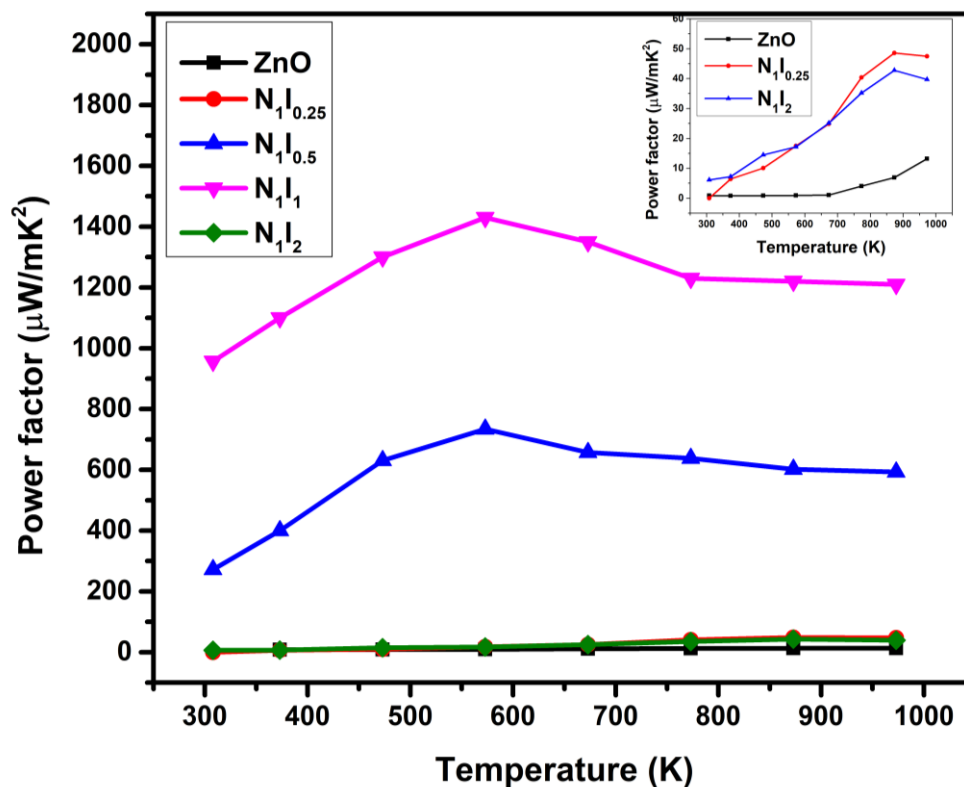


Fig 3.8 Variation of power factor of the samples with temperature

3.3.4.4 Thermal conductivity

The high thermal conductivity of ZnO limits its thermoelectric performance and one of the methods to reduce the thermal conductivity is the introduction of lattice defects through doping, which modify the microstructure and enhance the grain boundary scattering²⁸. The thermal conductivity of both doped and undoped samples show an exponential decay with temperature as depicted in Fig 3.9. All the doped samples possess low thermal conductivity than the pristine sample. The κ value of doped samples was found to decrease with the increasing addition of indium, and temperature dependence of thermal conductivity drastically reduced for all the samples. Ohtaki et al. and A. Paulson et al. reported similar behaviour of doped ZnO^{9, 14, 18}. The sample N₁I₁ has a low thermal conductivity of 10 W/mK among all other doped materials. Thermal conductivity of 13 W/mK, 11 W/mK and 12 W/mK are obtained for the samples doped with In 0.0025, In 0.005 and In 0.02 respectively.

The total thermal conductivity of the solids is the measure of the thermal conductivity from the electronic and lattice contributions,

$$\kappa_{total} = \kappa_l + \kappa_e \quad (3.7)$$

where κ_{total} is the total thermal conductivity, κ_e is the electrotonic contribution to thermal conductivity and κ_l is the lattice thermal conductivity. The electronic thermal conductivity can be estimated from the Wiedmann-Franz law, $\kappa_e = L_0 \sigma T$ where $L_0 = 2.45 \times 10^{-8} \text{ V}^2 \text{ K}^{-8}$ is the Lorentz constant, T is the absolute temperature, and σ is the electrical conductivity.

Doping will induce phonon scattering which causes reduction in thermal conductivity. Dual doping into the ZnO lattice (Zn²⁺ ionic radius = 0.74 Å) with In³⁺ of large ionic radii (0.80 Å) along with Ni²⁺ (0.70 Å) will cause large lattice distortions and defects in the host lattice. The increased distortions and defects act as a hindrance to the phonon movement in the lattice which in turn reduces the lattice contributions in the thermal conductivity of the materials⁴. Dual doping of Ni and In causes a large increase in electron concentration, which will contribute to electronic thermal conductivity²⁹. The increase in electronic thermal conductivity and decrease in lattice thermal conductivity sustain the K value of prepared samples into a moderate value.

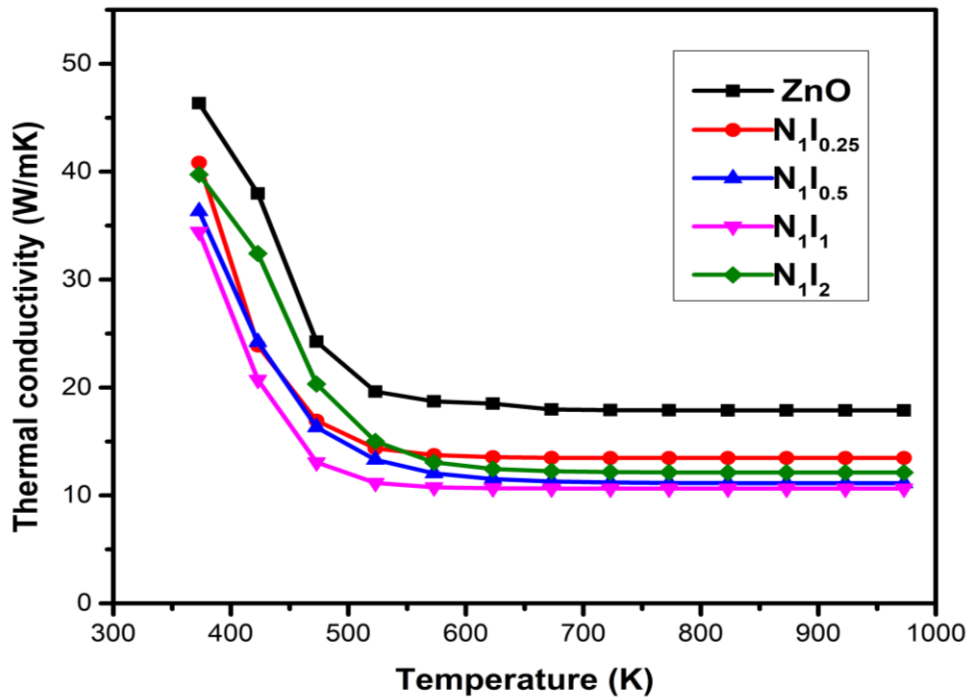


Fig 3.9 Variation of thermal conductivity of the samples with temperature

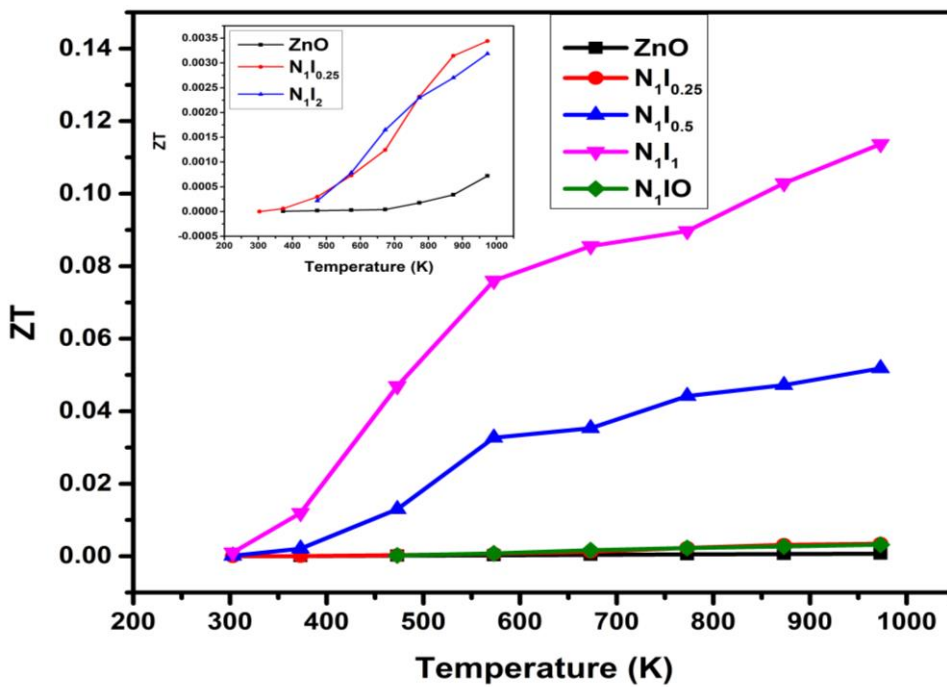


Fig 3.10 Variation of figure of merit of the samples with temperature

3.3.4.5 Figure of merit

The variation of the figure of merit of the prepared samples with temperature is presented in Fig 3.10. The figure of merit of Ni and In dual doped ZnO is greater than the undoped sample and it increases with the temperature. The sample N₁I₁ has high electrical conductivity and low thermal conductivity, but its low Seebeck coefficient limits the figure of merit of the sample to 0.11. However, owing to their highest power factor, nickel and indium dual doped materials can be effectively used in thermoelectric power generation applications. A table comparison of the power factor (PF) and figure of merit (ZT) of ZnO with other dopants is given in Table 3.3.

Table 3.3 Comparison of PF and ZT with different dopants

Dopant	PF ($\mu\text{Wm}^{-1} \text{K}^{-2}$)	ZT
Ni ¹²	600	0.09
Al, Ni ³	616	0.057
In, Ga ⁵	88.6	0.019
In ¹³	466	-
Nb ³⁰	484	0.06
Al, Mn ⁴	657	0.07

3.4 Conclusion

Nickel and Indium dual doped zinc oxide materials were prepared by solid state reaction method and structural, morphological, optical and thermoelectric characterisations were carried out. The strain induced in the lattice and variation in crystallite size estimated from the X-ray diffraction analysis confirms the inclusion of dopant ions into the host structure. FESEM-EDS images clearly show the perfect inclusions of the dopants and the morphological variations occurred due to the incorporation of dopant ions of different ionic radii. The optical band gap energy is reduced by 2.20 eV, a reduction of 70% from the band gap energy of the undoped sample with a redshift in the absorption edge. The substitution of dual dopants into ZnO leads to higher electrical conductivity. The increase in electrical conductivity

and decrease in the Seebeck coefficient was attributed to the high charge carrier density. A power factor of $1427 \mu\text{W}/\text{mK}^2$ at 573 K was obtained for sample N₁I₁, which is more than 100 times greater than the undoped ZnO. The thermal conductivity of dual doped ZnO samples shows a significant reduction due to the increased defects formed upon doping. A large enhancement in the figure of merit was observed as a result of the improved power factor and reduced thermal conductivity. Among all the prepared samples, N₁I₁ shows better thermoelectric efficiency of 0.11 and can be used as a good thermoelectric material for waste heat recovery.

References

1. M. Ohtaki, *Journal of the Ceramic Society of Japan* **119** (1395), 770-775 (2011).
2. L. Han, N. Van Nong, T. Holgate, N. Pryds, M. Ohtaki and S. Linderoth, *Journal of alloys and compounds* **555**, 291-296 (2013).
3. D.-B. Zhang, B.-P. Zhang, D.-S. Ye, Y.-C. Liu and S. Li, *Journal of Alloys and Compounds* **656**, 784-792 (2016).
4. J. Hoemke, A. U. Khan, H. Yoshida, T. Mori, E. Tochigi, N. Shibata, Y. Ikuhara and Y. Sakka, *Journal of the Ceramic Society of Japan* **124** (5), 515-522 (2016).
5. N. H. Tran Nguyen, T. H. Nguyen, Y.-r. Liu, M. Aminzare, A. T. T. Pham, S. Cho, D. P. Wong, K.-H. Chen, T. Seetawan and N. K. Pham, *ACS Applied Materials & Interfaces* **8** (49), 33916-33923 (2016).
6. K. V. Zakharchuk, M. Widenmeyer, D. O. Alikin, W. Xie, S. Populoh, S. M. Mikhalev, A. Tselev, J. R. Frade, A. Weidenkaff and A. V. Kovalevsky, *Journal of Materials Chemistry A* **6** (27), 13386-13396 (2018).
7. Y. Feng, X. Jiang, E. Ghafari, B. Kucukgok, C. Zhang, I. Ferguson and N. Lu, *Advanced Composites and Hybrid Materials* **1** (1), 114-126 (2018).
8. T. Tsubota, M. Ohtaki, K. Eguchi and H. Arai, presented at the XVI ICT'97. Proceedings ICT'97. 16th International Conference on Thermoelectrics (Cat. No. 97TH8291), 1997 (unpublished).
9. M. Ohtaki, K. Araki and K. Yamamoto, *Journal of Electronic Materials* **38** (7), 1234-1238 (2009).
10. B. Zhu, C. Chen, Z. Yao, J. Chen, C. Jia, Z. Wang, R. Tian, L. Tao, F. Xue and H. Hng, *Journal of the European Ceramic Society* **41** (7), 4182-4188 (2021).
11. C. Wang, W. Su, A. Zaman, I. Ullah, J. Zhai and D. Liu, *Journal of Materials Science: Materials in Electronics* **29** (11), 9555-9563 (2018).
12. H. Colder, E. Guilmeau, C. Harnois, S. Marinel, R. Retoux and E. Savary, *Journal of the European Ceramic Society* **31** (15), 2957-2963 (2011).
13. M. Ullah, W. Chunlei, W.-B. Su, A. Manan, A. S. Ahmad and A. U. Rehman, *Journal of Materials Science: Materials in Electronics* **30** (5), 4813-4818 (2019).
14. A. Paulson, N. M. Sabeer and P. Pradyumnan, *Journal of Alloys and Compounds* **786**, 581-587 (2019).
15. A. K. Zak, W. A. Majid, M. E. Abrishami and R. Yousefi, *Solid State Sciences* **13** (1), 251-256 (2011).
16. T. M. Hammad, J. K. Salem, R. G. Harrison, R. Hempelmann and N. K. Hejazy, *Journal of Materials Science: Materials in Electronics* **24** (8), 2846-2852 (2013).
17. K. Saw, N. Aznan, F. Yam, S. Ng and S. Pung, *PloS one* **10** (10), e0141180 (2015).

18. T. Tsubota, M. Ohtaki, K. Eguchi and H. Arai, *Journal of Materials Chemistry* **7** (1), 85-90 (1997).
19. T. A. Dar, A. Agrawal and P. Sen, (2013).
20. M. Caglar, Y. Caglar, S. Aksoy and S. Ilcan, *Applied Surface Science* **256** (16), 4966-4971 (2010).
21. M. Shaheera, K. Girija, M. Kaur, V. Geetha, A. Debnath, R. Vatsa, K. Muthe and S. Gadkari, *Optical Materials* **101**, 109723 (2020).
22. S. C. Das, R. J. Green, J. Podder, T. Z. Regier, G. S. Chang and A. Moewes, *The Journal of Physical Chemistry C* **117** (24), 12745-12753 (2013).
23. M. Sajjad, I. Ullah, M. Khan, J. Khan, M. Y. Khan and M. T. Qureshi, *Results in Physics* **9**, 1301-1309 (2018).
24. D. M. Rowe, *Thermoelectrics handbook: macro to nano*. (CRC press, 2018).
25. M. Ullah, S. Ullah, A. Manan, F. Khan, F. Zeb, I. Mehmood, M. U. Rehman and M. Amami, *Applied Physics A* **128** (2), 1-7 (2022).
26. K. Park, H. Hwang, J. Seo and W.-S. Seo, *Energy* **54**, 139-145 (2013).
27. A. Pashkevich, A. Fedotov, E. Poddenezhny, L. Bliznyuk, J. Fedotova, N. Basov, A. Kharchanka, P. Zukowski, T. Koltunowicz and O. Korolik, *Journal of Alloys and Compounds* **895**, 162621 (2022).
28. G.-K. Ren, J.-L. Lan, K. J. Ventura, X. Tan, Y.-H. Lin and C.-W. Nan, *npj Computational Materials* **2** (1), 1-9 (2016).
29. S. Katsuyama, Y. Takagi, M. Ito, K. Majima, H. Nagai, H. Sakai, K. Yoshimura and K. Kosuge, *Journal of applied physics* **92** (3), 1391-1398 (2002).
30. N. Wang, H. Xin, D. Li, X. Li, J. Zhang and X. Qin, *Journal of Physics and Chemistry of Solids* **74** (12), 1811-1815 (2013).

Chapter 4

Nickel and praseodymium, codoped zinc oxide materials for thermoelectric applications

This chapter deals with the thermoelectric studies of rare-earth element praseodymium and transition element nickel codoped ZnO. The introduction of dopants with large ionic radii will reduce the thermal conductivity of the parent material, hence the thermoelectric performance can be enhanced without much reduction in electrical conductivity. Simultaneous increments in electrical conductivity and Seebeck coefficient occurred up on codoping.

4.1 Introduction

As the population increases, energy consumption increases accordingly. The scarcity and depletion of fossil fuels demand alternate energy sources which are sufficient to fulfill all the energy requirements of society. The invention of thermoelectric power-generating systems will reduce energy deficiency to a great extent. Electrical energy from waste heat can be effectively harvested by the use of solid-state energy conversion device-thermoelectric generators (TEGs). TEGs are widely used because of their attractive features such as their efficiency, long life and maintenance free as these devices have no moving parts^{1, 2}.

The efficiency of thermoelectric conversion is represented by the figure of merit,

$$ZT = \frac{S^2 \sigma}{k_e + k_l} T \quad (4.1)$$

Here S , σ , κ_e , κ_l and T are the Seebeck coefficient, electrical conductivity, electronic thermal conductivity, lattice thermal conductivity and temperature respectively. This equation necessitates searching for materials with high electrical conductivity and low thermal conductivity. However, materials with high electrical conductivity are also good thermal conductors. So, it is difficult to maintain a high thermal gradient between the materials to generate high thermoelectric emf. Simultaneous enhancement of electrical conductivity and Seebeck coefficient will increase the power factor ($S^2\sigma$) and it can be achieved through band engineering and density of state modifications^{3, 4}. Attempt to reduce thermal conductivity will decrease the electrical conductivity as both parameters adhere to carrier concentration. Since thermal conductivity consists of the contribution from electrons and phonons, reducing the lattice part of thermal conductivity is more favourable to attaining low thermal transport. Introduction of defects and nanostructuring methods are used to minimize the lattice thermal conductivity which effectively scatters phonons and reduces its mean free path⁵. Defects can be induced by the introduction of atoms in a crystal structure, and if the dopant atoms are of larger ionic radii the defects will be more. Rare earth elements have larger ionic radii, so the inclusion of such elements

into the host will create more lattice imperfections and reduce the phonon conduction⁶⁻¹⁰.

In this chapter, we have focussed on the thermoelectric properties of nickel and praseodymium codoped ZnO. Yoshihiro Inoue et al. reported the enhancement of the power factor of ZnO up on praseodymium doping¹¹. Heavy element praseodymium creates more lattice imperfections and enhances the phonon scattering leading to the suppression of lattice thermal conductivity of the host structure¹². Reports reveal that the introduction of transition metals as a single dopant or codopant improves the thermoelectric properties of ZnO¹³⁻¹⁵. Codoping of nickel and praseodymium will improve the thermoelectric performance of ZnO by enhancing electrical transport and subduing thermal conduction.

4.2 Experimental method

Pure oxides (99.99%) of nickel, praseodymium, and zinc were weighed according to the composition $Zn_{(1-x-y)}Ni_xPr_yO$ ($x=0.01$, $y=0.003,0.005,0.007$), and ground for 1hour. Calcination of the powders was done at 450°C for 4 hours. Pellets of calcinated powders were sintered at 1300°C for 4 hours in a high temperature furnace at a cooling/heating rate of 5°C per minute. The sintered samples were used for characterisation studies. The dual doped materials are termed as $N_1P_{0.3}$ (Ni=1%, Pr=0.3%), $N_1P_{0.5}$ (Ni=1%, Pr=0.5%), and $N_1P_{0.7}$ (Ni=1%, Pr=0.7%)

4.3 Results and discussions

4.3.1 Structural characterisations

The X-ray diffraction pattern of $Zn_{(1-x-y)}Ni_xPr_yO$ ($x=0.01$, $y=0.003,0.005,0.007$) samples are shown in Fig 4.1. The peaks are indexed according to the ICSD card No: 29272. Major peaks were obtained at (101) and weak reflections occurred at (100), (002), (110), (102), (103), (112) planes, which means that the prepared samples belonging to the hexagonal wurtzite structure as ZnO. No secondary phase growth of nickel and praseodymium was observed in the XRD pattern, indicating the perfect inclusion of the dopants into the host lattice. The incorporation of Ni and

Pr ions in the ZnO lattice is also confirmed by the variation in crystallite size and microstrain induced in the doped samples, which are listed in Table 4.1.

The crystallite size of the samples is calculated using the Scherrer formula and the strain (ϵ) produced in the lattice is determined by the Wilson formula,

$$\epsilon = \frac{\beta_{hkl}}{4\tan\theta} \quad (4.2)$$

The Pr^{3+} and Ni^{2+} ions may occupy the interstitial position of the ZnO lattice and they will produce lattice distortions which lead to a reduction in crystallite size (D)¹⁶. Also, these dopants will hinder and suppress the diffusion and grain growth of ZnO crystallites¹⁷. The decrease in crystallite size is confirmed by the decrease in peak intensity in the XRD patterns. The negative slope indicates the compressive nature of strain and the strain variation is observed as the lower angle peak shift in the XRD pattern of the samples. The peak shift observed in the (101) plane is depicted in Fig 4.2. The microstrain developed in the ZnO lattice is due to the dual substitution of an ion with a large ionic radius ($\text{Pr}^{3+} = 1.013 \text{ \AA}$) along with nickel ($\text{Ni}^{2+} = 0.69 \text{ \AA}$), which leads to deviation in the lattice constants¹⁸. K.D.A. Kumar et al. reported the same variations in crystallite size and microstrain¹⁶.

Table 4.1 Crystallite size and strain produced in the samples

Sample	Crystallite size D (nm)	Strain (ϵ) (10^{-4})
ZnO	59.25	-0.254
$\text{N}_1\text{P}_{0.3}$	55.3	-1.66
$\text{N}_1\text{P}_{0.5}$	54.5	-0.095
$\text{N}_1\text{P}_{0.7}$	51.9	-0.874

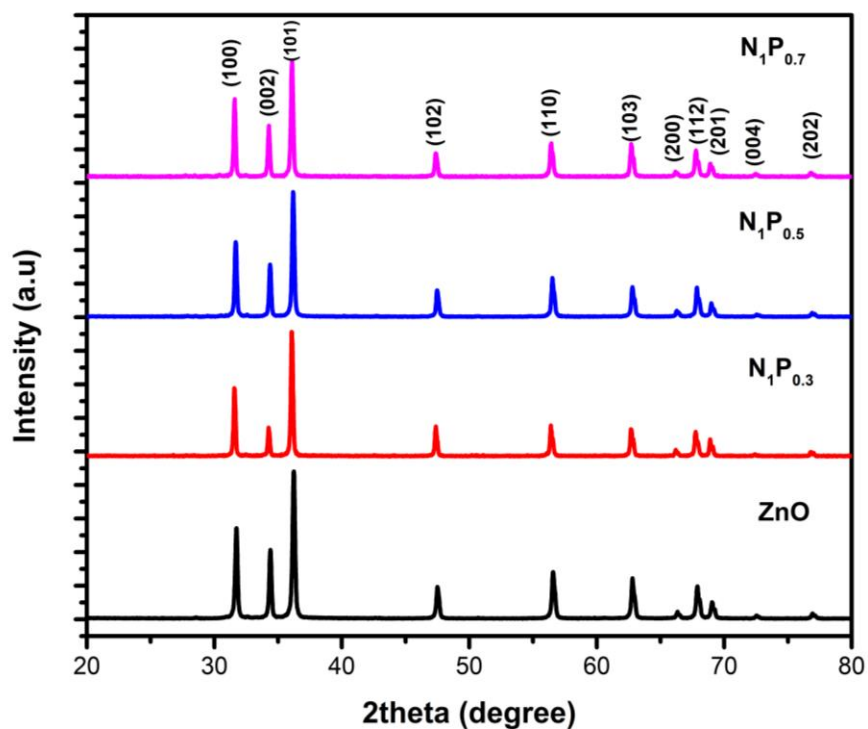


Fig 4.1 XRD patterns of prepared samples

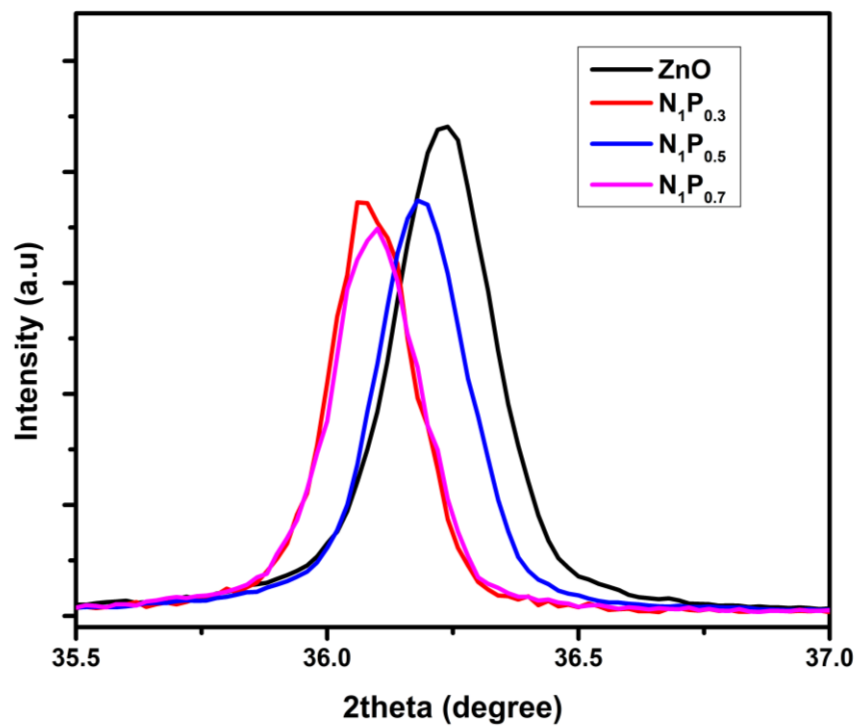


Fig 4.2 Peak Shift of (101) plane

4.3.2 FESEM and EDAX analysis

The surface morphological analysis of the samples was done with Field emission scanning electron microscope and the FESEM micrographs are shown in Fig 4.3. SEM image of pure ZnO has uniform particle distribution and it confirmed the hexagonal structure of ZnO as obtained from the XRD pattern. The structural deformation of the ZnO lattice due to the incorporation of larger Pr^{3+} and Ni^{2+} ions can be evident from the images. The morphology of the doped samples deviated from pristine ZnO and the grain growth in the doped samples was highly influenced by the dopant concentration.

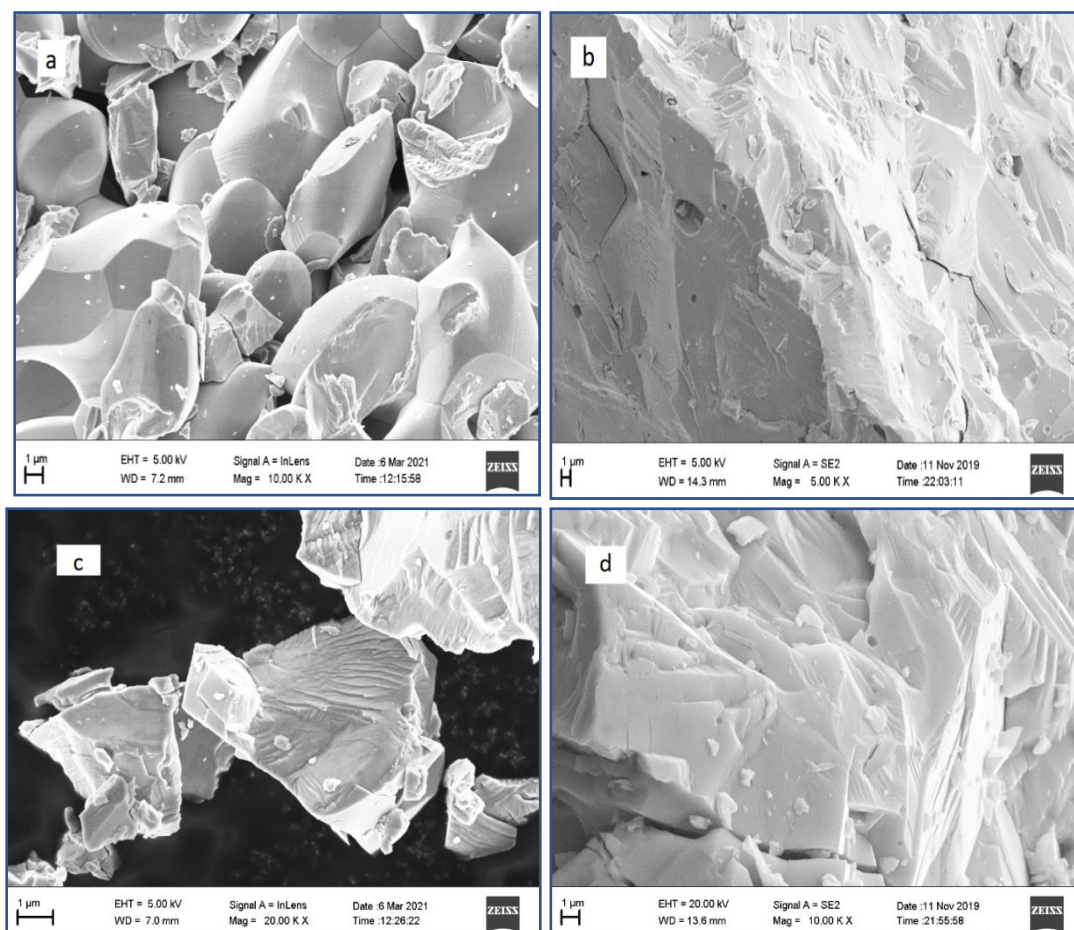


Fig 4.3 FESEM images of (a) ZnO (b) $\text{Ni}_1\text{P}_{0.3}$ (c) $\text{Ni}_1\text{P}_{0.5}$ (d) $\text{Ni}_1\text{P}_{0.7}$

The elemental composition of the materials was identified by Energy Dispersive X-ray analysis (EDX). EDX analysis confirmed the substitution of the dopants, only

the signals of Zn, O, Ni and Pr were detected from the analysis as presented in Table 4.2 and Fig.4.4 The EDS mapping of the sample $N_1P_{0.5}$ is shown in Fig 4.5.

Table 4.2 Elemental composition of the samples

Elements	ZnO		$N_1P_{0.3}$		$N_1P_{0.5}$		$N_1P_{0.7}$	
	wt%	at%	wt%	at%	wt%	at%	wt%	at%
Zinc	74.15	58.76	76.38	45.27	76.27	44.79	81.19	53.34
Oxygen	25.85	41.24	22.31	54.04	22.43	54.44	17.18	46
Nickel			0.87	0.58	0.78	0.46	0.92	0.42
Praseodymium			0.43	0.12	0.52	0.14	0.69	0.24

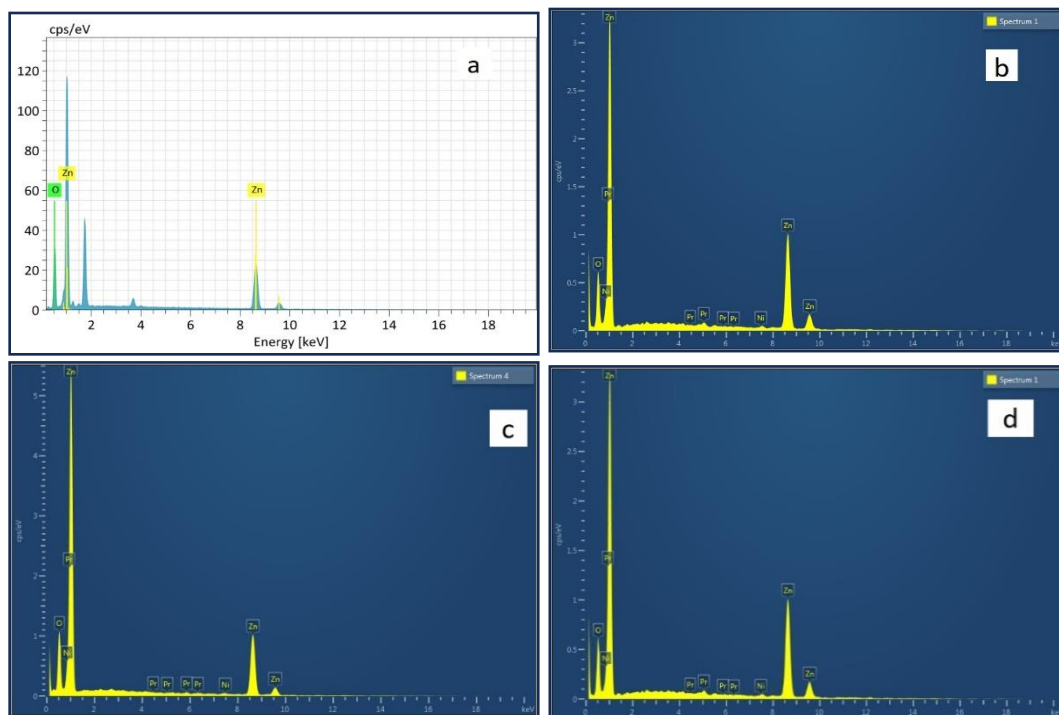


Fig 4.4 EDAX images of (a) ZnO (b) $N_1P_{0.3}$ (c) $N_1P_{0.5}$ (d) $N_1P_{0.7}$

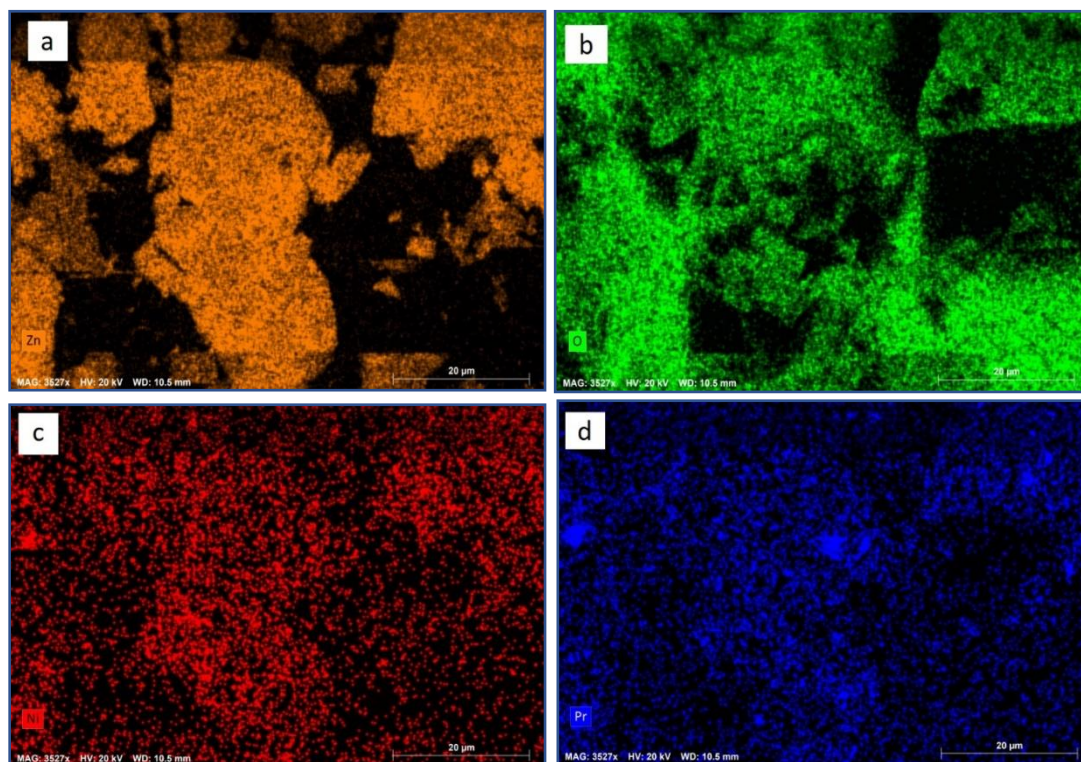


Fig 4.5 EDS mapping of $Ni_1P_{0.5}$ (a) Zinc (b) Oxygen (c) Nickel (d) Praseodymium

4.3.3 UV-Vis spectroscopic analysis

UV-Vis analysis was performed to study the optical properties of the undoped and doped samples. Since ZnO is a semiconductor with direct band gap energy, the optical band gap energy of the samples is determined from the Tauc's relation. Strong absorption in the ultraviolet region is observed in the prepared samples and the absorption edge shifted to the higher energy region of the spectrum. The red shift in absorption edge is confirmed by the optical band gap energy of the samples, determined from the graph plotted between $(\alpha h\nu)^2$ and $h\nu$. The linear extrapolation of the curves to the energy axis gives the band gap energy of the materials. The optical band gap energy of pure ZnO is 3.15 eV, and it is reduced to 2.26 eV when doping with Pr^{3+} and Ni^{2+} ions as depicted in Fig 4.6. Lattice strain, stoichiometric deformation, carrier density, grain boundaries etc. will affect the band gap energy of the samples. Dual doping with Pr^{3+} , which has a large ionic radius (1.013 Å) than Zn^{2+} , along with Ni^{2+} ions of ionic radius 0.69 Å will induce large lattice distortions

which in turn cause a decrease in optical band gap energy. The reduction in crystallite size and increase in strain may also result in a narrow band gap¹⁹.

The decrement of the band gap may also arise due to the many-body interactions such as electron-impurity interaction and electron-electron scattering that occurred at the valance band and conduction band. Fraction of the added impurity dopant atoms undergo ionisation which will reduce the free energy, as a result, the ionised impurities will contribute some amount of free electrons in the conduction band. The energy of the free electron-impurity cloud is lower than the energy of randomly distributed electrons. So the conduction band will move down leading to a decrease in band gap energy. The minority carrier-impurity interaction energy will also decrease, which causes more holes to move into the region with high electron density. Due to this interaction rising of the valance band occurred, consequently, band gap energy decreases^{20,21}.

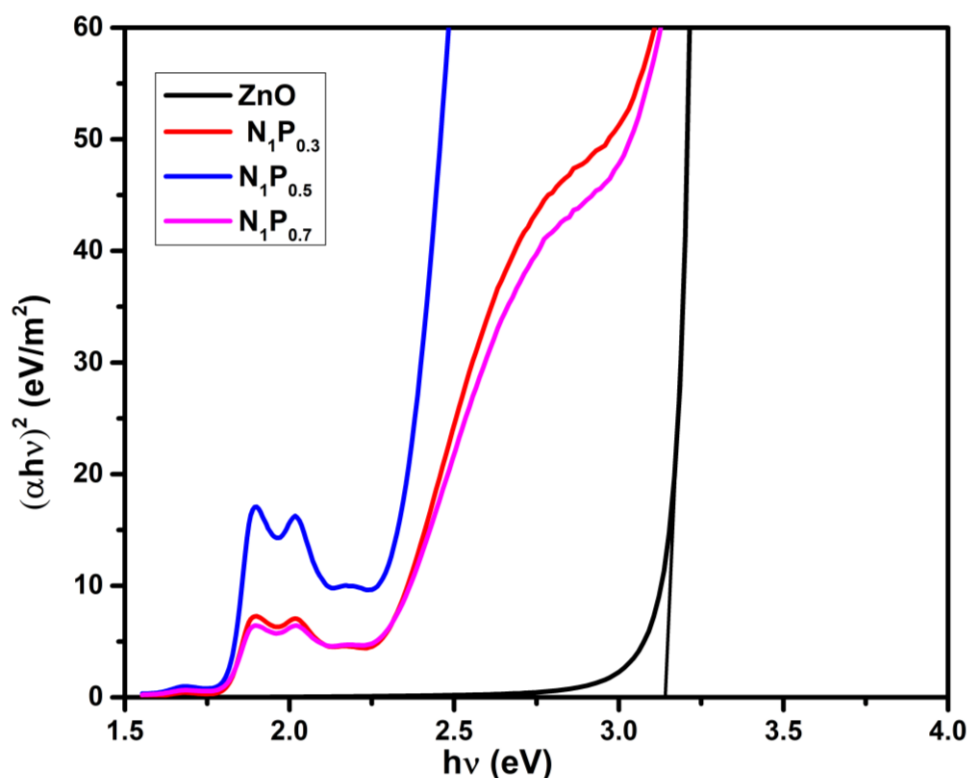


Fig 4.6 Tauc's plot of undoped and doped samples

4.3.4 Thermoelectric property studies

4.3.4.1 Electrical conductivity

Enhanced electrical conductivity of ZnO is due to the presence of oxygen vacancies and zinc interstitials. Herein, codoping creates more defects in the form of oxygen vacancies and zinc interstitials, which is responsible for the increase in electrical conductivity of the doped samples. The temperature-dependent electrical conductivity of the samples is shown in Fig 4.7. The dopant's substitution will increase the charge carrier density, leading to an increase in electrical conductivity. The inclusion of ions with higher valency than Zn^{2+} will induce more charge carriers into the host lattice^{22, 23}. The Ni and Pr doping will shift the Fermi level into the conduction band²⁴. The electron concentration increases with an increase in dopant substitution which is confirmed by the Hall measurement analysis. $6.20 \times 10^{19} \text{ m}^{-3}$, $1.23 \times 10^{20} \text{ m}^{-3}$, $3.52 \times 10^{20} \text{ m}^{-3}$, and $5.37 \times 10^{20} \text{ m}^{-3}$ are the carrier density obtained for the ZnO and doped samples $\text{N}_1\text{P}_{0.3}$, $\text{N}_1\text{P}_{0.5}$, $\text{N}_1\text{P}_{0.7}$ respectively.

It is observed that the doped and undoped samples exhibit semiconducting behaviour. At low temperatures, the doped samples show low electrical conductivity than the pure ZnO. For a doped semiconductor, most of the free electrons provided by the dopants are recaptured by the donor atoms. So the electron hopping between the impurity bands dominates over the free electron band conduction in the low temperature region^{25, 26}. Also, the scattering of conduction electrons by phonons may occur at low temperatures²⁷. As the temperature increases, due to the thermal excitation of free electrons from the donor energy level to the conduction band, which will contribute to the conduction mechanism, the codoped samples exhibit better electrical conductivity than the undoped ZnO samples. The electrical conductivity of the doped samples decreases with an increase in dopants concentration.

The electrical conductivity increases with carrier concentration according to the relation $\sigma = ne\mu$, where n , e , and μ are the carrier concentration, electronic charge and carrier mobility respectively. But the increased carrier density will cause a

reduction in carrier mobility as a consequence of the carrier-carrier interaction and the scattering produced by the introduction of defects to the crystal structure^{28, 29}. As a result, the electrical conductivity of heavily doped samples will decrease. The decrease in electrical conductivity can be explained by the grain boundary scattering mechanism and since the crystallite size decreases with doping concentration, it increases the grain boundary scattering in the samples, resulting in a reduction in the electrical conductivity³⁰.

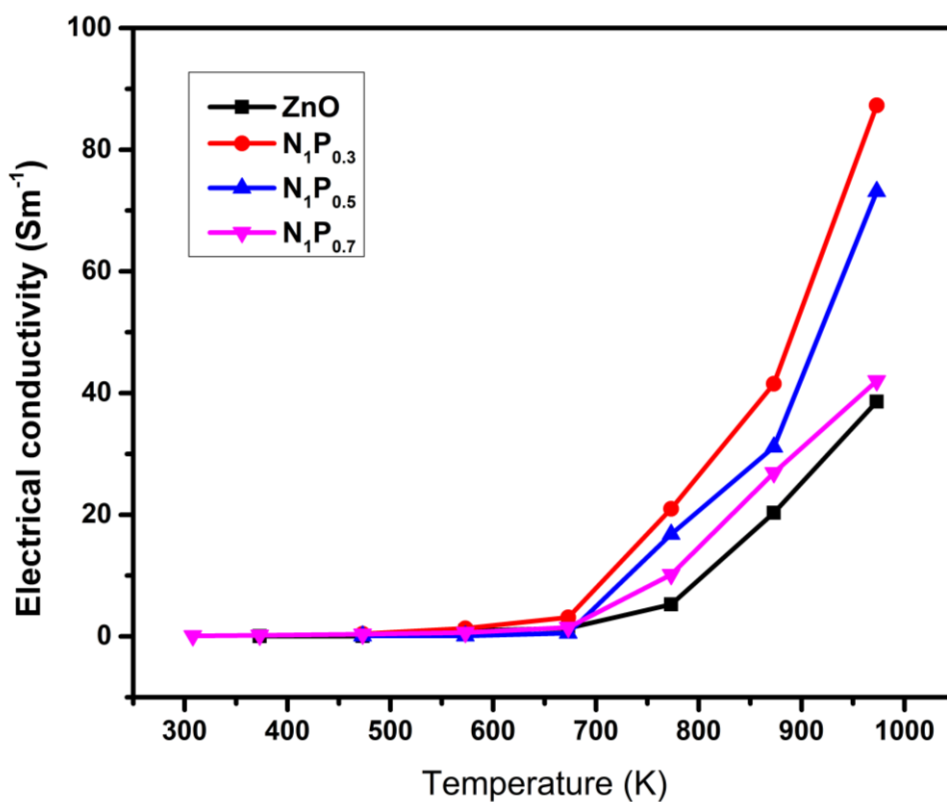


Fig 4.7 Electrical conductivity of undoped and doped samples

4.3.4.2 Seebeck coefficient

The variation of the Seebeck coefficient with temperature is shown in Fig 4.8. The sign of the Seebeck coefficient in the measuring temperature range is negative, indicating that the majority of carriers for conduction are electrons. All the samples show a higher Seebeck coefficient than the undoped material and sample N₁P_{0.5} has a higher Seebeck coefficient of $-716 \mu\text{V K}^{-1}$. This value is greater than the Seebeck

coefficient obtained for praseodymium singly doped ZnO⁶. However, analysis of the Seebeck coefficients of sample N₁P_{0.5} reveals that due to its gradual decrease in the seebeck coefficient with temperature, it can only be employed in the low temperature range. But the samples N₁P_{0.3} and N₁P_{0.7} are more suitable for high temperature application as they maintained better performance with increasing temperature. The doped materials generally exhibit high electrical conductivity and low Seebeck coefficient, since these two thermoelectric parameters have inverse dependence on the carrier density. Doping increases the carrier density and thereby increases electrical conductivity, whereas the Seebeck coefficient decreases with carrier density, according to Mott's relation. But in this case, Ni and Pr doping increases both electrical conductivity and the Seebeck coefficient. So besides the effect of carrier density, another factor may influence the Seebeck coefficient of the doped samples. Dedoping and energy filtering are the most effective methods to enhance the Seebeck coefficient³¹. But low doping levels cause a reduction in electrical conductivity as it depends on carrier density. So energy filtering is the most adapted method to increase the Seebeck coefficient without reducing the electrical conductivity. According to this, band bending occurs at the metal-semiconductor interface and which causes the scattering of low-energy charge carriers leading to the enhancement of the Seebeck coefficient³². The Seebeck coefficient of all the samples shows a decrease with increasing temperature. At high temperatures, thermal excitation of minority carriers occurs, and as a result of bipolar effects, a reduction in the Seebeck coefficient is observed³³.

The Fermi level shift, $E_c - E_f$ observed for the doped samples is listed in Table 4.3. A negative value of the Fermi level shift demonstrates that the materials are degenerate semiconductors and the Fermi level shift above the conduction band. The Fermi level shift of N₁P_{0.7} is positive, indicating that the Fermi level occupies inside the band gap. The low electrical conductivity obtained for this sample also confirmed the occupancy of the Fermi level inside the band gap³⁴.

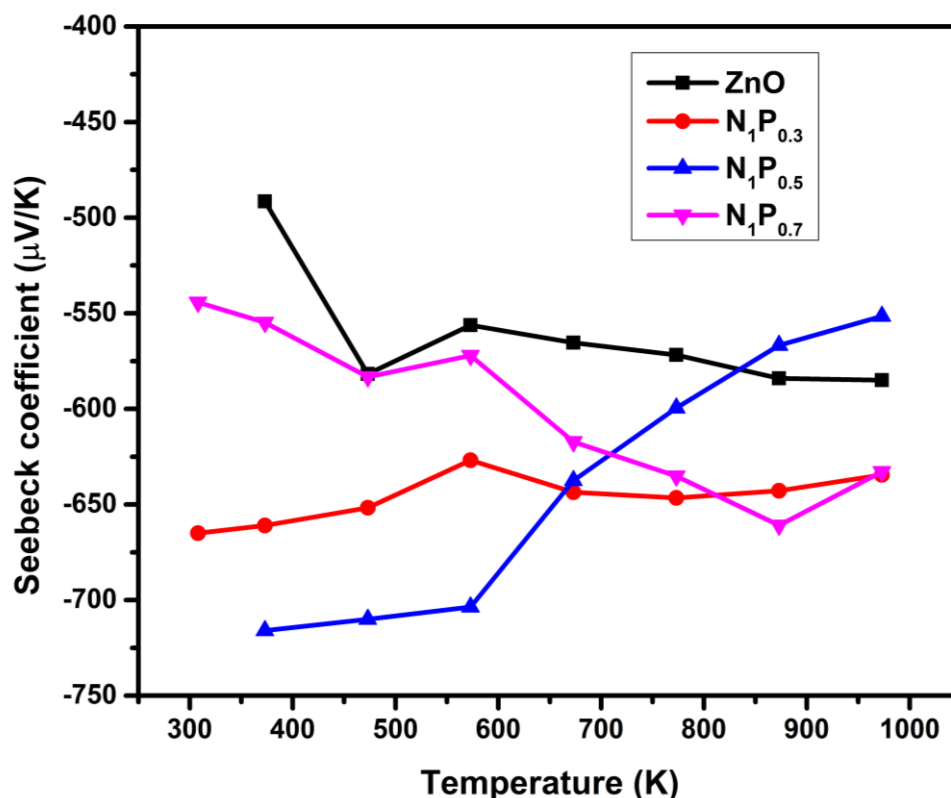


Fig 4.8 Seebeck coefficient of undoped and doped samples

Table 4.3 Fermi level shift observed in the samples

Sample	$E_c - E_f$ (eV)
ZnO	-0.0531 ± 0.002
N ₁ P ₃	-0.0125 ± 0.004
N ₁ P _{0.5}	-0.1075 ± 0.022
N ₁ P _{0.7}	0.0490 ± 0.008

4.3.4.3 Power factor

The power factor, ($S^2\sigma$) represents the electrical transport properties of a material and it is essential to increase the power factor to attain the highest thermoelectric figure of merit. The simultaneous increase in electrical conductivity and Seebeck coefficient will increase the power factor. The power factor of the doped samples is greater than the pure ZnO as shown in Fig 4.9. The increase in the Seebeck

coefficient and electrical conductivity are responsible for the increase in the power factor of the nickel and praseodymium doped ZnO samples.

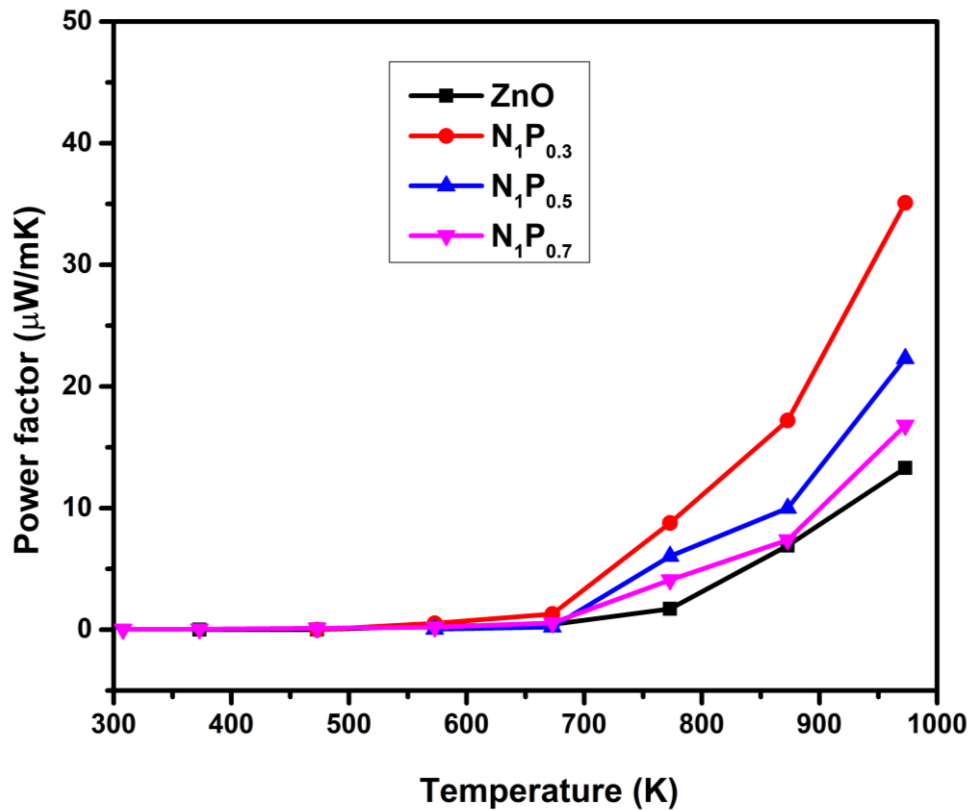


Fig 4.9 Power factor of undoped and doped samples

4.3.4.4 Thermal conductivity

The total thermal conductivity (κ) of a material is related to the contributions of phonons (κ_l) and electrons (κ_e). The electronic thermal conductivity can be determined by the Wiedmann-France law, $\kappa_e = L_0 \sigma T$ where $L_0 = 2.45 \times 10^{-8} \text{ V}^2 \text{ K}^{-8}$ is the Lorentz constant, T is the absolute temperature, and σ is the electrical conductivity. Attempt to reduce electronic thermal conductivity adversely affect the electrical conductivity of the materials. So, to reduce the thermal conductivity, it is desirable to reduce the lattice contribution (κ_l). Lattice thermal conductivity is reduced by the increased phonon scattering. Defects formed in a lattice act as the phonon scattering centres. Dual doping will create more lattice distortions or defects in the host lattice than the single doped ZnO. $17 \text{ W m}^{-1} \text{ K}^{-1}$ is the thermal

conductivity obtained when doping with Ni in ZnO¹³. The thermal conductivity of 9.2 W m⁻¹ K⁻¹, and 6.88 W m⁻¹ K⁻¹, were obtained for the Ni co-doped with Al in ZnO^{35, 36}. Rare earth element doping leads to more defects and reduces the total thermal conductivity of ZnO materials. A. Paulson et al. reported a thermal conductivity of 2 W m⁻¹ K⁻¹ in Dy doped ZnO⁹.

The thermal conductivity of doped and undoped samples with temperature is depicted in Fig 4.10. It is observed that the thermal conductivity decreases with doping concentration. 17.8 W m⁻¹ K⁻¹, 10 W m⁻¹ K⁻¹, 6.6 W m⁻¹ K⁻¹, and 3.7 W m⁻¹ K⁻¹ are the thermal conductivity values of pure ZnO, and doped samples respectively. The drastic reduction in thermal conductivity is ascribed to the increase in phonon scattering caused due to the large defects formed when doping with Ni²⁺ and heavier rare earth ion Pr³⁺ in the ZnO lattice. Since the ionic radii of praseodymium (1.013 Å⁰) is large than that of Zn²⁺ (0.74 Å), the inclusion of Pr³⁺ ion together with nickel (0.69 Å) creates more phonon scattering centres⁹. Enhanced phonon scattering decreases the phonon mean free path leading to a reduction in the thermal conductivity. Similarly, the difference in electronegativity of the dopants with the host lattice (Ni²⁺=1.91, Pr³⁺=1.13, Zn²⁺=1.65) enhances the phonon scattering³⁷. The thermal conductivity of the samples is independent at high temperatures. It may be due to the increase of temperature-independent phonon-impurity scattering caused due to the inclusion of praseodymium and nickel³⁸.

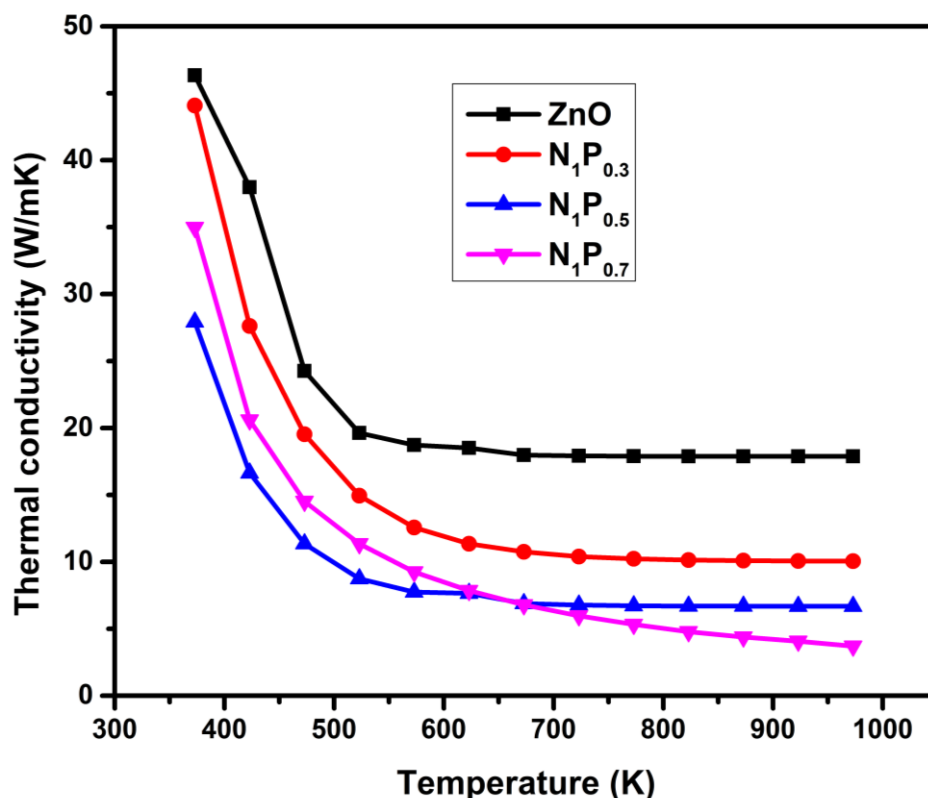


Fig 4.10 Thermal conductivity of undoped and doped samples

4.3.4.5 Figure of merit

The thermoelectric conversion efficiency is represented by the dimensionless quantity figure of merit. The temperature-dependent figure of merit of Pr and Ni doped ZnO samples is shown in Fig 4.11. The addition of the dopants into the ZnO lattice leads to a marked increase in the figure of merit. The increase in the figure of merit of doped samples arises from the large power factor and very low thermal conductivity compared to pristine ZnO. Due to its enhanced Seebeck coefficient and extremely low thermal conductivity, sample Ni₁Pr_{0.7} exhibits a higher figure of merit, more than three times greater than that of pure ZnO. This implies that introduction of rare-earth element praseodymium and nickel will improve the electrical characteristics and suppress the thermal conduction which is highly beneficial for the thermoelectric energy conversion.

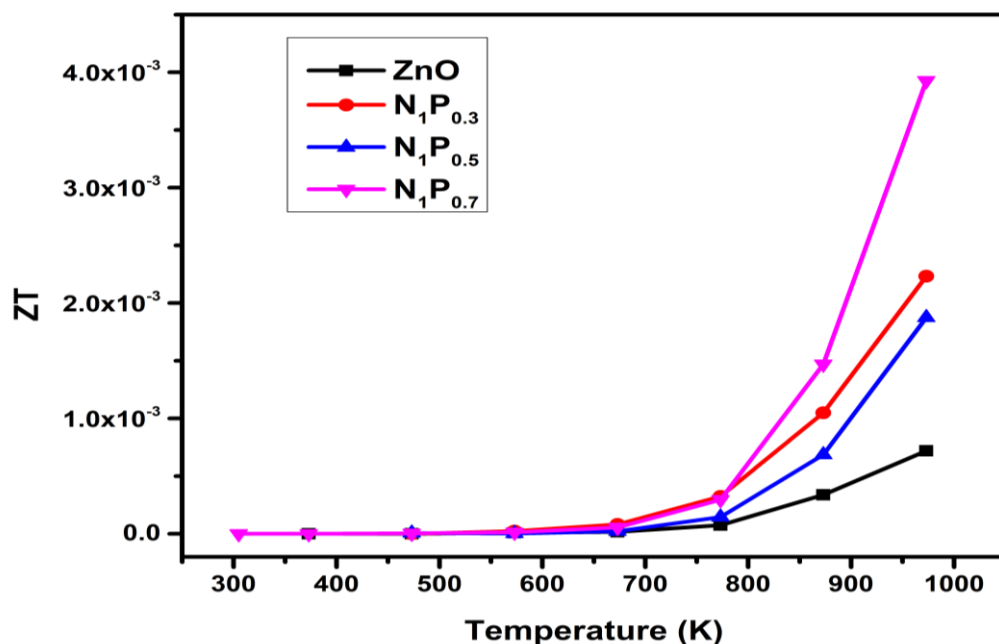


Fig 4.11 Figure of merit of undoped and doped samples

4.4 Conclusion

Nickel and praseodymium codoped ZnO ceramics were synthesised via the solid-state reaction method. The XRD patterns and FESEM-EDAX analysis confirmed the substitution of nickel and praseodymium in the host lattice. UV-Visible spectroscopic analysis shows the narrowing of optical band gap energy due to the formation of lattice defects and the electron-impurity interaction that occurred during doping. Electrical conductivity is increased due to the increment in the carrier concentration. The energy filtering effect is responsible for the large increase in the Seebeck coefficient of doped samples. Simultaneous enhancement of electrical conductivity and Seebeck coefficient in doped materials lead to an increase in power factor. The inclusion of nickel and ion with large radii causes large lattice distortions and thereby increases phonon scattering which causes a reduction in thermal conductivity. An increase in power factor and low thermal conductivity results in an improved figure of merit, almost three times increment in the figure of merit observed in the codoped samples. This confirms that the nickel and praseodymium codoping enhanced the thermoelectric performance of the ZnO crystal matrix.

References

1. H. S. Kim, W. Liu and Z. Ren, *Energy & Environmental Science* **10** (1), 69-85 (2017).
2. B. Lee, H. Cho, K. T. Park, J.-S. Kim, M. Park, H. Kim, Y. Hong and S. Chung, *Nature communications* **11** (1), 5948 (2020).
3. H. Goldsmid, *Journal of electronic materials* **42** (7), 1482-1489 (2013).
4. A. M. Dehkordi, M. Zebarjadi, J. He and T. M. Tritt, *Materials Science and Engineering: R: Reports* **97**, 1-22 (2015).
5. R. Hanus, M. T. Agne, A. J. Rettie, Z. Chen, G. Tan, D. Y. Chung, M. G. Kanatzidis, Y. Pei, P. W. Voorhees and G. J. Snyder, *Advanced Materials* **31** (21), 1900108 (2019).
6. K. Fuda and S. Sugiyama, *MRS Online Proceedings Library* **886** (1), 1-6 (2005).
7. M. Leena and S. Srinivasan, *Materials Letters* **219**, 220-224 (2018).
8. J.-H. Lin, C.-S. Hwang and F.-R. Sie, *Materials Research Bulletin* **122**, 110650 (2020).
9. A. Paulson, N. M. Sabeer and P. Pradyumnan, *Journal of Alloys and Compounds* **786**, 581-587 (2019).
10. J. Liu, C. Wang, Y. Li, W. Su, Y. Zhu, J. Li and L. Mei, *Journal of Applied Physics* **114** (22), 223714 (2013).
11. Y. Inoue, Y. Okamoto and J. Morimoto, *Journal of materials science* **43** (1), 368-377 (2008).
12. F. ZHANG, N. Baocheng, K. ZHANG, X. ZHANG, L. Qingmei and J. ZHANG, *Journal of Rare Earths* **31** (9), 885-890 (2013).
13. H. Colder, E. Guilmeau, C. Harnois, S. Marinel, R. Retoux and E. Savary, *Journal of the European Ceramic Society* **31** (15), 2957-2963 (2011).
14. R. S. Bose and A. Nag, *Journal of Physics D: Applied Physics* **54** (37), 375502 (2021).
15. J. Hoemke, A. U. Khan, H. Yoshida, T. Mori, E. Tochigi, N. Shibata, Y. Ikuhara and Y. Sakka, *Journal of the Ceramic Society of Japan* **124** (5), 515-522 (2016).
16. K. Kumar, R. Thomas, S. Valanarasu, V. Ganesh, M. Shkir, S. AlFaify and J. Thirumalai, *Applied Physics A* **125** (10), 1-12 (2019).
17. J.-L. Chen, N. Devi, N. Li, D.-J. Fu and X.-W. Ke, *Chinese Physics B* **27** (8), 086102 (2018).
18. T. Kamal, M. Chowdhury, M. Zubair and S. Al Mamun, presented at the 2018 4th International Conference on Electrical Engineering and Information & Communication Technology (iCEEICT), 2018 (unpublished).

19. S. Aksoy, Y. Caglar, S. Ilican and M. Caglar, *Optica Applicata* **40** (1), 7-14 (2010).
20. A. Jain, P. Sagar and R. Mehra, *Solid-State Electronics* **50** (7-8), 1420-1424 (2006).
21. G. Xie, L. Fanga, L. Peng, G. Liu, H. Ruan, F. Wu and C. Kong, *Physics Procedia* **32**, 651-657 (2012).
22. H. Çolak and H. İ. Mercan, *Journal of Materials Science: Materials in Electronics*, 1-13 (2022).
23. S. C. Das, R. J. Green, J. Podder, T. Z. Regier, G. S. Chang and A. Moewes, *The Journal of Physical Chemistry C* **117** (24), 12745-12753 (2013).
24. L. L. Chen, H. D. Hu and Z. H. Xiong, presented at the Advanced Materials Research, 2013 (unpublished).
25. J. Han, M. Shen, W. Cao, A. Senos and P. Mantas, *Applied Physics Letters* **82** (1), 67-69 (2003).
26. U. Godavarti, V. Mote and M. Dasari, *Journal of Asian Ceramic Societies* **5** (4), 391-396 (2017).
27. K. Barmak and K. Coffey, *Metallic films for electronic, optical and magnetic applications: Structure, processing and properties*. (Woodhead Publishing, 2014).
28. E. Hendry, M. Koeberg, J. Pijpers and M. Bonn, *Physical Review B* **75** (23), 233202 (2007).
29. M. Koopmans, M. A. Leiviskä, J. Liu, J. Dong, L. Qiu, J. C. Hummelen, G. Portale, M. C. Heiber and L. J. A. Koster, *ACS applied materials & interfaces* **12** (50), 56222-56230 (2020).
30. A. Yildiz, B. Kayhan, B. Yurduguzel, A. Rambu, F. Iacomi and S. Simon, *Journal of Materials Science: Materials in Electronics* **22** (9), 1473-1478 (2011).
31. X. Guan and J. Ouyang, *CCS Chemistry* **3** (10), 2415-2427 (2021).
32. C. Gayner and Y. Amouyal, *Advanced Functional Materials* **30** (18), 1901789 (2020).
33. P. Shyni and P. Pradyumnan, *ECS Journal of Solid State Science and Technology* **10** (7), 071017 (2021).
34. P. Shyni and P. Pradyumnan, *RSC Advances* **11** (8), 4539-4546 (2021).
35. H. Yamaguchi, Y. Chonan, M. Oda, T. Komiyama, T. Aoyama and S. Sugiyama, *Journal of electronic materials* **40** (5), 723-727 (2011).
36. D.-B. Zhang, B.-P. Zhang, D.-S. Ye, Y.-C. Liu and S. Li, *Journal of Alloys and Compounds* **656**, 784-792 (2016).
37. C. Gayner, *Chemical Engineering Journal* **413**, 128149 (2021).
38. H. Muta, K. Kurosaki and S. Yamanaka, *Journal of Alloys and Compounds* **350** (1-2), 292-295 (2003).

Chapter 5

Effects of Ni-Cu dual doping on the thermoelectric properties of ZnO

This chapter emphasizes the impact of dual doping of transition metals on the thermoelectric properties of ZnO. Nickel and copper inclusion increases the charge carrier density causing an increment in electrical conductivity, and induces more crystal defects in the host structure to suppress the thermal conductivity. Large thermopower and increased electrical conductivity together with minimized thermal conductivity lead to improvement in the figure of merit.

5.1 Introduction

Thermoelectricity is the most dependable renewable energy source as heat energy is available everywhere and an enormous amount of heat energy is expelled from every energy-producing system. Thermoelectric materials can effectively harvest this waste heat and convert it into useful electrical energy. For effective waste heat recovery, thermoelectric materials should possess high transport properties and minimal thermal conduction. Since it is difficult to increase electrical transport and reduce thermal conduction simultaneously, we have to adopt many approaches such as band structure modification through doping, nanostructuring etc. Such methods will reduce the thermal conductivity by increasing the phonon scattering and enhancing the electrical conductivity of the materials.¹⁻⁵.

The improvement in power factor is achieved through the simultaneous enhancement in both electrical conductivity and the Seebeck coefficient via the energy filtering effect. A material with high carrier density will have high electrical conductivity, and if this material has the capability to filter out the low energy carriers through the effect of energy filtering, we can achieve a high Seebeck coefficient without much reduction in electrical conductivity. There are many reports on the enhancement of thermoelectric power factors through energy filtering. A.T.T. Pham et.al. reported a power factor of 100-200 $\mu\text{W}/\text{mK}^2$ in Mg doped ZnO films⁶. A power factor of 313 $\mu\text{W}/\text{mK}^2$ was obtained for Ga doped ZnO and Ni, Al doped ZnO multilayer films⁷.

This chapter deals with the effect of simultaneous doping of transition metals - nickel and copper, on the thermoelectric properties of ZnO. Dual doping creates more lattice imperfections and hence reduces the thermal conductivity of the parent lattice. Moreover, it is effective to customise the position and occupancy of the Fermi level⁸. Investigations show that transition metal doping enhances the thermoelectric properties of ZnO either as a single dopant or as a co-dopant⁹⁻¹¹. Ni doped ZnO shows enhancement in the thermoelectric properties and decrement in the optical band gap energy. As a codopant with Al, Ni substituted ZnO possesses a power factor of $6.16 \times 10^{-4} \text{ W}/\text{mK}^2$ ¹²⁻¹⁵. Since nickel and copper have comparable

sizes to that of ZnO, these metals possess higher solubility in the ZnO crystal structure.

5.2 Experimental method

$Zn_{(1-x-y)} Ni_x Cu_y O$ ($x = 0.01, 0.02$ $y = 0.01, 0.02$) materials were prepared through the solid-state reaction method. Powders of zinc oxide, nickel oxide, and copper oxide (purity 99.99%) were weighed according to stoichiometric ratio, mixed and ground for 1 hour, and then calcinated at $450^\circ C$ for 4 hours. The calcinated powder mixture was again ground for 1 hour and then pelletized for densification with a force of 10 Ton. The densified pellets were sintered at $1300^\circ C$ for 4 hours. The sintered sample in powder and pellet form was used for characterizations. The doped samples are denoted as N1C1 ($Zn_{0.98} Ni_{0.01} Cu_{0.01} O$), N1C2 ($Zn_{0.97} Ni_{0.01} Cu_{0.02} O$), and N2C1 ($Zn_{0.97} Ni_{0.02} Cu_{0.01} O$)

5.3 Results and discussions

5.3.1. Structural characterization

Microstructure analysis of the prepared materials was carried out with the X-ray diffraction method between the Bragg angle of 20° - 80° . All the peaks of the doped samples were indexed according to the ICSD card No: 29272 and no characteristic peaks of nickel and copper were observed. The materials were belonging to the space group P63mc and the XRD pattern of each doped sample confirmed the hexagonal wurtzite structure of ZnO as shown in Fig 5.1 indicating the perfect inclusion of dopants into the ZnO lattice. The dual doping of nickel and copper (ionic radii of $Ni^{2+} = 0.69 \text{ \AA}$ and $Cu^{2+} = 0.73 \text{ \AA}$) into the ZnO lattice may lead to the formation of defects which will affect the crystallinity of the lattice and it is observed as the intensity reduction in the XRD pattern. The sample N2C1 has the lowest intensity, indicating more lattice imperfections. As the doping concentration increased, the most intense peak (101) shifted to a lower and higher angle as depicted in Fig 5.2. The higher angle peak shift is attributed to the decrease in lattice parameters and thereby contraction of the lattice. The lower angle peak shift indicates the presence of increased strain, leading to the lattice expansion^{1, 16}. The

substitution of dopant ions will create defects and charge imbalance in the lattice ¹⁷. The ionic radii of Ni²⁺ and Cu²⁺ are smaller than Zn²⁺ ions (Zn²⁺=0.74 Å), therefore, most of the dopants will be occupied in the interstitial sites other than the vacancy sites that lead to very slight variation in lattice parameters. This will maintain the hexagonal wurtzite structure in the doped samples. The variation of lattice parameters with dopant concentrations is summarised in Table 5.1.

The variation in crystallite size and microstrain developed in the lattice substantiate the inclusion of dopants in the host lattice. The crystallite size and strain estimated from the W-H plot using the W-H equation are given in Table 5.2. The crystallite size decreases with an increase in dopant concentration. The decrease in crystallite size is due to the inhibition of nucleation, thereby reducing the microcrystals' growth upon doping ¹⁷. The negative strain indicates the compressive nature of the lattice and the doping increases the strain in the lattice. The N1C2 material has a high strain value due to the incorporation of more copper atoms, which have a larger ionic radius than the nickel atom.

Table 5.1 Lattice constants of ZnO and doped ZnO materials

Sample	a (Å)	c(Å)	c/a
ZnO	3.254	5.216	1.6029
N1C1	3.259	5.226	1.6035
N1C2	3.258	5.223	1.6031
N2C1	3.254	5.205	1.5995

Table 5.2 Crystallite size and microstrain calculated from W-H plot

Sample	Crystallite size (nm)	Strain ϵ (10^{-4})
ZnO	59.25±0.0004	-0.2540
N1C1	52.32±0.0001	-1.8084
N1C2	53.32±0.0002	-7.6608
N2C1	48.14±0.0004	-2.1976

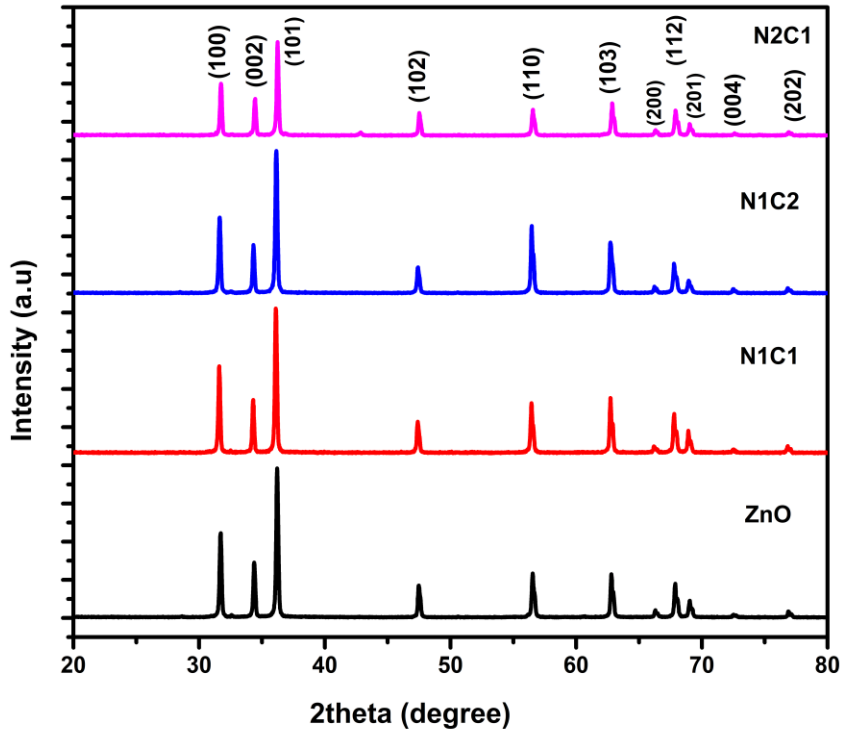


Fig 5.1 XRD pattern of the undoped and doped samples

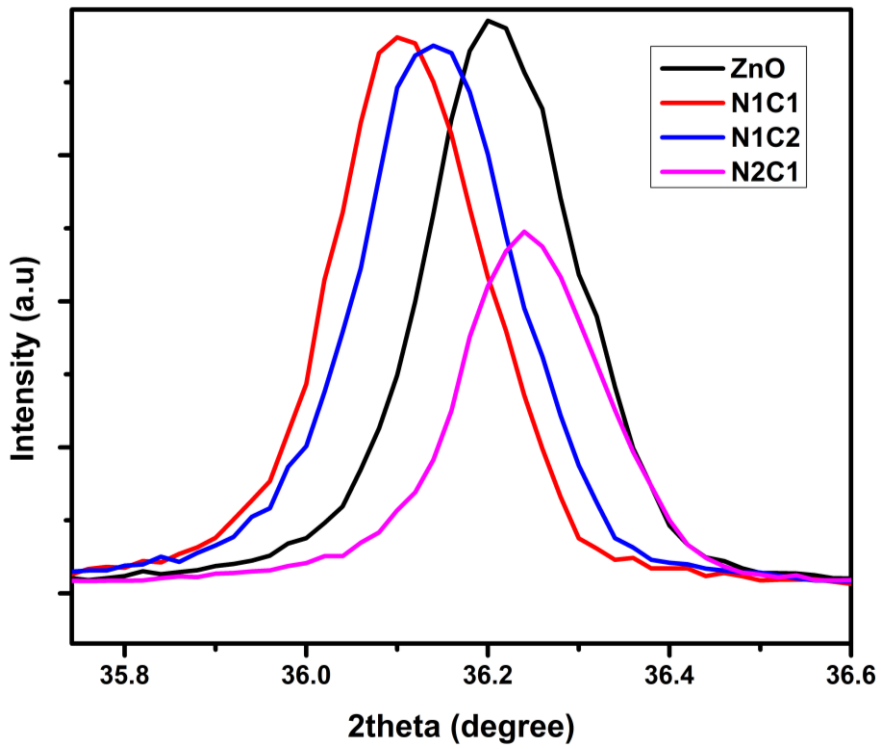


Fig 5.2 Peak shift of (101) plane

5.3.2 FESEM and EDAX analysis

The morphology of the undoped dual doped samples was investigated by the Field Emission Scanning electron microscopic analysis. The FESEM images of the samples are shown in Fig 5.3. Stripes formed on the surface show the growth of planes and stacks on the surface. The homogeneous distribution of grains and the presence of hexagonal-like grains can be identified. The morphology of the samples doped with a higher concentration of nickel and copper varies significantly. The EDAX analysis of the dual doped samples confirms the presence of dopants Ni and Cu in the synthesised materials and the spectrum is depicted in Fig 5.4.

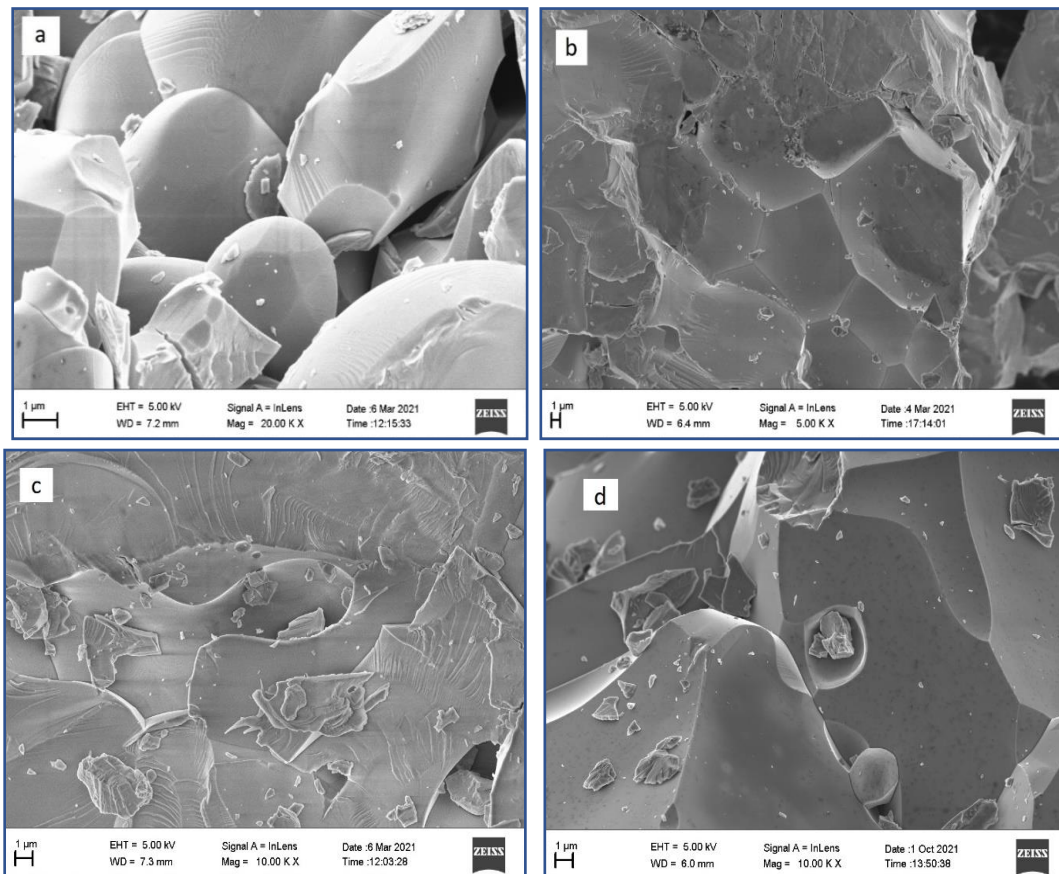


Fig 5.3 FESEM images of (a) ZnO (b) N1C1 (c) N1C2 (d) N2C1

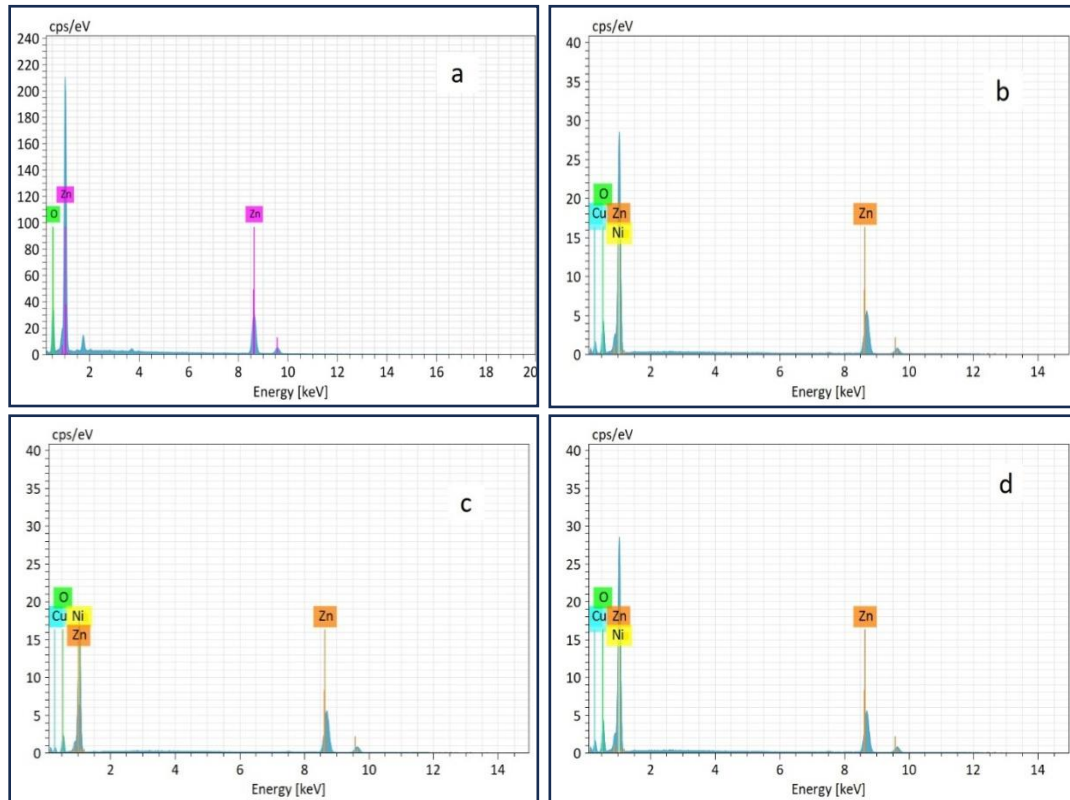


Fig 5.4 EDAX spectrum of (a) ZnO (b) N1C1 (c) N1C2 (d) N2C1

5.3.3 UV-Vis spectroscopic analysis

The absorption spectra of the doped materials show strong absorption in the ultraviolet region and low absorption in the visible region. The optical band gap energy of semiconducting materials with a direct band gap is estimated from the Tauc's relation.

The band gap energy of doped semiconductors is greatly influenced by many-body interactions, grain size, structural deformation, strain etc. The transition metals dual doping enhances the optical properties of ZnO due to the occupancy and position of the Fermi level¹⁸. The reports show that the presence of a small amount of nickel or copper as a single dopant leads to a strong band gap reduction in ZnO^{19, 20}. The optical band gap energies of all the doped samples were lower than the pristine ZnO as presented in Fig 5.5, which is in agreement with the redshift observed in the absorption edge of the doped materials. The decrease in band gap arises mainly due to the presence of defects formed due to the dual substitution of metal ions into the

ZnO lattice and the sp-d exchange interaction between the dopants and the host atom. Furthermore, as a result of doping, impurity band formation and many body effects occurs which may cause a raising of the valance band and lowering of conduction bands resulting in reduced optical band gap energy^{21, 22}. The decrease in band gap energy of transition metal doped ZnO is reported by several investigators^{18, 19, 23, 24}.

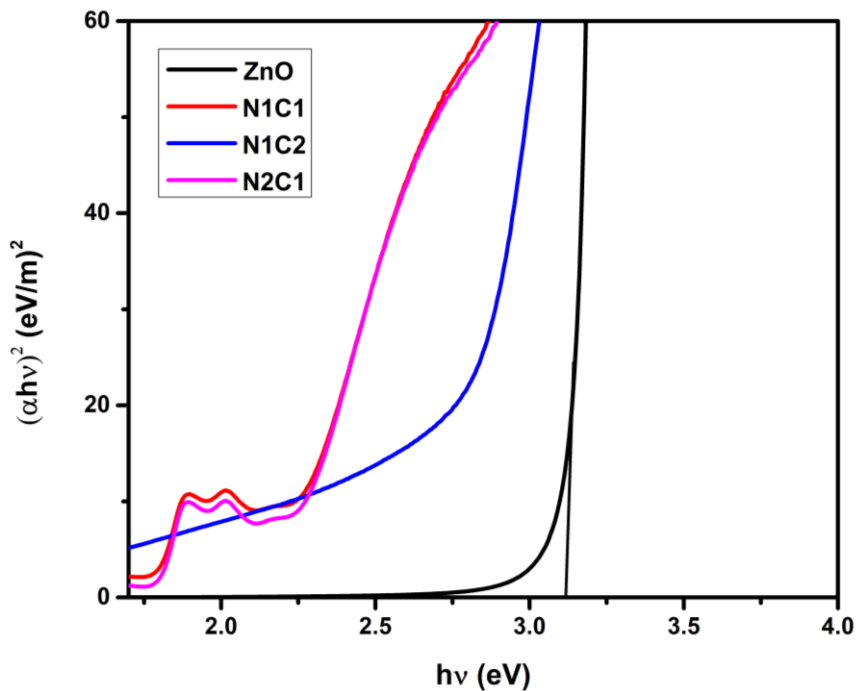


Fig 5.5 Optical band gap energy of doped and undoped samples

5.3.4 Thermoelectric studies

5.3.4.1 Electrical conductivity

The plot of the variation of electrical conductivity with temperature confirms the semiconducting nature of pure ZnO and doped samples. All the dual substituted materials possess high electrical conductivity than pristine ZnO as shown in Fig 5.6. In a doped semiconductor, low electrical conductivity in the low-temperature region is due to the recapturing of free electrons supplied by the dopant atoms. As a result, electron hopping dominates over free electron band conduction^{25, 26}. When the temperature increases, the electrical conductivity increases because of the bipolar conduction mechanism from the valance band to the conduction band.

The inclusion of Ni and Cu will induce more electrons to the host lattice which increases the charge carrier density of the doped samples. An increment in carrier concentration increases the electrical conductivity according to the relation $\sigma = ne\mu$, where n , e , μ are the carrier concentration, electron charge and mobility of charge carriers respectively. Ni^{2+} and Cu^{2+} doping increases the carrier concentration. $6.20 \times 10^{19} \text{ m}^{-3}$, $2.7 \times 10^{20} \text{ m}^{-3}$, $8.25 \times 10^{20} \text{ m}^{-3}$ and $4.227 \times 10^{20} \text{ m}^{-3}$ are the carrier concentration of ZnO, N1C1, N1C2 and N2C1 materials respectively, determined by the Hall measurement analysis. As the doping concentration increases, the electrical conductivity increases up to the doping concentration of N1C2 but decreases with a further increase in doping concentration. Increased addition of Ni^{2+} and Cu^{2+} ions induce defects scattering centres in the host lattice, which will cause trapping of free electrons donated by the dopants. This will reduce the free electron contribution to the electrical conductivity. The carrier mobility may decrease with an increase in carrier concentration due to the increase in degeneracy and scattering of carriers²⁷.

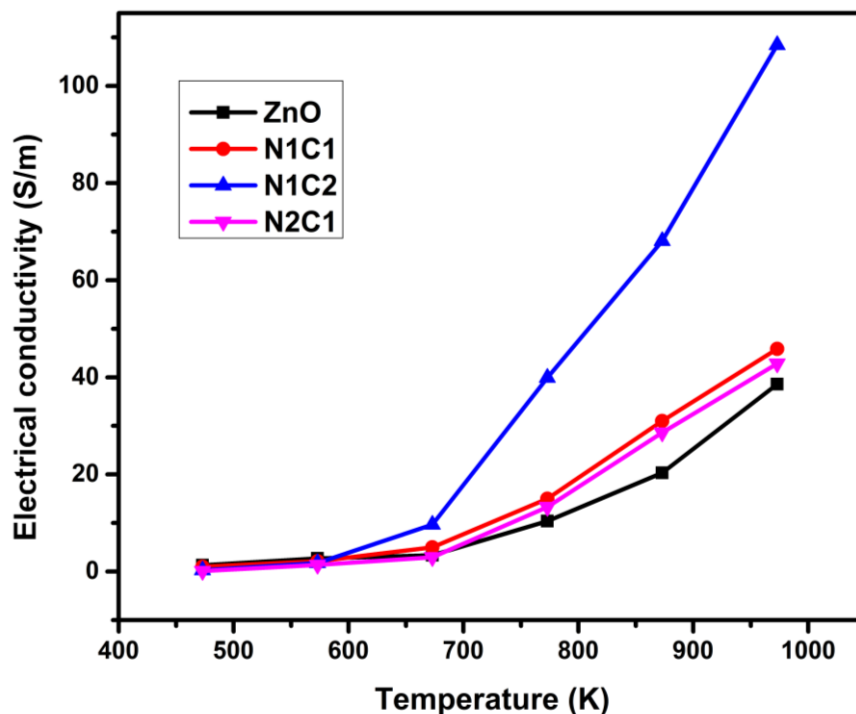


Fig 5.6 Variation of electrical conductivity of samples with temperature

5.3.4.2 Seebeck coefficient

Variations of the Seebeck coefficient of the prepared materials as a function of temperature are shown in Fig 5.7. The negative Seebeck coefficient indicates that the majority of charge carriers are electrons and the materials are n-type. All the prepared materials have a higher Seebeck coefficient than the undoped ZnO. The doped samples exhibit a higher Seebeck coefficient in the low temperature region, then decrease at higher temperatures. The decreasing nature of the Seebeck coefficient with temperature is explained based on the bipolar effect, dominated at high temperatures, resulting in the cancellation of the Seebeck coefficient of holes and electrons^{28, 29}. Among the doped samples, the N1C1 sample has the highest Seebeck coefficient of 1318 $\mu\text{V/K}$. This is greater than the Seebeck coefficient obtained for copper and nickel singly doped ZnO^{12, 30}.

Large effective mass and electron-electron interactions are responsible for the higher Seebeck coefficient in the samples. The Seebeck coefficient of bulk semiconducting oxides can be related to the effective mass and carrier concentration through Mott's relation. The higher Seebeck coefficient of samples N1C1 and N2C1 are the manifestation of low charge carrier concentration. Since the doped materials possess a very large Seebeck coefficient, the density-of-state (DOS) effective mass (m_d^*) of pristine and doped ZnO materials is estimated at 300K using equation (5.1) connecting the Seebeck coefficient and carrier density of the synthesised materials³¹.

$$\log_{10} \left(\frac{m_d^*}{300} T \right) = \frac{2}{3} \log_{10}(n) - \frac{2}{3} [20.3 - (0.00508 \times |S|) + (1.58 \times 0.967^{|S|})] \quad (5.1)$$

The calculated m_d^* (m_e) is listed in Table 5.3. The density-of-state effective mass shows an increase from 0.24 m_e to 1.35 m_e with an increase in nickel and copper doping concentrations. The hike in the Seebeck coefficient observed in the doped materials is attributed to the large increase in the density-of-state-effective mass caused during dual doping. The electronic band structure of the host material is highly modified through doping which creates more density of states and thereby

increment in density-of-states effective mass which resulted from the tuning of Fermi level in the valance band^{32, 33}. The excess charge scattering centres created in the lattice upon dual doping scatter the induced carriers also caused to increase in the Seebeck coefficient of doped materials³⁴. Although both the increased scattering and effective mass increase the Seebeck coefficient, it is responsible for the diminishing of electrical conductivity by decreasing carrier mobility even if the carrier concentration of ZnO increases when doping with Ni²⁺ and Cu²⁺ ions.

Seebeck coefficient strongly depends on Fermi level shift. Enhanced Seebeck coefficient can be attained by tuning the E_F of the materials in the vicinity of E_C . According to the Fritsche model connecting the Seebeck coefficient, the energy difference between the conduction band and Fermi level, the Seebeck coefficient of n-type semiconductor can be expressed as,

$$S = \frac{-k_B}{e} \left\{ \frac{E_C - E_F}{k_B T} + A_C \right\} \quad (5.2)$$

where A_C is a temperature independent constant related to the carriers distributed above the conduction band E_C . The sign of the Seebeck coefficient is relies on whether the conduction mechanism occurs above or below the Fermi level³⁵. The Fermi level energy measured from the conduction band edge is shown in Table 5.3. $E_C - E_F$ of both the doped and undoped samples are negative, indicating that the Fermi level shifts above the conduction band and the materials become degenerate.

Table 5.3 Fermi-level shift and DOS effective mass of the prepared materials

Sample	$E_C - E_F$ (eV)	Effective mass m_d^* (m_e)
ZnO	-0.05319±0.002	0.2407
N1C1	-0.40135±0.069	0.6419
N1C2	-0.31953±0.013	1.358
N2C1	-0.34975±0.031	0.8657

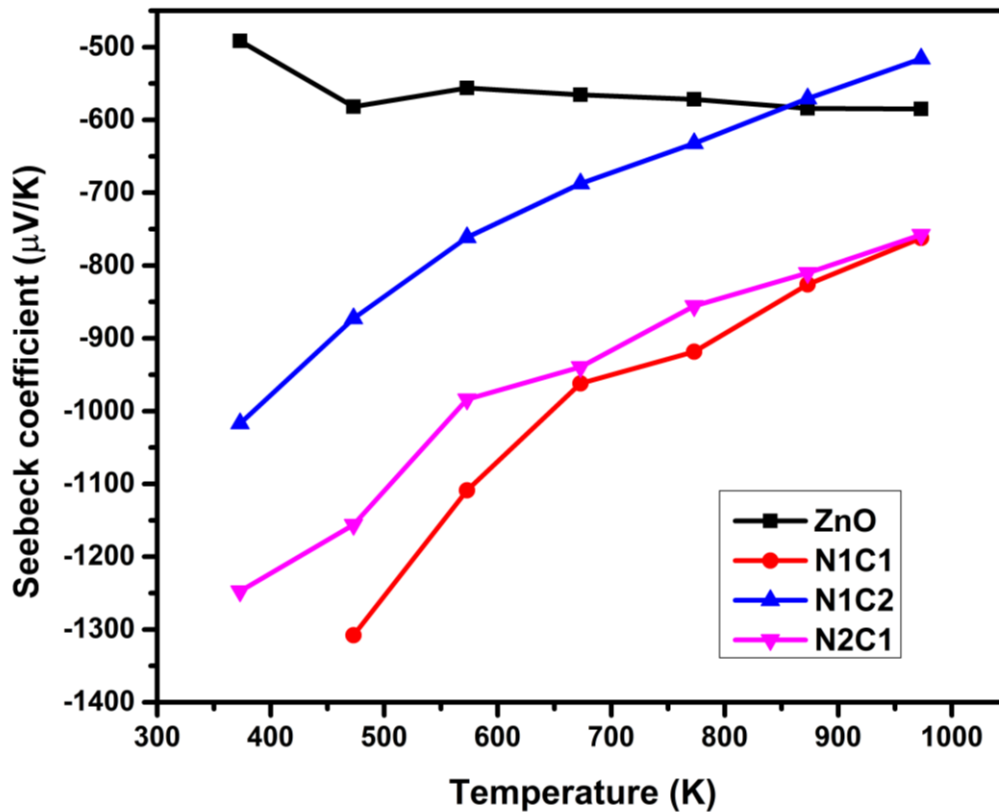


Fig 5.7 Variation of Seebeck coefficient with temperature

5.3.4.3 Power factor

The power factor represents the electrical contribution to the thermoelectric performance and is estimated from the electrical conductivity and Seebeck coefficient. The temperature dependent thermoelectric power factor of doped and undoped materials are given in Fig 5.8. Owing to the large Seebeck coefficient, all the doped samples exhibit a higher power factor than the host ZnO. The power factor values increased with an increase in copper doping concentration but decreases with nickel concentration.

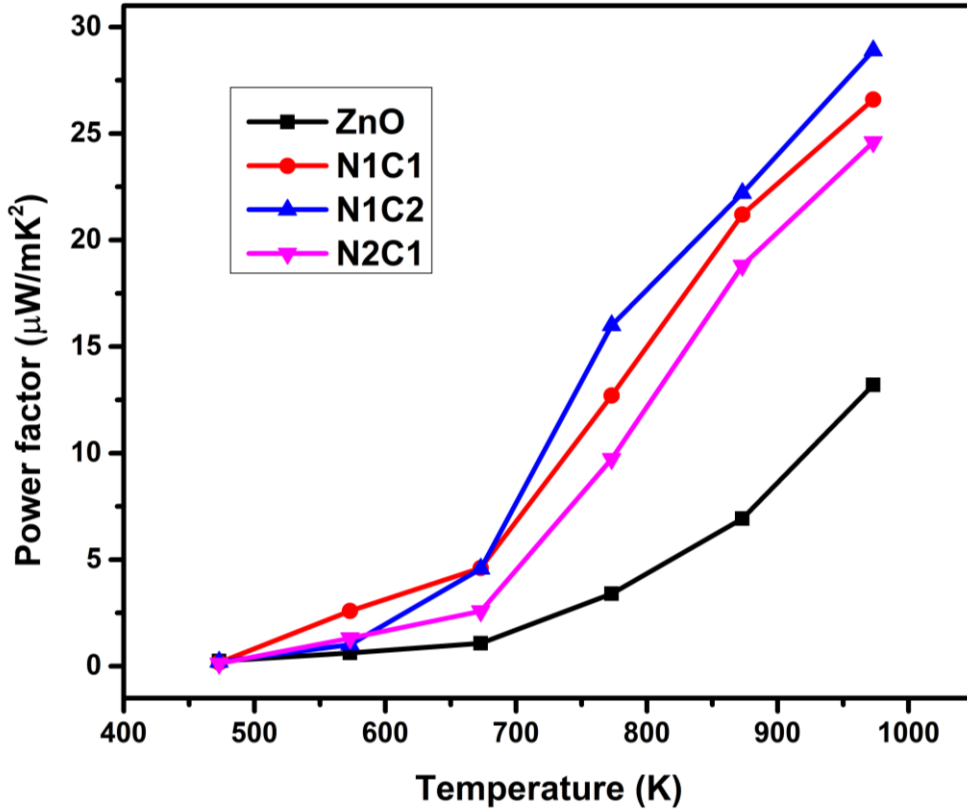


Fig 5.8 Variation of power factor of the samples with temperature

5.3.4.4 Thermal conductivity

The total thermal conductivity (κ) in solids is the sum of lattice (κ_l) and electronic (κ_e) thermal conductivities. The electronic thermal conductivity can be estimated by the Wiedmann-Franz law, $\kappa_e = L\sigma T$ where $L = 2.45 \times 10^{-8} \text{ V}^2 \text{ K}^{-8}$ is the Lorentz constant, T is the absolute temperature, and σ is the electrical conductivity. But estimating electronic thermal conductivity with Lorentz constant of $2.45 \times 10^{-8} \text{ V}^2 \text{ K}^{-8}$ leads to huge error as it is valid only for highly degenerate materials with Seebeck coefficient less than $50 \text{ } \mu\text{V/K}$. For materials with very high Seebeck coefficient, an equation to determine L in terms of measured Seebeck coefficient is proposed³⁶ as,

$$L = 1.5 + \exp\left[-\frac{|S|}{116}\right] \quad (5.3)$$

Since electronic thermal conductivity is contributed by electrons, a reduction in electronic thermal conductivity will affect the electrical conductivity of the

materials. For ZnO ceramics, the main contribution to the total thermal conductivity is from the phonons. So, low thermal conductivity can be achieved by reducing the lattice part by introducing phonon scattering centres in the host lattice. Doping will induce lattice imperfections that act as phonon scattering centres^{37, 38}. The Ni and Cu dual substitution will create more defects in the host lattice. The heat-carrying phonons with different mean free paths will scatter when colliding with the defects, leading to low thermal conductivity. The lattice thermal conductivity and total thermal conductivity are depicted in Fig 5.9 and Fig 5.10. From the figures, it can be inferred that the decrease in total thermal conductivity is mainly due to the reduction of the lattice thermal conductivity and it is less dependent on the electronic thermal transport. The pure ZnO has a thermal conductivity of 17 W/mK which is reduced to 8.36 W/mK up on dual doping. The difference in electronegativity ($\text{Ni}^{2+}=1.91$, $\text{Cu}^{2+}=1.9$, $\text{Zn}^{2+}=1.65$) also minimizes the phonon mean free path and thereby the lattice thermal transport³⁹. The thermal conductivity is independent of temperature variations, mainly due to the increment in the temperature independent phonon-impurity scattering, which occurred upon dual substitution⁴⁰.

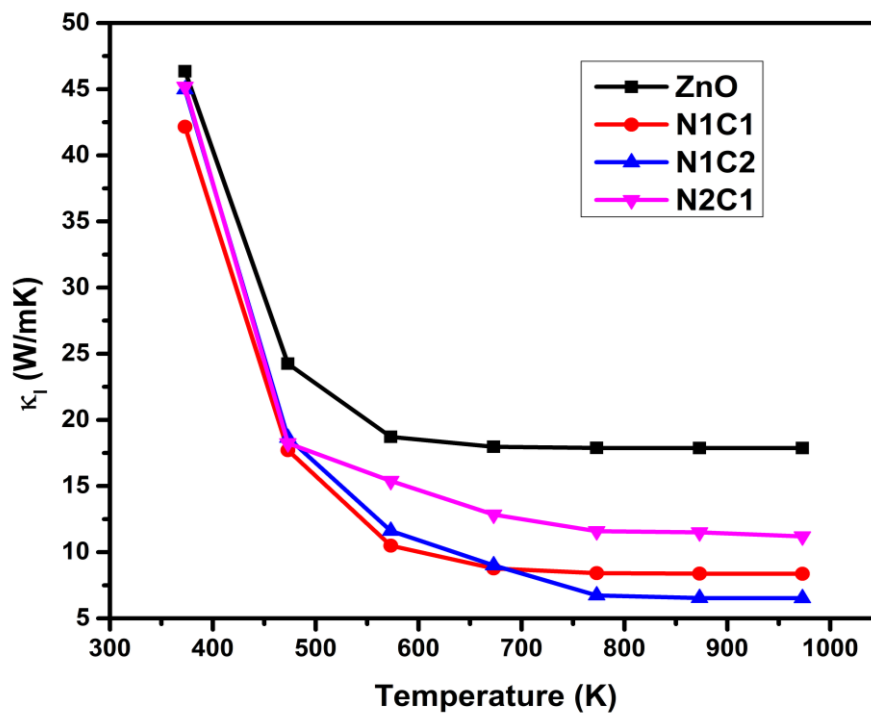


Fig. 5.9 Variation of lattice thermal conductivity of the samples with temperature

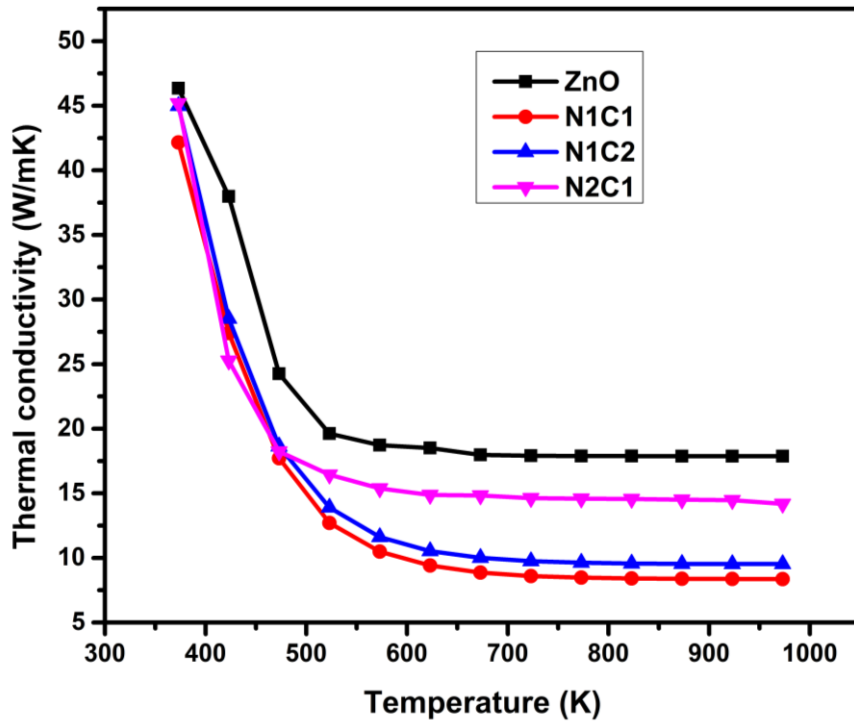


Fig 5.10 Variation of total thermal conductivity of the samples with temperature

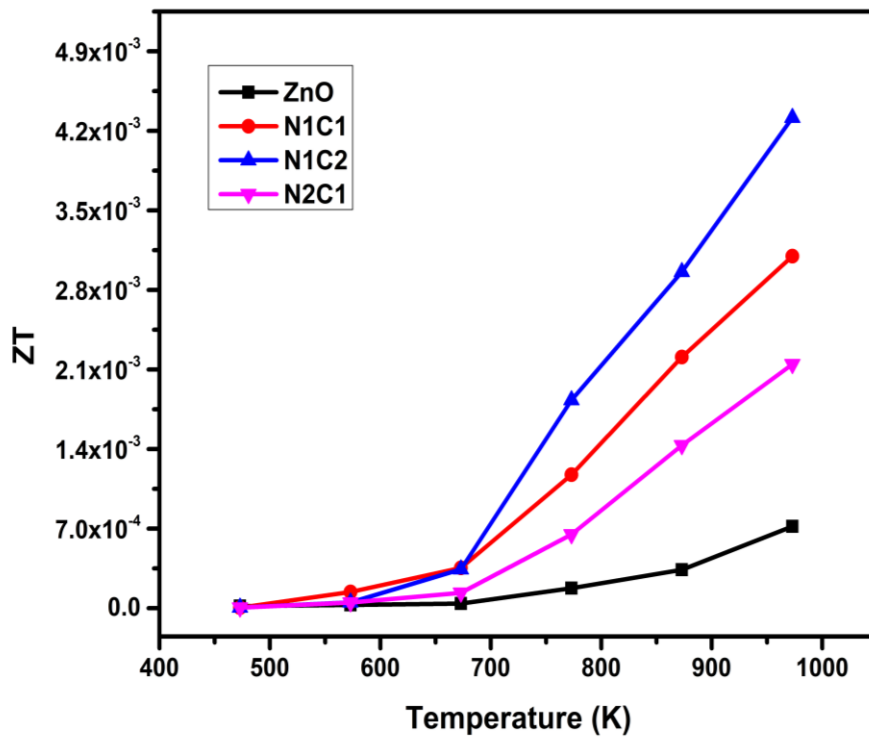


Fig 5.11 Variation of figure of merit of the samples with temperature

5.3.4.5 Figure of merit

The thermoelectric figure of merit is determined from the power factor and thermal conductivity of the prepared materials. The effect of enhanced power factor and suppressed thermal conductivity are greatly reflected in the figure of merit of nickel and copper doped ZnO. Among the prepared materials, N1C2 has the improved efficiency because of its high power factor and low thermal conductivity. A sixfold improvement in the figure of merit is obtained in the dual doped ZnO materials at 973K as shown in Fig 5.11.

5.4 Conclusion

The inclusion of nickel and copper in the host lattice was confirmed by the structural and morphological analysis. All the prepared samples resemble the hexagonal wurtzite structure of ZnO and significant variations in surface morphology were observed. The absorption edge shows a redshift and the optical band gap energy is reduced from 3.1 eV to 2.15 eV. Both the electrical conductivity and Seebeck coefficient were enhanced due to the dual substitution of donor atoms. Dual substitution leads to the highest Seebeck coefficient of $\sim 1318 \mu\text{V/K}$ and thermal conductivity is reduced to 8.3 W/mK as a result of the increased phonon scattering. Power factor enhancement and thermal conductivity reduction resulted in a six-fold increase in the figure of merit of the prepared materials. Since all the Ni and Cu doped ZnO materials possess enhanced thermoelectric properties than pristine ZnO, these materials are suitable for thermoelectric applications.

References

1. A. Paulson, N. M. Sabeer and P. Pradyumnan, *Journal of Alloys and Compounds* **786**, 581-587 (2019).
2. N. M. Sabeer, A. Paulson and P. Pradyumnan, *Journal of Applied Physics* **124** (18), 185107 (2018).
3. T. Ramachandran, N. Rajeevan and P. Pradyumnan, *Modern Physics Letters B* **28** (05), 1450034 (2014).
4. T. Ramachandran, R. NE and P. PP, *Materials Sciences and Applications* **2013** (2013).
5. N. M. Sabeer, A. Paulson and P. Pradyumnan, *Journal of Physics and Chemistry of Solids* **138**, 109294 (2020).
6. A. T. T. Pham, P. T. N. Vo, H. K. T. Ta, H. T. Lai, V. C. Tran, T. L. H. Doan, A. T. Duong, C.-T. Lee, P. Nair and Y. A. Zulueta, *Thin Solid Films* **721**, 138537 (2021).
7. Z. Zhou, Y. Zheng, Y. Yang, W. Zhang, M. Zou, C.-W. Nan and Y.-H. Lin, *Crystals* **12** (10), 1351 (2022).
8. N. Lathiotakis, A. N. Andriotis and M. Menon, *Physical Review B* **78** (19), 193311 (2008).
9. A. Pashkevich, A. Fedotov, E. Poddenezhny, L. Bliznyuk, J. Fedotova, N. Basov, A. Kharchanka, P. Zukowski, T. Koltunowicz and O. Korolik, *Journal of Alloys and Compounds* **895**, 162621 (2022).
10. H. Yamaguchi, Y. Chonan, M. Oda, T. Komiyama, T. Aoyama and S. Sugiyama, *Journal of electronic materials* **40**, 723-727 (2011).
11. B. Zhu, C. Chen, Z. Yao, J. Chen, C. Jia, Z. Wang, R. Tian, L. Tao, F. Xue and H. Hng, *Journal of the European Ceramic Society* **41** (7), 4182-4188 (2021).
12. H. Colder, E. Guilmeau, C. Harnois, S. Marinel, R. Retoux and E. Savary, *Journal of the European Ceramic Society* **31** (15), 2957-2963 (2011).
13. D.-B. Zhang, B.-P. Zhang, D.-S. Ye, Y.-C. Liu and S. Li, *Journal of Alloys and Compounds* **656**, 784-792 (2016).
14. J. Hoemke, A. U. Khan, H. Yoshida, T. Mori, E. Tochigi, N. Shibata, Y. Ikuhara and Y. Sakka, *Journal of the Ceramic Society of Japan* **124** (5), 515-522 (2016).
15. H. Yamaguchi, Y. Chonan, M. Oda, T. Komiyama, T. Aoyama and S. Sugiyama, *Journal of electronic materials* **40** (5), 723-727 (2011).
16. C. Soumya and P. P. Pradyumnan, *International Journal of Energy Research*.
17. M. M. Hassan, W. Khan, A. Azam and A. Naqvi, *Journal of Luminescence* **145**, 160-166 (2014).

18. A. Safeen, K. Safeen, M. Shafique, Y. Iqbal, N. Ahmed, M. A. R. Khan, G. Asghar, K. Althubeiti, S. Al Otaibi and G. Ali, *RSC advances* **12** (19), 11923-11932 (2022).
19. S. C. Das, R. J. Green, J. Podder, T. Z. Regier, G. S. Chang and A. Moewes, *The Journal of Physical Chemistry C* **117** (24), 12745-12753 (2013).
20. T. Munir, A. Mahmood, N. Ahmad, M. Atif, K. Alimgeer, A. Fatehmulla, A. Hanif, N. Yaqub, W. Farooq and S. Ahmad, *Journal of King Saud University-Science* **33** (2), 101330 (2021).
21. S. Benramache, B. Benhaoua and H. Bentrah, *Journal of Nanostructure in Chemistry* **3**, 1-7 (2013).
22. D. P. Joseph and C. Venkateswaran, *Journal of Atomic and Molecular Physics* **2011** (2011).
23. D. Sharma and R. Jha, *Journal of Alloys and Compounds* **698**, 532-538 (2017).
24. D. Toloman, A. Mesaros, A. Popa, T. Silipas, S. Neamtu and G. Katona, *Journal of Materials Science: Materials in Electronics* **27** (6), 5691-5698 (2016).
25. U. Godavarti, V. Mote and M. Dasari, *Journal of Asian Ceramic Societies* **5** (4), 391-396 (2017).
26. R. Kumar and N. Khare, *Thin Solid Films* **516** (6), 1302-1307 (2008).
27. S. Wang, H. Li, R. Lu, G. Zheng and X. Tang, *Nanotechnology* **24** (28), 285702 (2013).
28. P. Shyni and P. Pradyumnan, *RSC Advances* **11** (8), 4539-4546 (2021).
29. Z. M. Gibbs, H.-S. Kim, H. Wang and G. J. Snyder, *Applied Physics Letters* **106** (2), 022112 (2015).
30. D. V. Vu, D. H. Le, T. T. Nguyen, T. Van Duong, Q. D. Ngo and T. Q. Trinh, *Journal of Materials Science: Materials in Electronics* **30** (7), 6544-6551 (2019).
31. K. H. Lee, S. i. Kim, J. C. Lim, J. Y. Cho, H. Yang and H. S. Kim, *Advanced Functional Materials* **32** (33), 2203852 (2022).
32. Y. Pei, A. D. LaLonde, H. Wang and G. J. Snyder, *Energy & Environmental Science* **5** (7), 7963-7969 (2012).
33. H. Park, S.-i. Kim, J.-Y. Kim, S.-M. Hwang and H.-S. Kim, *Ceramics* **6** (1), 504-513 (2023).
34. A. Paulson, N. M. Sabeer and P. Pradyumnan, *Materials Science and Engineering: B* **262**, 114745 (2020).
35. H. Fritzsche, *Solid State Communications* **9** (21), 1813-1815 (1971).
36. H.-S. Kim, Z. M. Gibbs, Y. Tang, H. Wang and G. J. Snyder, *APL materials* **3** (4), 041506 (2015).

37. F. C. Correia, J. M. Ribeiro, A. Ferreira, J. S. Reparaz, A. R. Goñi, T. Boll, A. Mendes and C. J. Tavares, *Vacuum* **207**, 111572 (2023).
38. Y. Zhao, B. Chen, A. Miner and S. Priya, *RSC Advances* **4** (35), 18370-18377 (2014).
39. R. V. R. Virtudazo, B. Srinivasan, Q. Guo, R. Wu, T. Takei, Y. Shimasaki, H. Wada, K. Kuroda, S. Bernik and T. Mori, *Inorganic Chemistry Frontiers* **7** (21), 4118-4132 (2020).
40. Y. Wang and J. Zhao, *Journal of Nuclear Materials* **529**, 151931 (2020).

Chapter 6

Thermoelectric features of Al-Cu dual doped ZnO

This chapter briefly outlines the effect of aluminium and copper dual doping in the ZnO structure to improve the thermoelectric performance of ZnO. Energy filtering effect and increased lattice distortions lead to large enhancement in the thermopower and very low thermal conductivity in the Al- Cu dual doped ZnO.

6.1 Introduction

Thermoelectric materials gained immense attention because of their ability to scavenge waste heat from various sources and harvest electrical energy. Many theoretical and experimental investigations are ongoing to understand the mechanisms to improve thermoelectric conversion efficiency. Most attempts to increase the effectiveness of thermoelectric materials focus on two aspects - reducing the lattice part of thermal conductivity and increasing the power factor of the materials. Materials with enhanced electrical transport and minimum thermal conduction are advantageous for thermoelectric conversion applications.

Donor impurities have the potential to be employed to increase carriers, and it has been demonstrated that the addition of trivalent impurities like Al, In, and Ga optimises the electrical transport mechanisms in ZnO¹⁻⁴. The most effective approach for modifying the thermoelectric performance of ZnO is doping with elements that have oxidation states greater than +2. Some of the dopants that are frequently incorporated with ZnO are Al, In, Ni, Fe, etc. Aluminium is one of these dopants and is often employed as both a single dopant and a codopant in ZnO. Al doping in the Zn sites of the ZnO structure will contribute more free electrons in the conduction band and lower the electrical resistivity⁵. The thermoelectric characteristics could be substantially improved than pure ZnO by co-doping aluminium with transition metals like Ni, Sm, Mn, and Fe⁶⁻⁸. K.V. Zakharchuk et al. reported that the thermoelectric performance of Al and Zr codoped ZnO is higher than that of Al single-doped ZnO^{9, 10}. Al and B co-doped ZnO samples have the highest power factor, $6.33 \times 10^{-4} \text{ Wm}^{-1} \text{ K}^{-2}$ and ZnO materials with In and Ga co-doping exhibit a power factor enhancement of 112.8%¹¹.

This chapter describes the synthesis of Al and Cu dual doped ZnO microcrystals and the investigation of the improvement in the thermoelectric efficiency. Several investigations are showing the improvement in thermoelectric properties of aluminium and copper singly doped ZnO¹²⁻¹⁵. Since the ionic radii of Al and Cu are lower than that of Zn ($\text{Zn}^{2+} = 0.74 \text{ \AA}$, $\text{Cu}^{2+} = 0.73 \text{ \AA}$, $\text{Al}^{3+} = 0.54 \text{ \AA}$), doping of these

two ions will not change the ZnO structure and they will induce free charge carriers in the conduction band.

6.2 Experimental method

Al and Cu doped ZnO materials $Zn_{(1-(x-y))} Al_x Cu_y O$ ($x=0.01, 0.02$ $y=0.01, 0.03$) were prepared through solid state reaction method. 99.99% pure powders of Al_2O_3 , CuO, and ZnO were weighed and these powder mixtures were ground for 1 hour. The fine powders then calcinated at $450^\circ C$ and again ground for 1 hour. The calcinated powders were densified using a pelletizer and made into pellets. These pellets were kept for sintering in a high temperature furnace at $1300^\circ C$ for 4 hours and then allowed to cool. The prepared materials are named A1C1 ($Zn_{0.98} Al_{0.01} Cu_{0.01} O$), A2C1 ($Zn_{0.97} Al_{0.02} Cu_{0.01} O$), and A1C3 ($Zn_{0.96} Al_{0.01} Cu_{0.03} O$). The sintered pellets were used in powder and pellet form for various characterisation studies.

6.3 Results and discussions

6.3.1 X-ray diffraction analysis

The PXRD patterns of the prepared materials were recorded between the Bragg angle of 20° to 80° , which are shown in Fig 6.1. All the diffraction peaks observed in the XRD pattern are consistent with the hexagonal wurtzite structure of ZnO confirming the inclusion of the dopants into the ZnO structure. Copper and aluminium impurity peaks were not evident in the XRD profile and the characteristic peaks were matching with the ICSD card No: 165014 indicating the formation of ZnO phases with the P63mc space group. The peak intensity varied with dopant concentration and the material A2C1 had the lowest intensity as a result of enhanced lattice deformation caused by the inclusion of significant amounts of Al and Cu in the ZnO lattice. The shift observed in the characteristic peak (101), as depicted in Fig 6.2. substantiates the addition of Al, and Cu ions in the ZnO lattice. Differences in ionic radii between the host and dopant ions create large lattice distortions in the host material that leads to microstrain in the lattice.

Table 6.1 lists the variations in crystallite size and microstrain determined by the Williamson-Hall plot. All the doped samples possessed smaller crystallite sizes than pure ZnO which is ascribed to the decreased rate of crystal growth with an increase in the concentration of dopants¹⁶. Among the doped samples, A1C3 has a high crystallite size due to the maximum incorporation of dopants, which may segregate the dopant ions at the grain boundaries¹⁷, giving rise to the initiation of secondary growth formation. Negative strain indicates the lattice contraction which shortens the bond lengths in the crystal structure and it is identified as the higher angle peak shift in the XRD pattern. Lattice expansion is confirmed by the positive strain and lower angle peak shift observed in the XRD pattern⁶.

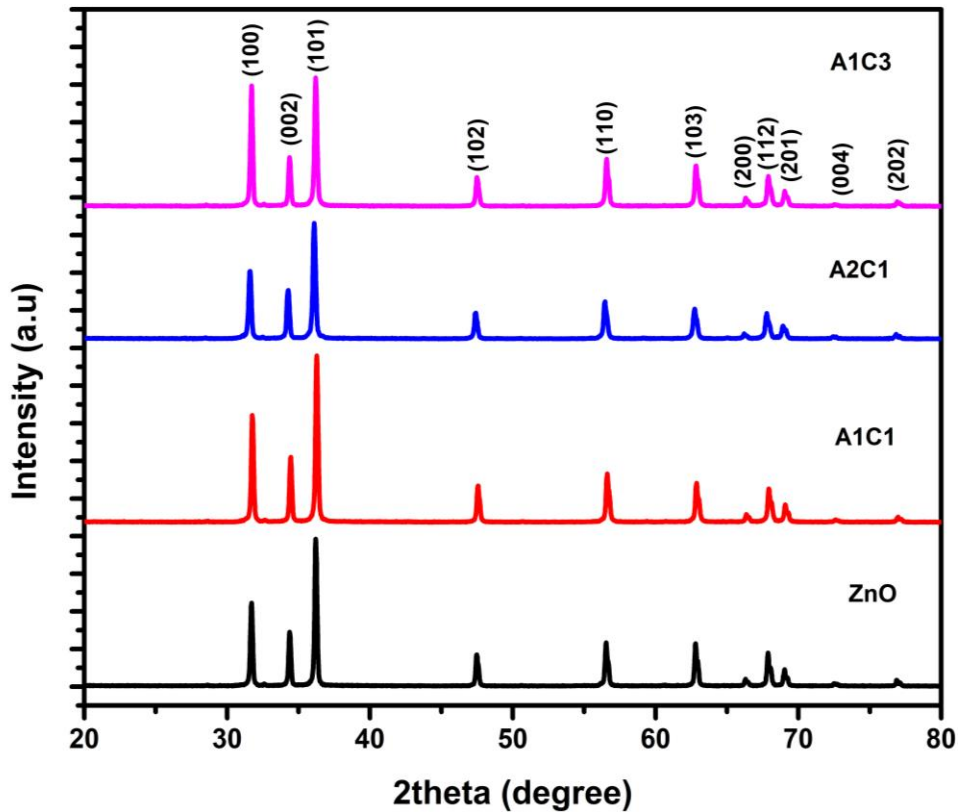
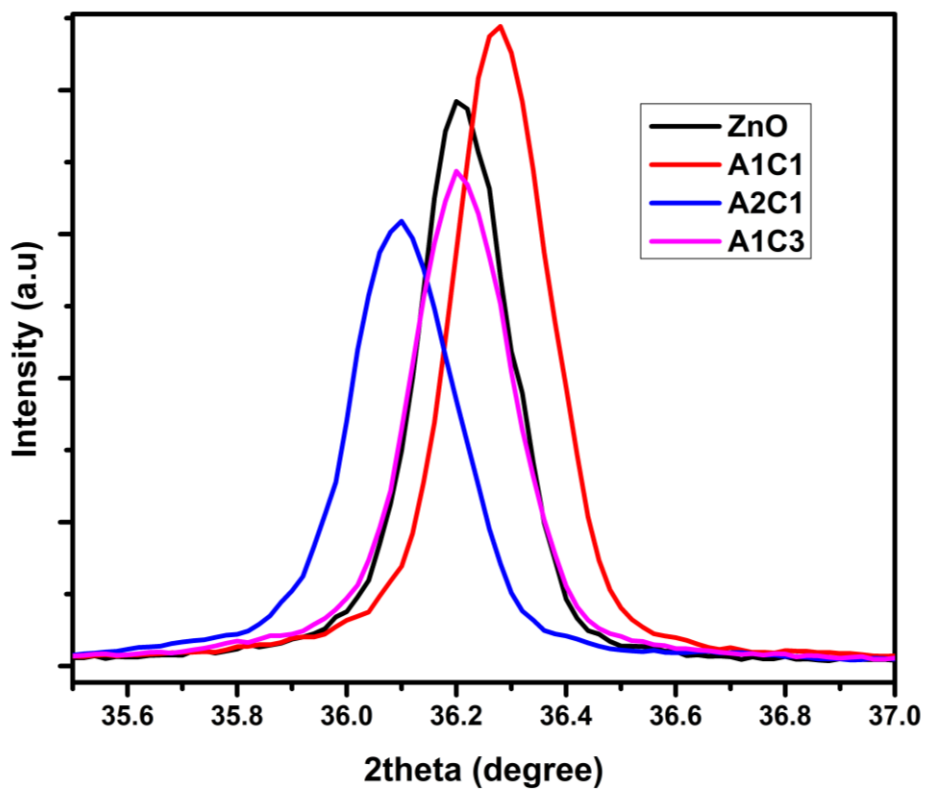


Fig. 6.1 XRD pattern of undoped and doped materials

Table 6.1 Crystallite size and induced microstrain

Sample	Crystallite size (nm)	Strain ϵ (10^{-4})
ZnO	59.25 ± 0.0004	-0.2540
A1C1	57.77 ± 0.0001	1.0927
A2C1	46.68 ± 0.0003	-0.1059
A1C3	49.87 ± 0.0003	0.1042

**Fig 6.2** XRD peak shift of (101) plane

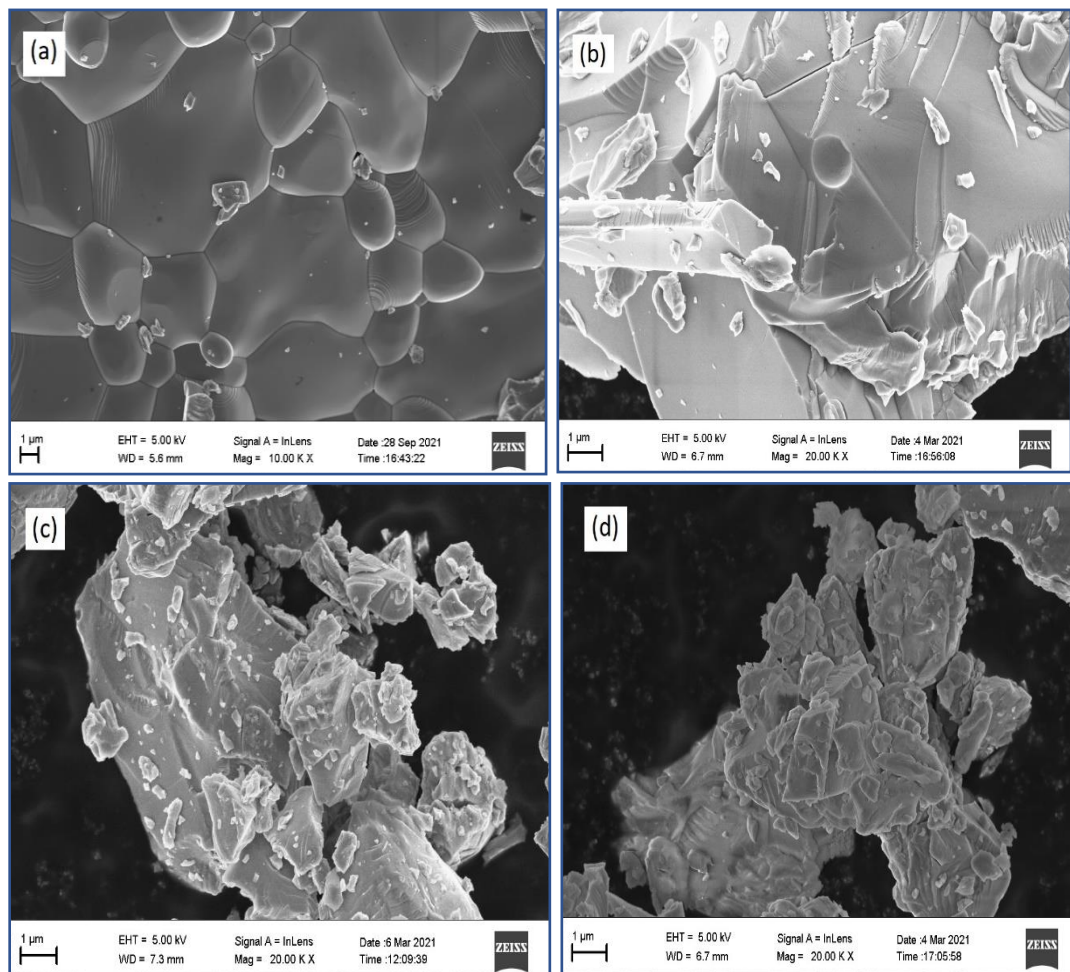


Fig 6.3 FESEM images of (a) ZnO (b) Al1C1 (c) Al2C1 (d) Al1C3

6.3.2 FESEM and EDAX analysis

Morphological identification of the materials was done with FESEM analysis and images of the synthesized materials are shown in Fig 6.3, showing significant variations from the undoped ZnO structure. The initiation of layered structure formation is observed in the samples with more doping concentration and as the copper content is increased, it is found that the surface become more layered as compared to the host morphology. Only the signals of Zn, Al, Cu and O are observed in the EDAX spectrum of the samples as presented in Fig 6.4 and no signals corresponding to impurity phases are obtained in the spectrum.

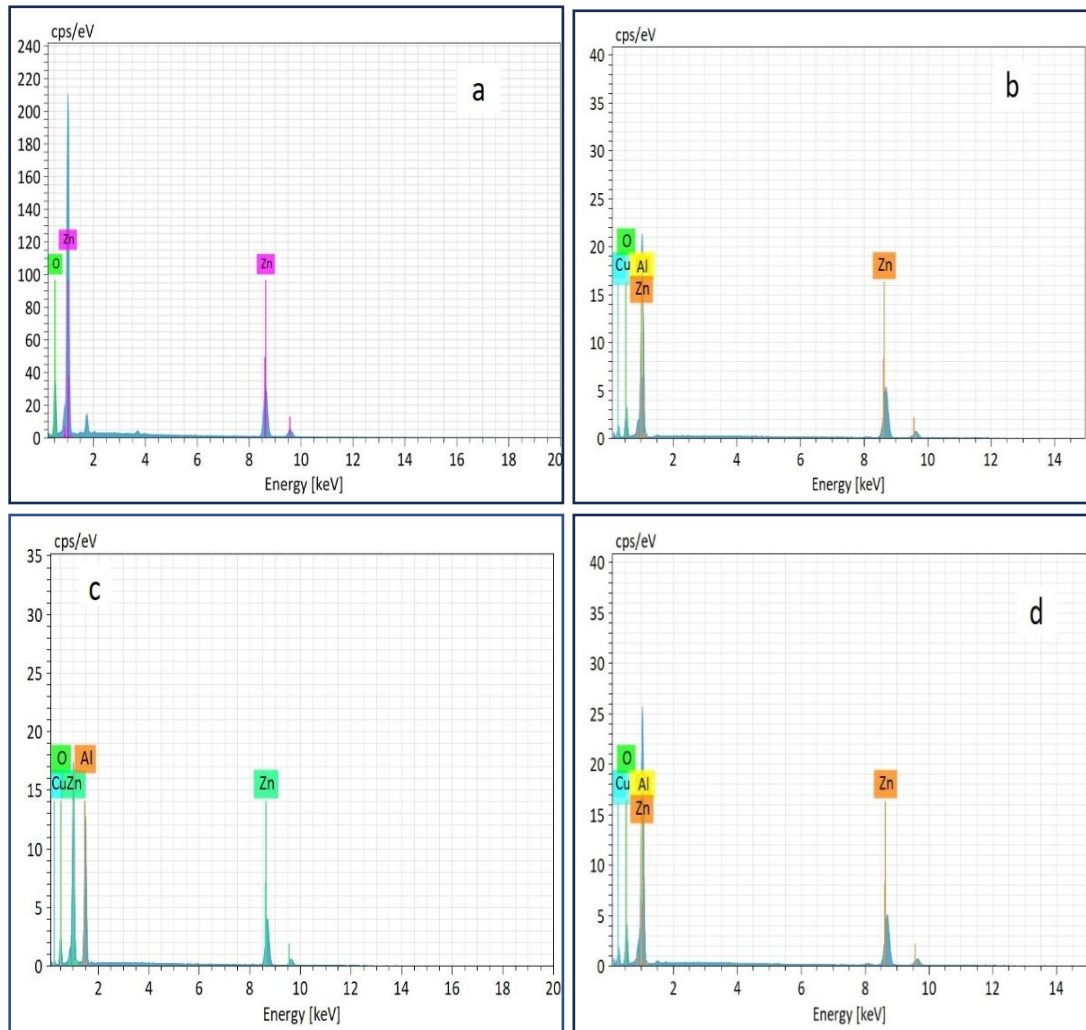


Fig 6.4 EDAX spectrum of materials (a) ZnO (b) A1C1 (c) A2C1 (d) A1C3

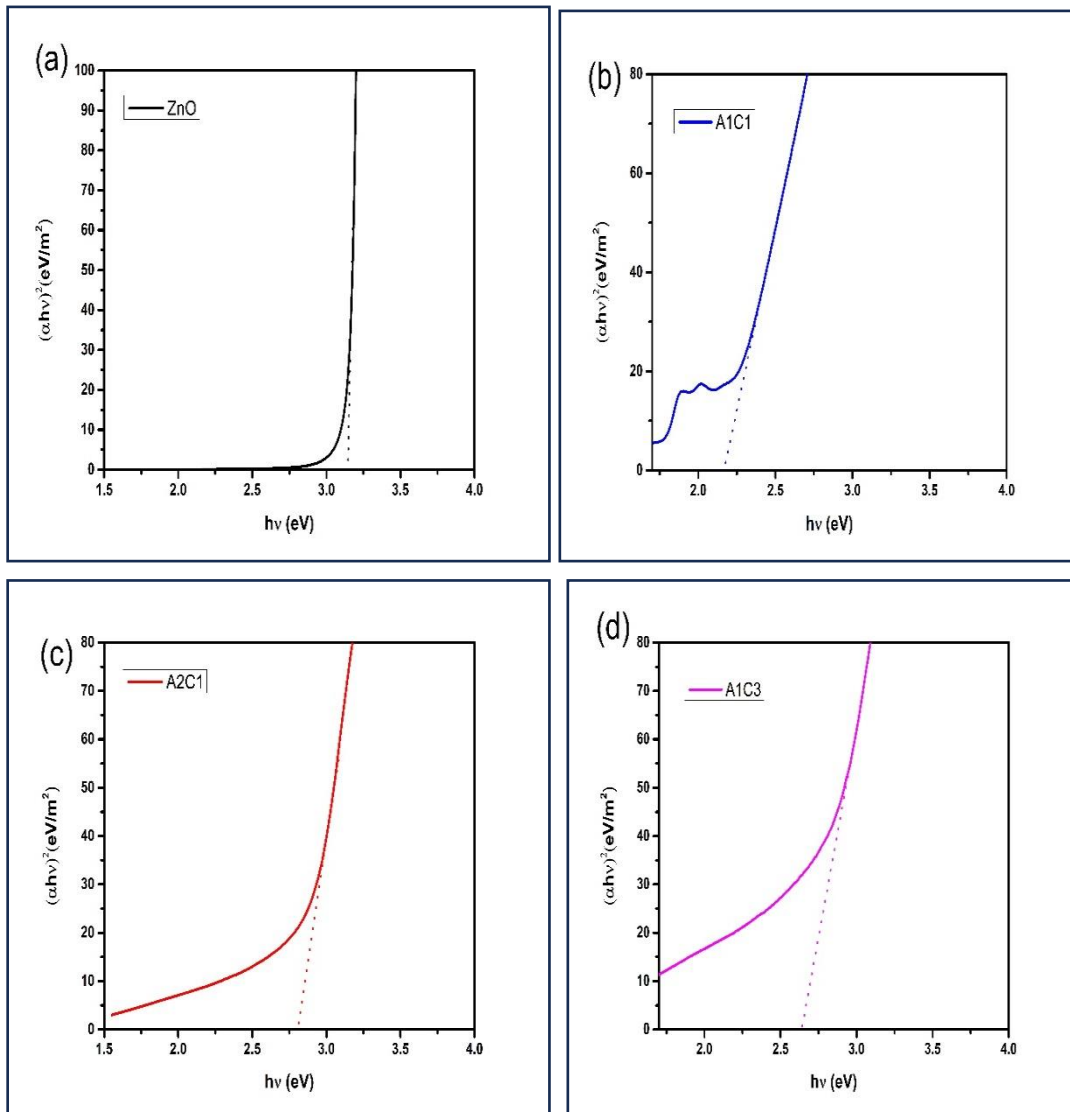


Fig 6.5 Band gap energy of (a) ZnO (b) A1C1 (c) A2C1 (d) A1C3

6.3.3 UV-Vis spectroscopic analysis

UV-Vis spectroscopic analysis enables the optical property studies of the materials. The optical band gap energies of the Al-Cu dual doped ZnO were determined from Tauc's plot plotted using Tauc's relation described in the previous chapters. The optical properties of ZnO are enhanced when doping with transition metals. The addition of impurities shifted the absorption edge to the lower energy region. As a result, the optical band gap energies of all the doped specimens are found to be decreased as presented in Fig 6.5. A2C1 and A1C3 show increased band gap energy

than A1C1 but less than that of ZnO. It is observed that Al addition causes a small increase in optical band cap energy as compared to the material doped with higher copper content. Laya et.al. reported the same result for Cu and Al singly and co-doped ZnO¹⁸. Mir Waghas et al observed that the decrease in optical band gap energy in Al and Cu singly doped ZnO is due to the increment in free carrier concentrations that occurred upon doping¹⁹. The band gap energy decreases due to the shifting of the valance band maximum and conduction band minimum and the downward shift of the conduction band is the main reason for band gap reduction in doped materials²⁰. The increase in carrier concentration and the increased defects created in the lattice lead to band gap reduction.

6.3.4 Thermoelectric property studies

6.3.4.1 Electrical conductivity

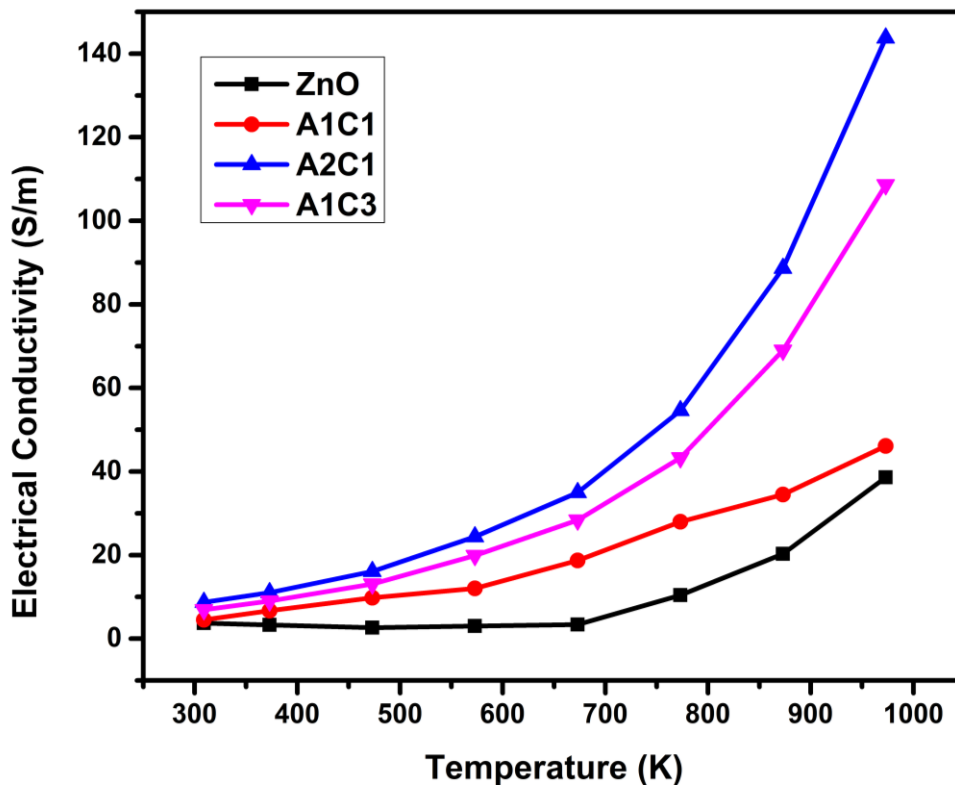


Fig 6.6 Temperature dependent electrical conductivity of the materials

The electrical conductivity of the pristine and Al-Cu dual doped ZnO is shown in Fig 6.6. The electrical conductivity increases with an increase in temperature, indicating the characteristics of semiconductors. The electrical conductivity of all the doped materials is higher than the pure ZnO. This increase is mainly attributed to the increase in charge carrier concentration on doping with donor cations like aluminium and copper. Al³⁺ is a trivalent cation which contributes electrons to the ZnO structure. The increase in carrier concentration is ascribed to the oxygen vacancies formed during high temperature sintering which can act as donors and generate additional electrons. The carrier concentrations of ZnO, A1C1, A2C1 and A1C3 materials estimated from the Hall measurement analysis are $6.20 \times 10^{19} \text{ m}^{-3}$, $1.91 \times 10^{20} \text{ m}^{-3}$, $4.94 \times 10^{20} \text{ m}^{-3}$ and $3.24 \times 10^{20} \text{ m}^{-3}$ respectively. The sample A2C1 possesses high electrical conductivity, more than four times increment in magnitude than the pristine ZnO. The low electrical conductivity of all the doped samples in the low temperature region is attributed to the recapturing of free electrons by the donor atoms. The defect formed in the lattice contributes to the electrical conductivity of the samples. The point defect concentration increases with an increase in temperature according to the relation,

$$c = N_{\text{sites}} \exp\left(-\frac{E^f}{k_B T}\right) \quad (6.1)$$

Where c is the point defect concentration, N_{sites} is the number of sites available for defect formation, E^f is the defect formation energy, k_B is the Boltzmann constant and T is the temperature. As the temperature increases, the concentration of oxygen vacancies increases and contributes to electrical conductivity²¹.

6.3.4.2 Seebeck coefficient

All the Al-Cu dual doped samples exhibit a large Seebeck coefficient than the pure ZnO as presented in Fig 6.7. The sign of the Seebeck coefficient is negative, denoting that both the host and doped materials have n-type conductivity. The samples A1C1 and A2C1 possess large Seebeck coefficients in the low temperatures up to 673 K and as the temperature increases, their value will gradually decrease.

But the Seebeck coefficient of A1C3 is lower than the pristine ZnO in the low temperature region and reaches a maximum value at 673 K and then decreases.

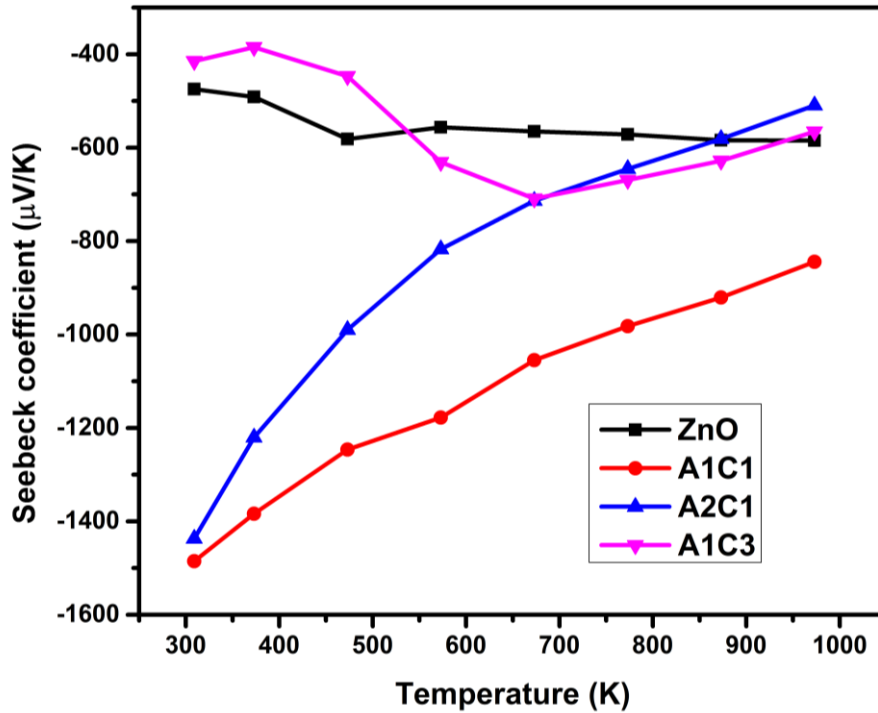


Fig 6.7 Temperature dependent Seebeck coefficient of the materials

The Mott's relation, which shows that the Seebeck coefficient and charge carrier density are inversely linked, can be used to determine the Seebeck coefficient of semiconducting materials. As a result, it is anticipated that Al, Cu dual doped material will have a low Seebeck coefficient as doping imparts additional carriers to the lattice structure. But Al, Cu dual doping leads to the enhancement of both electrical conductivity and Seebeck coefficient due to the energy filtering effect occurring in the lattice. Charge carriers with kinetic energies lower than chemical potential will contribute negatively to the overall Seebeck coefficient and if low-energy carriers can be effectively scattered by imposed potential barriers, an improvement in the overall Seebeck coefficient can be anticipated. However, as the temperature increases, the charge carriers acquire significantly higher kinetic energies, but the potential barrier remains constant at the same height, so the enhancement will become diminished²². The bipolar conduction mechanism that takes place at high temperatures will also decrease the Seebeck coefficient²³.

Since the dual doped materials exhibit a large Seebeck coefficient than the pristine sample, the density of state (DOS) effective mass calculation was conducted with the equation proposed by K.H.Lee et al ²⁴,

$$\log_{10} \left(\frac{m_d^*}{300} T \right) = \frac{2}{3} \log_{10}(n) - \frac{2}{3} [20.3 - (0.00508 \times |S|) + (1.58 \times 0.967^{|S|})] \quad (6.2)$$

The DOS effective mass estimated from the Seebeck coefficient (S) and carrier density (n) is presented in Table 6.2. The inclusion of dopants modified the electronic band structure of the parent lattice and creates more DOS and hence increase the DOS effective mass (m_d^*). The effective mass increases in samples with high doping concentration and the large increase in the Seebeck coefficient is attributed to the increase in density of state effective mass. The Fermi level shift from the conduction band edge ($E_c - E_f$) estimated from the Fritsche model which is explained in detail in the Chapter 5 is given in Table 6.2. The shift $E_c - E_f$ indicates that the Fermi level of the materials with negative Fermi level shift moves to the conduction band edge and that materials are degenerate. Sample A1C3 with increased Cu dopant has a low Fermi level shift and the sample A2C1 has the highest Fermi level shift among the doped samples.

Table 6.2 Fermi level shift and DOS effective mass of the samples

Sample	$E_c - E_f$ (eV)	DOS Effective mass (m_d^*) (m_e)
ZnO	-0.0531 ± 0.002	0.24
A1C1	-0.2837 ± 0.022	10.96
A2C1	-0.4169 ± 0.005	20.68
A1C3	-0.1282 ± 0.003	15.61

Due to the fluctuating potential in the ZnO crystal structure induced by the different electronegativities of Zn (1.65), Cu (1.9), and Al (1.61), there is a decrease in carrier

mobility, which increases the effective mass and the increase in effective mass increases the Seebeck coefficient of the prepared samples ²⁵.

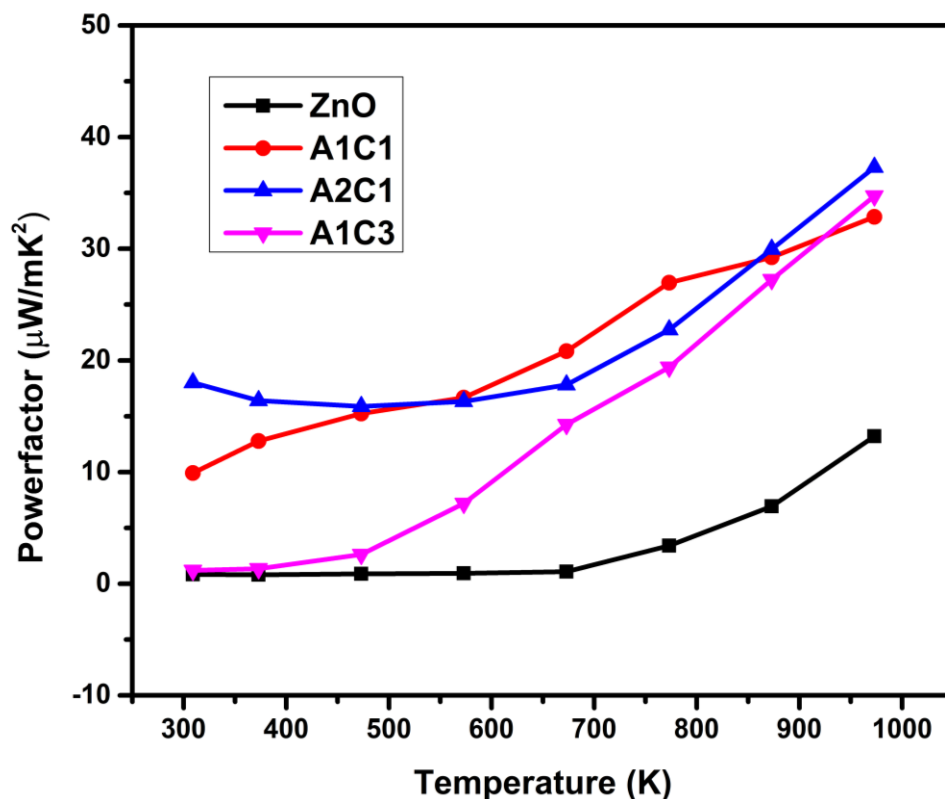


Fig 6.8 Temperature dependent power factor of the materials

6.3.4.3 Power factor

The increase in both electrical conductivity and Seebeck coefficient with temperature was greatly reflected in the power factor as shown in Fig 6.8. All doped materials have a higher power factor than that of the parent material. A greater increase in power factor is anticipated since all of the doped samples have a higher Seebeck coefficient and electrical conductivity than pure ZnO. However, the benefit of improved electrical conductivity cannot be justified when addressing the power factor because the Seebeck coefficient of all the materials decreases drastically at high temperatures. Among the synthesized materials, A2C1 has a large Seebeck coefficient and high electrical conductivity, therefore, it possesses a high power factor and can be used for thermoelectric power generation applications.

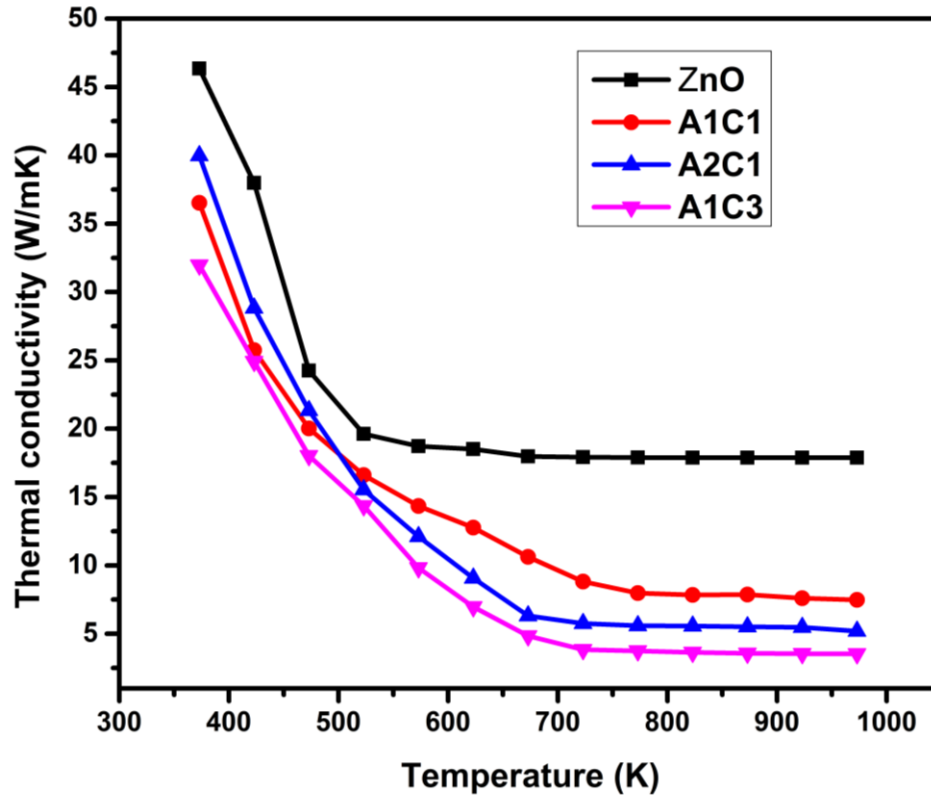


Fig 6.9 Temperature dependent thermal conductivity of the materials

6.3.4.4 Thermal conductivity

The thermal conductivity of metal oxides is very high as the atomic mass ratio (M/O) approaches unity. Simple lattice structures or smaller unit cells will also enhance thermal transport due to lattice vibrations or phonons. In semiconductors, the electronic contribution to the total thermal conductivity is very low and the major contribution, about 90% is from the phonons²⁶. It is confirmed by the thermal conductivities obtained for Al and Cu doped ZnO which are presented in Fig 6.9. The thermal conductivities of all the materials are very high and possess an exponential decay in the low temperature region where the phonon mean free path is very high. As the temperature increases, the thermal conductivity is independent of temperature. Due to an increase in the concentration of charge carriers, the electronic thermal conductivity may increase when the doping concentration is increased. The enhanced phonon scattering that occurs in the lattice structure, however, causes the lattice thermal conductivity to decrease. The impact of

electronic thermal conductivity on total thermal conductivity in ZnO is too small, and the lattice component contributes the majority of the overall thermal conductivity. Al and Cu doping significantly lower the lattice thermal conductivity, which scatters the low and high frequency phonons and lowers the thermal transport.

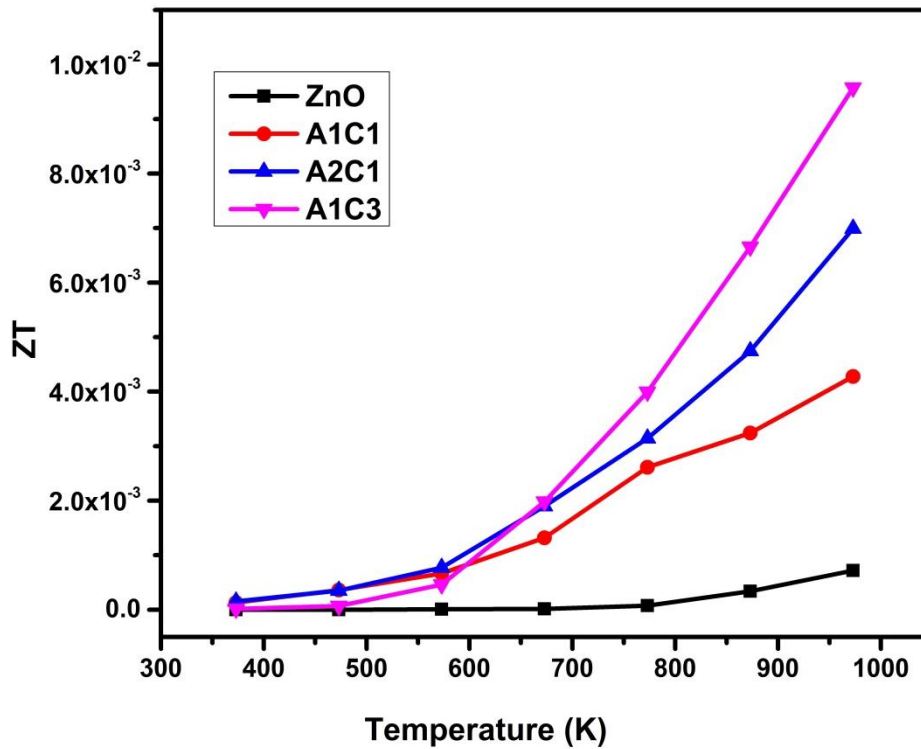


Fig 6.10 Temperature dependent figure of merit of the materials

6.3.4.5 Figure of merit

The figure of merit of the synthesized materials are shown in Fig 6.10. The cumulative effect of electronic and thermal transport occurred in the ZnO structure due to the addition of Al and Cu is reflected as the figure of merit in the dual doped materials. Since the electrical conductivity and Seebeck coefficient of all the doped materials increase concurrently with a decrease in thermal conductivity, the figure of merit of all the samples enhanced on doping. Among the samples, A1C3 shows a high figure of merit, because of its high power factor and low thermal conductivity.

6.4 Conclusion

To demonstrate the effect of Al, Cu doping in ZnO, solid state sintered materials with compositions $\text{Zn}_{(1-x-y)} \text{Al}_x \text{Cu}_y\text{O}$ ($x=0.01, 0.02$ $y= 0.01, 0.03$) were prepared. The structure of the prepared materials resembles the hexagonal wurtzite structure as that of the parent lattice and no secondary phase growth is detected from the structural and morphological analysis. Crystallite size and strain variations substantiate the inclusion of dopants and the presence of defects in the ZnO lattice. Variation of surface morphology with varying concentrations of dopants is identified from the FESEM and EDAX analysis, confirming the presence of the dopants in the host structure. The optical band gap energy of the dual doped materials decreased as a result of the increased defects and carrier enhancement. Al-Cu dual doping improves the electrical characteristics of the doped materials which causes an increment in electrical conductivity. Due to the impact of energy filtering, the doped materials exhibited large Seebeck coefficients. The combined effect of enhanced electrical conductivity and Seebeck coefficient were illustrated as the improved power factor in the doped materials. The defect concentration in the host structure increased on doping which resulted in the substantial reduction of thermal conductivity. The improvement in the Seebeck coefficient and electrical conductivity accompanied by a large reduction in thermal conductivity led to an enhancement in the thermoelectric efficiency of ZnO at 973 K.

References

1. L. Zhang, T. Tosho, N. Okinaka and T. Akiyama, *Materials transactions* **49** (12), 2868-2874 (2008).
2. P. Jood, R. J. Mehta, Y. Zhang, T. Borca-Tasciuc, S. X. Dou, D. J. Singh and G. Ramanath, *Rsc Advances* **4** (13), 6363-6368 (2014).
3. P. Jood, R. J. Mehta, Y. Zhang, G. Peleckis, X. Wang, R. W. Siegel, T. Borca-Tasciuc, S. X. Dou and G. Ramanath, *Nano letters* **11** (10), 4337-4342 (2011).
4. X. Wang, X. Huang, Z. M. Wong, A. Suwardi, Y. Zheng, F. Wei, S. Wang, T. L. Tan, G. Wu and Q. Zhu, *ACS Applied Nano Materials* **5** (6), 8631-8639 (2022).
5. H. Varudkar, G. Umadevi, P. Nagaraju, J. Dargad and V. Mote, *Journal of Materials Science: Materials in Electronics* **31** (15), 12579-12585 (2020).
6. J. Hoemke, A. U. Khan, H. Yoshida, T. Mori, E. Tochigi, N. Shibata, Y. Ikuhara and Y. Sakka, *Journal of the Ceramic Society of Japan* **124** (5), 515-522 (2016).
7. H. Yamaguchi, Y. Chonan, M. Oda, T. Komiyama, T. Aoyama and S. Sugiyama, *Journal of electronic materials* **40**, 723-727 (2011).
8. D.-B. Zhang, B.-P. Zhang, D.-S. Ye, Y.-C. Liu and S. Li, *Journal of Alloys and Compounds* **656**, 784-792 (2016).
9. K. V. Zakharchuk, D. M. Tobaldi, X. Xiao, W. Xie, S. M. Mikhalev, J. F. Martins, J. R. Frade, A. Weidenkaff and A. V. Kovalevsky, *Journal of the European Ceramic Society* **39** (4), 1222-1229 (2019).
10. K. V. Zakharchuk, M. Widenmeyer, D. O. Alikin, W. Xie, S. Populoh, S. M. Mikhalev, A. Tselev, J. R. Frade, A. Weidenkaff and A. V. Kovalevsky, *Journal of Materials Chemistry A* **6** (27), 13386-13396 (2018).
11. M. Ullah, S. Ullah, A. Manan, F. Khan, F. Zeb, I. Mehmood, M. U. Rehman and M. Amami, *Applied Physics A* **128** (2), 1-7 (2022).
12. N. Ma, J.-F. Li, B. Zhang, Y. Lin, L. Ren and G. Chen, *Journal of Physics and Chemistry of Solids* **71** (9), 1344-1349 (2010).
13. K. Cai, E. Müller, C. Drašar and A. Mrotzek, *Materials Science and Engineering: B* **104** (1-2), 45-48 (2003).
14. X. Qu, W. Wang, S. Lv and D. Jia, *Solid State Communications* **151** (4), 332-336 (2011).
15. D. V. Vu, D. H. Le, T. T. Nguyen, T. Van Duong, Q. D. Ngo and T. Q. Trinh, *Journal of Materials Science: Materials in Electronics* **30**, 6544-6551 (2019).
16. P. N. Mishra, P. K. Mishra and D. Pathak, *Chemistry* **4** (4), 1136-1146 (2022).
17. U. Rehman, J. Jacob, A. Mahmood, K. Mahmood, A. Ali, A. Ashfaq, M. Basit, N. Amin, S. Ikram and S. Hussain, *Journal of Alloys and Compounds* **843**, 156081 (2020).

18. L. Dejam, S. Kulesza, J. Sabbaghzadeh, A. Ghaderi, S. Solaymani, Ş. Tãlu, M. Bramowicz, M. Amouamouha and A. hossein Sari, *Results in Physics* **44**, 106209 (2023).
19. M. W. Alam, M. Z. Ansari, M. Aamir, M. Waheed-Ur-Rehman, N. Parveen and S. A. Ansari, *Crystals* **12** (2), 128 (2022).
20. N. Kamarulzaman, M. F. Kasim and R. Rusdi, *Nanoscale research letters* **10**, 1-12 (2015).
21. A. Janotti and C. G. Van de Walle, *Physical Review B* **76** (16), 165202 (2007).
22. J. Zhang, D. Wu, D. He, D. Feng, M. Yin, X. Qin and J. He, *Advanced Materials* **29** (39), 1703148 (2017).
23. P. Shyni and P. Pradyumnan, *RSC Advances* **11** (8), 4539-4546 (2021).
24. K. H. Lee, S. i. Kim, J. C. Lim, J. Y. Cho, H. Yang and H. S. Kim, *Advanced Functional Materials* **32** (33), 2203852 (2022).
25. N. H. Tran Nguyen, T. H. Nguyen, Y.-r. Liu, M. Aminzare, A. T. T. Pham, S. Cho, D. P. Wong, K.-H. Chen, T. Seetawan and N. K. Pham, *ACS applied materials & Interfaces* **8** (49), 33916-33923 (2016).
26. T. Tsubota, M. Ohtaki, K. Eguchi and H. Arai, *Journal of Materials Chemistry* **7** (1), 85-90 (1997).

Chapter 7

General Conclusions

This chapter summarises the research work discussed in the thesis and the conclusion of the findings of the research.

7.1 Introduction

Thermoelectricity is one of the simplest energy conversion technologies applicable to heat-to-electricity transformation. Thermoelectrics are capable of power generation and active spot-size heat management. As heat is ubiquitous, thermoelectricity has secured a position as one of the solutions to global energy needs and environmental crisis. By analyzing the history and progress of thermoelectrics, this technology was rejuvenated through different new potential paradigm mechanisms such as size effect, defect engineering, scattering mechanisms, etc. All these mechanisms attempt to decouple the contradiction existing between the electrical and thermal transport properties in achieving the highest figure of merit. If the current trends in thermoelectric research will sustain, this technology will be the most prominent renewable energy source in the future.

7.2 Summary of the research work

Electricity is considered the fuel of the modern world and can be generated from various sources such as nuclear energy, hydropower, solar energy, etc. But thermoelectricity or electricity from waste heat serves as a renewable energy source and the best means to minimize the global atmospheric temperature and carbon footprints to a great extent.

This thesis is focused on the effect of dual doping on the enhancement of thermoelectric properties of ZnO. To date, there are so many thermoelectric materials with high thermoelectric efficiency. But most of the materials have low temperature applications and many of them are toxic. The search for an eco-friendly thermoelectric material that can be used at elevated temperatures led the scientific community into the fields including oxide materials. Several investigators studied the thermoelectric properties of many oxides such as SnO₂, SrTiO₃, ZnO, CuO, etc. The research on oxides reveals that the metal oxide ZnO is an eco-friendly, highly efficient thermoelectric material that can withstand high temperatures and possesses high chemical stability. The doping method is adopted to enhance the thermoelectric properties of ZnO, as it will enhance the electrical transport properties and inhibit the thermal conduction in ZnO material. Multiple doping is more effective in many

ways than single doping, therefore, dual doping of ions into the host lattice was done to investigate the enhancement of thermoelectric properties of ZnO. The solid-state reaction method was used to synthesize the dual doped ZnO materials, as it is one of the most appropriate methods to synthesize polycrystalline materials with reduced size. Transition metal ions, trivalent ions, and rare earth ions were chosen to tune the thermoelectric properties of ZnO, and four different combinations of these ions (Ni-In, Ni-Pr, Ni-Cu, and Al-Cu) were chosen for the preparation of dual ion doped ZnO. The thermoelectric characteristics of all the dual-doped ZnO systems have improved and proven to be promising candidates for thermoelectric applications. The findings on the effect of dual doping on the physical and thermoelectric characteristics of ZnO are summarised below.

7.2.1 Ni and In dual doped ZnO

Nickel is a frequently employed dopant in ZnO because it increases both the electrical conductivity and the Seebeck coefficient while lowering the thermal conductivity, thereby improving thermoelectric efficiency. The trivalent ion In doping induces more carriers and enhances the power factor by suppressing the electrical resistivity of ZnO. Dual substitution of Ni and ion of large size than ZnO created defects in the host structure and hence minimizes the thermal transport. Therefore, dual doping of Ni and In will lead to a large enhancement in the thermoelectric properties of ZnO.

Solid state sintered Ni and In dual doped ceramics were synthesized with the compositions Ni=0.01, In=0.0025, 0.005, 0.01, 0.02, 0.03. Structural, morphological, optical, and thermoelectric characterizations were done with the sintered materials. The conclusion of the findings is given below,

- The Ni and In dual doped materials resemble the hexagonal wurtzite structure as that of the host material, and the variation of crystallite size and strain indicates the inclusion of the cations into the ZnO lattice.

- The suppression of grain growth and reduction in porosity is observed in the FESEM analysis which will be advantageous to reduce the thermal conductivity.
- Red shift in the absorption edge was observed and the optical band gap energy was reduced from 3.1 eV to 2.2 eV due to the presence of defects and increased strain formed upon doping.
- The electrical conductivity of the dual doped sample was enhanced due to the increment in charge carrier density that occurred upon Ni²⁺ and In³⁺ dual doping in the ZnO lattice. Among the doped samples, N₁I₁ has high electrical conductivity of 50600 S/m.
- All the doped samples have low Seebeck coefficient than the pure ZnO since the dual doped materials have high carrier density.
- Improved electrical transport properties of the doped samples led to a power factor of 1427 $\mu\text{W}/\text{mK}^2$ in the N₁I₁ sample.
- Nickel and indium dual doped ZnO materials are good candidates for the thermoelectric application since it possesses reduced thermal conductivity than the host ZnO with an enhanced figure of merit of 0.11.

Among all dual doped ZnO materials, the N₁I₁ sample possesses the high thermoelectric figure of merit at 973 K. Therefore, these materials are suitable for high temperature thermoelectric applications.

7.2.2 Ni and Pr dual doped ZnO

As mentioned in the previous chapters, ions with larger ionic radii will create more lattice defects leading to a reduction in the thermal conductivity of ZnO. Lanthanides had a significant impact on modulating the thermoelectric characteristics of a material. Lanthanide substitution modifies the band structure and hence the density of the state of the parent lattice. As they have larger ionic radii, they will induce more lattice imperfections and strengthen the phonon scattering mechanism. As a dopant, Ni imparts more carriers into the host structure and

increases the electronic transport properties of the host matrix. Therefore, dual doping of nickel with praseodymium will enhance the electrical transport properties and inhibit the thermal transport properties of ZnO. The samples with compositions Ni=0.01, Pr=0.003, 0.005, 0.007 were prepared and the results of various characterization studies are summarised as,

- Structural studies and the optical band gap reduction confirmed the inclusion of the dopants into the host lattice.
- Dual doping of nickel and praseodymium increases the carrier density, which causes enhancement in the electrical conductivity of the doped materials.
- Due to the energy filtering effect, simultaneous increments in electrical conductivity and the Seebeck coefficient were observed, which resulted in an enhanced power factor in doped materials.
- The thermal conductivity of the dual doped materials was drastically reduced from 17.8 W/mK to 3.7 W/mK due to the increased lattice distortions created in ZnO on doping heavier praseodymium ions along with nickel.
- Enhancement of power factor with a significant thermal conductivity reduction led to triple enhancement in the thermoelectric figure of merit of doped ZnO.

Despite its low electrical characteristics, the sample doped with the maximum Pr³⁺ concentration (N₁P_{0.7}) possesses a higher thermoelectric figure of merit at 973 K as its total thermal conductivity is highly reduced upon doping.

7.2.3 Ni and Cu dual doped ZnO

Several investigations report the effect of transition metal doping on the enhancement of thermoelectric properties of ZnO. Nickel and copper were well incorporated into the ZnO lattice and possess high solubility because of their similar valency and size. Nickel and copper singly doped ZnO materials enhance electrical conductivity/Seebeck coefficient. But nickel and copper dual doping shows

simultaneous increments in electrical conductivity and Seebeck coefficient. Therefore, these materials are suitable for thermoelectric applications. Samples with compositions Ni=0.01, 0.02, Cu=0.01, 0.02 were prepared through solid state reaction method, and the results of the various characterizations are,

- The structural and morphological analysis of the doped materials confirmed the hexagonal wurtzite structure of ZnO.
- The substitution of the dopants into the host matrix was established by the strain induced in the lattice and the variation of crystallite size
- The optical band gap energy shows a reduction from 3.1 eV to 2.15 eV with a redshift in the absorption edge.
- The electrical conductivity and Seebeck coefficient of ZnO increased upon doping. The most distinguished result of Ni-Cu dual doping is the enhancement of the Seebeck coefficient to $\sim 1318 \mu\text{V/K}$.
- The thermal conductivity of ZnO is considerably reduced to 8.36 W/mK as a result of the lattice distortion created due to the dual substitution of the dopants.
- The power factor enhancement and degradation of thermal conductivity give rise to a six-fold increase in the thermoelectric figure of merit of the material

The electrical characteristics of the host system were enhanced and the phonon conduction was greatly suppressed by the addition of Al and Cu into ZnO and the sample N1C2 with optimum copper concentration shows better thermoelectric performance because of its reduced thermal conductivity and highly improved power factor.

7.2.4 Al and Cu dual doped ZnO

Trivalent impurities such as Al will enhance the electrical conductivity of the parent lattice as it contributes more electrons to the host structure. Dual doping of Al with Cu will improve the electrical transport properties and create more lattice defects

which reduce the thermal conductivity of ZnO. So, dual doping of aluminium and copper is beneficial to increase the thermoelectric efficiency of ZnO. The main findings of Al and Cu dual doped samples (Al=0.01, 0.02, Cu=0.01, 0.03) are summarised as,

- The structural and morphological analysis confirmed the inclusion of Al³⁺ and Cu²⁺ ions in the ZnO lattice.
- The optical band gap energy strongly depends on the induced defects which is reduced to 2.17 eV
- Trivalent impurity addition together with copper caused an increment in carrier density and thereby enhanced the electrical conductivity
- A high Seebeck coefficient of -1485 $\mu\text{V/K}$ was obtained in the dual doped samples due to high effective mass and the carrier filtering effect that occurred in the host structure.
- The thermal conductivity of ZnO is decreased from 17.87 W/mK to 3.52 W/mK when doping with Al³⁺ and Cu²⁺ ions which causes large lattice distortions in the ZnO lattice.
- Enhancement in power factor and reduction in thermal conductivity significantly enhanced the thermoelectric figure of merit.

Among the doped samples, the sample with the maximum copper concentration (A1C3) exhibits high thermoelectric performance because of its very low thermal conductivity and significantly improved electrical transport properties.

A table comparison of the results obtained for materials with high efficiency among the four series of dual doped ZnO materials with pure ZnO is given in Table 7.1. The sample doped with Ni and In are the material with enhanced thermoelectric efficiency and is most suitable for thermoelectric as well as sensor applications.

Table 7.1 Comparison of TE properties of best performed dual doped material with ZnO

Sample	PF ($\mu\text{W}/\text{mK}^2$)	κ (W/mK)	ZT
ZnO	13.20	17.87	7.18×10^{-4}
N ₁ I ₁	1427	10.63	0.11
N ₁ P _{0.7}	16.8	3.7	3.93×10^{-3}
N1C2	28.91	9.61	4.29×10^{-3}
A1C3	34.73	3.52	9.58×10^{-3}

The results mentioned above are the main outcome of this research work which substantiates the effectiveness of dual doping in enhancing the thermoelectric properties of ZnO. The enhancement of electrical transport properties and hindering of thermal transport is observed in all the dual doped materials and hence the advancement in the thermoelectric efficiency of ZnO is achieved. All the synthesized dual doped ZnO systems possess better thermoelectric efficiency in the high temperature region. Therefore, these materials can be used to develop new high temperature thermoelectric conversion devices for power generation and sensor applications.

Chapter 8

Scope for future research

This chapter deals with the recommendations for future research required for the materials discussed in this thesis.

8.1 Introduction

Thermoelectric technology is now widely applied in many small- and large-scale systems such as in the aerospace sector and systems to operate human artificial internal organs. But the low efficiency and sustainability of current thermoelectric materials are the main obstacle to the wider application of this technology. To expand the application of thermoelectric technology into all areas of energy production, it is to be ensured that it is capable of competing on efficiency with the current prominent systems. Synergistic efforts may be paid to develop thermoelectric materials with high performance and that materials can effectively harvest electrical energy from waste heat. Hence thermoelectric devices play a major role in minimizing the global atmospheric temperature and ensuring zero carbon emissions.

8.2 Recommendations for future research

The expected outcome of the research is to synthesize doped oxide materials with enhanced thermoelectric properties and we have succeeded in achieving this objective by successfully synthesizing dual doped ZnO materials with improved thermoelectric conversion efficiency. Since the synthesized materials possess better thermoelectric properties, that materials can be found applications in thermoelectric power generation and sensors.

Thermoelectric materials are essential for the fabrication of thermoelectric devices such as power generators, refrigerators, and sensors. But in order to manufacture thermoelectric devices capable of power generation and refrigeration, it needs to be ensured that the materials have high thermoelectric efficiency. So based on our research on dual doped ZnO thermoelectric, the following recommendations can be done as an extension of the current research work.

1. In this work, the synthesized materials are n-type materials and if suitable p-type dual doped ZnO materials can be fabricated, thermoelectric module preparation can be possible for device manufacturing.

2. Low-dimensional systems show better thermoelectric properties than bulk materials. So, preparing nanostructured (nanocomposites) dual doped materials will enhance the electronic transport properties and reduce thermal conduction simultaneously.
3. Dual-doped thin films with well-defined thicknesses can be fabricated through methods such as doctor blade coating techniques, which are advantageous to enhance thermoelectric properties with very low thermal conductivity.
4. A low-temperature thermoelectric study can be carried out with these materials as the oxide ceramic materials will show excellent thermoelectric properties in the very low-temperature region.
5. Spin Seebeck analysis of the dual doped ZnO materials with nickel codopant can be done as Ni²⁺ ions are magnetic.
6. The theoretical studies of these research works can be carried out using advanced techniques such as DFT.
7. Besides oxides, many investigations substantiate the effect of dual doping on the enhancement of thermoelectric properties of various systems. So, our investigation can be extended to other systems such as ZnSe, ZnS, etc.
8. New material synthesis methods such as co-precipitation and hydrothermal methods can be adopted by which nanomaterials synthesis can be achieved that reduce the thermal conductivity and enhance the thermoelectric efficiency.